An electrophysiological assessment of the use of stem cells in neurological disease modelling and therapy

O.G. Steele

Master of Philosophy in Biosciences
Cardiff School of Biosciences

Supervisor(s): *Professor P.J. Kemp, Professor A.E. Rosser*
Word Count: *23,959 (Excluding figure legends & reference lists)*
Date of Submission:

Acknowledgements

I'd like to thank Dr David Millar for his help on the CDKL5 project and Dr Ana Garcia Aguirre and the rest of the BRG for their help on the Repair HD project. I'd also like to thank Dr. Christian Schnell and Dr Francesco Tamagnini for their electrophysiological expertise and ability to answer my endless questions. I would like to thank Dr. Jessica Griffiths for her relentless positivity, and all of Prof. Riccardi's lab members for their support also. Most importantly, enormous thanks goes to Prof. Paul Kemp for his unconditional support and guidance both professionally and personally. You're an inspiration and a role model, and the completion of this thesis and future work simply would not be possible without all that you have done for me.

Declaration

I, Oliver George Steele, hereby declare no conflict of interest and that all work conducted is a product of my own original work unless explicitly stated throughout. No work presented here is also being submitted for any other degree qualification. Work for the Huntington's Disease arm of the project was funded by the European consortium, Repair HD.

Date of Declaration: 25/01/2019

Signature: Steele

Abstract

Electrophysiology is the best discipline to functionally characterise neuronal behaviour, as such, electrophysiology plays a key role in neurological disease modelling and therapy. Totipotent stem cells have the limitless possibility to differentiate into any type of cell within the human body and therefore used frequently in disease modelling and therapy. This thesis aims to electrophysiologically assess the use of stem cells in disease modelling and therapy across two diseases; the infantile epilepsy disorder - cyclin dependant kinase like 5 (CDKL5) deficiency, and the fatal neurodegenerative condition - Huntington's Disease, respectively. This thesis shows that a patient induced pluripotent stem cell derived cortical neuronal model of CDKL5-deficiency recreates the epilepsy seen in patients, providing a valid disease model. Furthermore, these neurons can be cultured on a high-throughput multi-electrode array for the rapid testing of novel therapeutic compounds. In the disease therapy side of the project, stem cell grafts fail to functionally integrate synaptically into a rat model of Huntington's Disease (HD), however restore synaptic function in the lesioned striatum. These data suggest that the stem cell graft may provide therapeutic benefits, just not electrophysiologically. Taken together, these observations suggest that stem cells can reproduce the defining clincal charactersistics, epilepsy, lacking from other model systems in an infantile epilepsy model and induce acute therapeutic benefits in a rodent model of HD.

Word Count: 219 words

Table of Contents

List of Abbreviations

(In order of appearance)

Abbreviation	…	Term	Abbreviation	…	Term
hESC(s)	…	Human embryonic stem cell(s)	R	…	Gas constant
ICM	…	Inner cell mass	T	…	Absolute temperature
iPSC(s)	…	Induced pluripotent stem cell(s)	z	…	Valency of the ion
h-iPSC(s)	…	Human induced pluripotent stem cell(s)	F	…	Faraday Constant
MGE	…	Medial ganglionic eminence	ATP	…	Adenosine triphosphate
LGE	…	Lateral ganglionic eminence	P	…	Permeability
CGE	…	Caudal ganglionic eminence	GABA	…	Gamma-aminobutyric acid
WGE	…	Whole ganglionic eminence	v-SNARE(s)	…	Vesicle soluble N-ethylmaleimide-sensitive factor attachment protein receptor(s)
hWGE	…	Human whole ganglionic eminence	t-SNARE(s)	…	Target soluble N-ethylmaleimide-sensitive factor attachment protein receptor(s)
rWGE	…	Rat whole ganglionic eminence	AMPA(R)	…	α-amino-3-hydroxy-5-methyl-4-isoxazolepropionic acid receptor
HD	…	Huntingtons Disease	(f)EPSP	…	(Field) excitatory post synaptic potential
Q	…	Charge	MSN	…	Medium spiny neurons
C	…	Coulombs	NCC		Na+/Cl- cotransporter
I	…	Current	NKCC		Na+/K+/Cl- cotransporter
A	…	Amperes	KCC	…	K+/Cl+ cotransporter
V	…	Volts	NDCBE	…	Na+/HCO3-/Cl- exchanger
J	…	Joules	mRNA	…	Messenger ribonucleic acid
g	…	Conductance	(a)CSF	…	(Artificial) cerebrospinal fluid
E	…	Voltage difference	MEA	…	Multi-electrode array
Ω	…	Ohms	PDL	…	Poly-D-lysine

R	…	Resist	DIV	…	Days *in vitro*
c	…	Capacitance	NPC(s)	…	Neural progenitor cells
f	…	Farads	CDKL5	…	Cyclin dependant kinase like 5
Q	…	Charge	WT	…	Wild type
V_m	…	Membrane potential	BDNF	…	Brain derived neurotrophic factor
CNS	…	Central nervous system	PolyQ	…	Polyglutamine
Na	…	Sodium	KO	…	Knockout
K	…	Potassium	3-HK	…	3-hydroxykynurenine
Ca	…	Calcium	NMDA(R)	…	N-methyl-D-aspartate (receptor)
Cl	…	Chloride	18F-FDG	…	18F-fleurodeoxyglucose
E_{ion}	…	Equilibrium potential			

Chapter 1 - General Introduction

1.1 Stem Cells: Origins, applications and issues

1.1.1 Human embryonic stem cells (hESCs)

Stem cells have the unique ability to differentiate into the many other types of mature cells within the body, and can broadly be classified as either embryonic or adult. Embryonic stem cells are pluripotent, meaning that they can differentiate into cells derived from the three primary germ layers: endoderm; mesoderm, and; ectoderm. Adult stem cells tend to reside in the tissue with which they are associated, and are more restricted in their differentiation potential (Boyle, 2008). Following formation of a zygote, the next steps in embryogenesis are the merula, followed by the blastocyst. The blastocyst is composed of the external trophectoderm and inner cell mass (ICM). It is from this ICM that embryonic stem cells are taken. Originally isolated from the mouse embryonic ICM in 1981 (Evans and Kaufman, 1981), it wasn't until 1998 that the first hESC was generated (Thomson et al., 1998).

Within the hESC is a complex transcriptional regulatory circuit that impairs differentiation and maintains pluripotency; this regulatory pathway intimately involves *SOX2*, *OCT4* and *NANOG* (Boyer et al., 2005). These transcriptional regulators simultaneously inhibit transcription of certain genes such *NEUROG1*, essential for neurogenesis (Gao et al., 2009), and *HAND1*, essential for mesoderm development (Barnes et al., 2010 p.1), whilst promoting the expression of genes such as *MYST3*, *SET* and *SMARCAD1*; genes involved in histone acetylation, methylation and chromatin remodelling, respectively.

The milestone generation of hESCs in 1998 provided the first reliable source of stem cells for disease modelling and drug discovery and are still employed today (Marolt et al., 2012). The first successful use of hESCs for disease therapy was 14 years later when hESC-derived retinal pigment epithelium were transplanted into the eye of a patient with Sargardt's macular dystrophy (Schwartz et al., 2012). However, clinical use of hESCs remains limited, largely due to the fears surrounding hESC graft-derived tumour formation as a result of the fast proliferation and self-renewal properties of hESCs (Hentze et al., 2009). The other large practical concern surrounding the use of hESC derived grafts in disease therapy is associated with immune rejection and the need for patients to be on immune rejection therapy before, during and a long time after the surgery. Furthermore, the fact that hESCs are derived from human embryos is a source of huge ethical concern amongst certain sections of society.

1.1.2 Induced pluripotent stem cells (iPSCs).

A potential alternative to hESCs, potentially bypassing the ethical issues surrounding their human embryonic source, was presented by Takahashi *et al.,* with the advent of iPSCs. In 2006 Takahashi & Yamanaka first demonstrated the generation of embryonic-like features by reprogramming murine fibroblast cells using retroviral transfection of genes associated with pluripotency *OCT3/4*, *Sox2*, *Klf4* and *c-Myc* (Takahashi and Yamanaka, 2006). This revolutionary step was then refined to generate human iPSC (h-iPSC) from human fibroblasts (Takahashi et al., 2007).

The advent of h-iPSCs allowed the generation of patient- and disease-specific models on which to test novel therapeutics. Furthermore, the ability to generate h-iPSCs could, in principle, allow for patient-specific grafts, autografts, that might bypass the practical problems associated with immune rejection. However, there are still issues surrounding the use of h-iPSCs which may limit their clinical applications, including: i) iPSCs appear to have a more 'closed' chromatin structure compared to their hESC counterpart and questions remain about the ‘completeness’ of the reprogramming and whether any somatic memory persists, and; ii) induction of pluripotency as a result of transfection of proto-oncogenes (LING et al., 2012; Wuebben and Rizzino, 2017; Zhao et al., 2018),. may lead to teratoma formation in grafts.

1.1.3 Ganglionic eminence cells

During neurogenesis the ICM of the blastocyst forms two layers collectively termed the bilaminar embryonic disc. The external layer of this disc, the epiblast, gives rise to the three primary germ layers; the endoderm, mesoderm and ectoderm. It is the ectoderm that forms the neural plate and subsequently the neural tube between days 20 and 29 post fertilisation in humans. The anterior part of this neural tube then develops into the prosencephalon, giving rise to the telencephalon and diencephalon. The ventral telencephalon then matures into the medial, lateral and caudal ganglionic eminences (MGE, LGE and CGE) and the anterior entopeduncular area. The ganglionic eminence, a transitory brain structure, facilitates tangential cell migration, eventually forming the basal ganglia which are made up of the striatum and globus pallidus (Bear et al., 2001).

Harvesting of the MGE, LGE and CGE, collectively termed the whole ganglionic eminence (WGE) from medically terminated human foetal tissue generates human WGE (hWGE) cells. Rat WGE (rWGE) are neurons harvesting from the ganglionic eminence of foetal rat tissue in the same way. These embryonic cells are much further along their respective differentiation timelines and, as such, can only differentiate into a very limited subset of neurons making them neural progenitor cells, rather than stem cells. The use of human WGE (hWGE) is associated with very significant ethical concerns since the cells are harvested from relatively late gestation human foetuses (between 8 and 14 weeks post-conception). However, these cells are not as commonly associated with issues surrounding teratoma formation making them an attractive source of cells for cell replacement therapy.

1.1.4 Stem cell technology and neurological disease modelling and therapy

Stem cells have proven invaluable in modelling neurological diseases and have led to the discovery of key pathogenic processes and testing of novel therapeutics. Due to the difficulty and enormous risk associated with harvesting brain tissue from living patients, development of an efficient and replenishable model is paramount. Animal models have commonly been used to study human neurological diseases. However, animal brains develop differently to human brains and as such animal models of neurological diseases may not fully recapitulate the disease progression in human tissue. The use of human ESC/iPSC has facilitated the modelling of many neurological disorders including, but not limited to, amyotrophic lateral sclerosis (Dimos et al., 2008; Boulting et al., 2011), Huntington’s disease (HD)(Park et al., 2008), Parkinson’s disease (Soldner et al., 2009; Nguyen et al., 2011) and Rett’s syndrome (Marchetto et al., 2010; Cheung et al., 2011).

Furthermore, stem cells have huge possibilities in neurological disease therapy. Neurodegenerative conditions are associated with severe cell loss and effective therapies would therefore require effective cell replacement. Stem cells provide a potential source of neurons for use in such cell replacement therapies. However, and as already discussed above, there are concerns surrounding the pluripotent nature of the stem cells used in potential graft tissue. The use of WGE cells may alleviate some of this concern due to their limited potency. Indeed, grafting of hWGE cells into human HD patients has had some early promising results (Gaura et al., 2004; Reuter et al., 2008). Whilst limited potency is a vital characteristic, stem cell derived neurons used in grafts also need to accurately depict perhaps the most defining feature of neurons, their electrophysiological properties.

1.2 Electrophysiology: Basic principles and applications

1.2.1 Bioelectricity and electrophysiology

Neurons fall into a subcategory of cells within the body which are excitable. The term excitable refers to the ability of the cells to be electrically active and to generate action potentials. Neurons are not alone in this category, as muscle cells (smooth, cardiac and skeletal) and a small number of endocrine cells (pancreatic β cells) are also classed as excitable. The study of electrically excitable cells and their inherent bioelectrical properties is termed electrophysiology.

Neurons, like other cells, have a membrane made of a stable phospholipid bilayer, with a hydrophobic interior and hydrophilic exterior, separating the extracellular solution from the intracellular cytosol. The polar nature of the phospholipid bilayer renders it impermeable to large and charged particles. Inserted into this membrane are protein structures known as ion channels, selectively permeable to charged ions, facilitating the flow of ions across the phospholipid bilayer. Importantly these ion channels are often gated, whereby they only facilitate the passive diffusion of ions across the membrane when certain parameters are met. Another type of protein commonly found in the cell membrane are ion pumps, that facilitate the active movement of ion channels against the concentration gradient through the consumption of adenosine triphosphate (ATP). It is indeed this transport of charged ions that facilitate the electrical activity of neurons.

In order to understand the key concepts of electrophysiology a sound understanding of certain principles for physics is vital. Charge (Q) is measured in coulombs (C) and the rate of movement of charge is termed current (I), measured in $C.s^{-1}$, or amperes (A). According to the convention established by Benjamin Franklin, positive current flows in the same direction as the movement of positive charge. For example, placing positive (anode) and negative (cathode) electrodes in a solution containing cations (positively charged ions) and anions (negatively charged ions) would induce the moment of cations toward the cathode and the anions towards the anode, as opposite charges attract. It is therefore said that current flows from positive to negative, anode to cathode. Conductance of the solution and the potential difference between the electrodes determines the size of the current, *i.e.*, how fast ions move.

Potential difference, measured in volts (V) and otherwise termed voltage, is defined as the amount of work (measured in Joules, J) required to move a single unit of charge between two points. 1 J is required to move 1 C across 1 V difference. Conductance, measured in siemens (S), is considered to be the ease of flow of current between two points. The conductance between two electrodes in the earlier example could be increased by moving the electrodes closer together or by increasing the concentration of salt in solution. Decreasing the conductance could be achieved by increasing the solutions viscosity, distance between the electrodes or simply by placing an impermeable barrier between the two electrodes. Essentially, ion channels are conductors which facilitate the movement of ions across an otherwise impermeable membrane, the cell’s own phospholipid bilayer. The sum of the all conductors in parallel equal the total conductance of the membrane representing the number of open ion channels and the ease of passage through them. Conductance in simple conductors is defined by Ohm’s Law (Ohm, 1827):

$$I = gE$$

where I (current) is equal to the product of g (conductance) and E (voltage difference) across the conductor. Ohm’s Law is also seen represented using resistance (R), the reciprocal of conductance, measured in in ohms (Ω):

$$E = IR$$

Ohm’s Law is pivotal in understanding the movement of ions across cell membranes.

All that is required to generate a potential difference is the separation of charge via a capacitor. Capacitance (c), measured in farads (f), is the amount of charge (Q) transferred between two conductors to generate a defined potential. This can be written as:

$$c = \frac{Q}{E}$$

where c refers to capacitance. When + 1 C of charge is on one side of the capacitor and – 1 C charge is on another side of the capacitor, a 1 f capacitor between the two will be charged 1 V.

As the thin neuronal cell membrane separates two conducting solutions from each other, the extracellular solution and the neuronal cytosol, the cell membrane can be seen to act as a capacitor. Following on from this basic understanding of electrical concepts and seminal work in the giant squid axon, Hodgkin and Huxley proposed the Hodgkin-Huxley model cell (Bean, 2007) (simplified in Figure 1.1) to describe the electrical properties of excitable cells, for which they won the 1963 Nobel Prize for Medicine or Physiology (Hodgkin et al., 1963). When considering the ion channels as rudimentary conductors allowing ions to pass through them there is a resistance associated with them, that is the resistance through an ionic pore. It is for this reason ion channels are represented as resistors in the model cell.

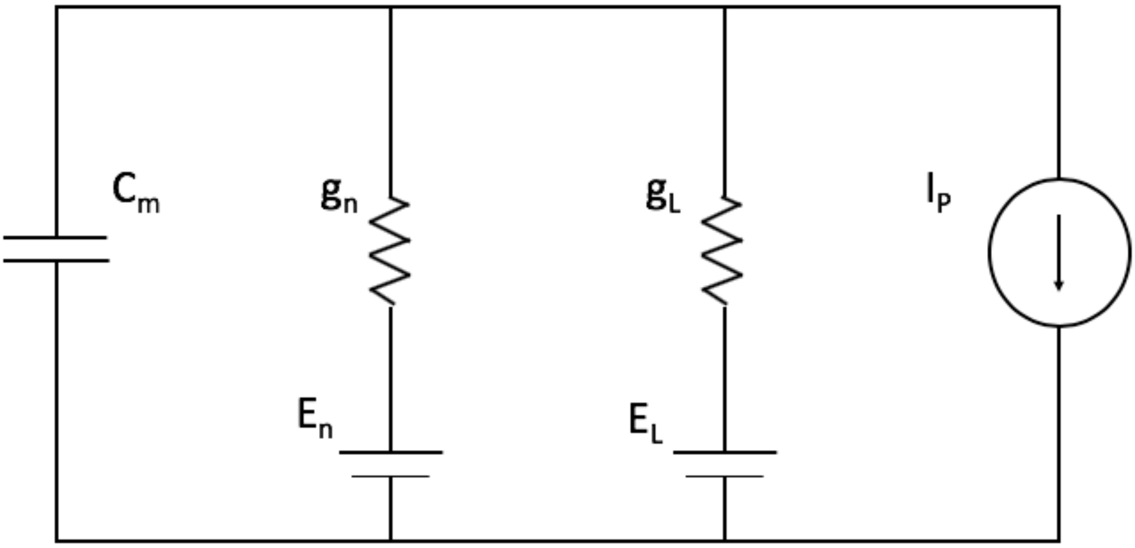

Figure 1.1: Basic components of the Hodgkin-Huxley model cell
The lipid bilayer is represented as a capacitor (C_m). Non-linear and linear resistors represent voltage gated channels (g_n) and leak channels (g_L) respectively, and are associated with the electrochemical gradient driving the flow of ions; shown as batteries (E_n & E_L). Ion pumps are shown here as current sources (I_P)

1.2.2 Equilibrium and membrane potentials

The resting membrane potential (V_m) of the neuron is the potential difference across the membrane at a given time. Typically, this value is at -65 mV in neurons in the central nervous system (CNS), which is to say the inside of the membrane is 65 mV more negative than the outside. For a negative V_m to arise the inside of the cell needs to be more negatively, or indeed less positively, charged relative to the outside of the cell. In neurons, this occurs through a balance between equilibrium potentials controlled by relative permeabilities, as described below.

For simplicity, the following four ions will be used to demonstrate the ions critical to neuronal function; Na^+, K^+, Ca^{2+}, Cl^-. In a situation where a solution of the four previously mentioned ions is separated, by an impermeable barrier, from a 25 times diluted sample of the same solution there would be no net movement. As such the V_m would equal 0 mV as the ratio of each ion to each other on either side of the membrane would equal 1. Inserting a channel selective to a single ion, K^+, would facilitate passive diffusion down the concentration gradient from intracellular to extracellular solution until equilibrium is met. Once in this state, the V_m at which the concentration of the ion is in equilibrium is known as the equilibrium potential (E_{ion}). If the extracellular and intracellular concentrations of the ion are known, then the E_{ion} can be calculated using the Nernst Equation:

$$E_{ion} = 2.303\frac{RT}{ZF}log10\frac{[ion]_o}{[ion]_i}$$

Which describes the relationship between the E_{ion}, the gas constant (R; 8.314 J K^{-1} mol^{-1}), the absolute temperature (T), the valency of the ion (z), the Faraday Constant (F; 9.654 x 10^4 C / mol) and the concentrations of the ions extracellularly ($[ion]_o$) and intracellularly ($[ion]_I$). Using this equation for the hypothetical situation described previously in which two solutions, the extracellular being twenty-five fold more diluted than the intracellular, are separated by an impermeable barrier only allowing K^+ diffusion at biological temperature (37 °C) the equation would look as follows:

$$E_K = 2.303\frac{RT}{ZF}log10\frac{[K^+]_o}{[K^+]_i} = 61.54\,mV\;log10\frac{1}{25} = \;-86.029\,mV$$

As shown above, the E_{ion} for K^+ is roughly -86 mV in this particular hypothetical situation. However, in neurons, the concentration gradient for each of the composite ions is not simply twenty-five fold. The following table describes the internal and external ion concentrations for the four most “important” biologically active ions, adapted from Lodish *et al.* (Lodish et al., 2000)*,* Bear *et al. (Bear et al., 2001),* and Hille (Hille, 1984):

Ion	Extracellular Concentration (mM)	Intracellular Concentration (mM)	Equilibrium Potential (mV)
Na^+	+ 146.667	+ 13	+ 64.764
K^+	+ 4.334	+ 131.334	- 91.171
Ca^{2+}	+ 1.5	< + 0.0001	+ 128.498
Cl^-	+ 129.667	+ 7.067	- 77.761

Table 1.1: Extracellular and intracellular ionic concentration of mammalian neurons
The concentrations of Na^+, K^+, Ca^{2+}, Cl^- intracellularly and extracellularly with respect to mammalian neurons on the CNS. Values taken from Lodish *et al*., Bear *et al*., and Hille and calculated using the Nernst Equation. All calculations performed at biological temperature (T = 37 °C or 310.15 K)

Averaging these equilibrium potentials generates a much higher value than the V_m seen in mammalian neurons of roughly -65 mV. Several factors contribute to this including relative permeabilities and ion pumps maintaining concentration gradients.

Maintenance of concentration gradients is due in part to the relative permeabilities, but also heavily due to ion pumps like the sodium-potassium pump. The sodium-potassium pump, the discovery of which won Jens Skou the 1997 Nobel Prize for Chemistry (Boyer et al., 1997) breaks down adenosine triphosphate (ATP) in the presence on intracellular Na^+ exporting it out across the membrane in exchange for extracellular K^+. Maintenance of these concentration gradients is vital for function of all living cells.

Ion channel permeabilities (P) are usually noted as relative to P_K due to it having a much larger permeability than P_{Na} and P_{Cl} . Typically, a neuron at rest is suggested to have permeability values as follows; $P_K : P_{Na} : P_{Cl} = 1 : 0.05 : 0.45$. Whilst Ca^{2+} invariably plays a role in neuronal bioelectricity, it's impact on membrane potential is comparably low due to low intracellular

(1.25 mM) and extracellular (< 0.0001 mM) concentrations and a much smaller permeability (< 0.01% of P_K)(Spangler, 1972). It is for these reasons that Ca^{2+} is not included in the Goldman-Hodgkin-Katz equation which incorporates relative permeabilities to calculate the V_m as follows:

$$V_m = 2.303\frac{RT}{F}log10\left(\frac{P_k[K^+]_o + \ P_{Na}[Na^+]_o + P_{Cl}[Cl^-]_i}{P_k[K^+]_i + \ P_{Na}[Na^+]_i + P_{Cl}[Cl^-]_o}\right)$$

Inserting the extracellular and intracellular concentrations as calculated in Table 1 and relative permeability values (P_K : P_{Na} : P_{Cl} = 1 : 0.05 : 0.45), generates a theoretical resting membrane potential similar to that seen in neurons at rest, as follows:

$$V_m = 61.54\,mV\ log10\left(\frac{4.334 + \ 7.334 + 3.18}{131.334 + \ 0.65 + 58.35}\right) = \ -68.177\,mV$$

1.2.3 Electrochemical communication via action potentials and synaptic transmission

Electrochemical communication in mammalian neurons relies on manipulation of these membrane potentials and ion channels. Ion channels themselves can be gated by both ligands and/or membrane potential, whereby a ligand binding or the membrane potential changing induces a conformational change to facilitate the passage of ions through the pore. For example, in voltage gated Na^+ channels three states of 'activation' exist: closed, open and, inactivated. Whilst in closed and inactivated, the channel remains impermeable to ions. Whilst V_m = ~ - 70 mV, voltage gated sodium channels are in their closed state where the activation gates block the pore extracellularly. Upon electrochemical stimulation, these activation gates undergo conformational change to facilitate the passage of ions through the pore, transitioning from closed to open state, i.e. activation. In the open state Na^+ continues to pass through the pore depolarising the membrane, facilitating the activation of other nearby voltage gated sodium channels. Following depolarisation of the membrane the inactivation gate then conformationally alters to render the pore impermeable to Na^+ and therefore in its inactivated state. The transition from inactivated to closed is time dependant. An action potential (neuronal) is a rapid reversal of potential across a membrane, largely dependent on Na^+ and K^+ channels, facilitating the passage of information from one point to another in the mammalian nervous system. A detailed exploration of all the facets of mammalian action potentials is outside the scope of this introduction to the basics of electrophysiology, but see Bean (Bean, 2007) for a detailed review. However, a brief explanation follows below.

At rest, the membrane potential is maintained at roughly -65 mV via Na^+/K^+ pumps and leakage channels. The Na^+/K^+ pump generates a high intracellular concentration of K^+ and low intracellular concentrations of Na^+. As the neuronal membrane is considerably more permeable to K^+, K^+ diffuses out of the neuron at a much faster rate than Na^+. The efflux of cations results in the interior of the cell being more negatively charged relative to the outside of the cell. Following a stimulus (ligand/mechanical/electrical) Na^+ influx through open Na^+ channels begins to depolarise the membrane. An action potential is only generated when the membrane continues to depolarise past a specific potential, termed threshold potential, of between -50 and -55 mV (Bostock et al., 1998) at which the voltage gates Na+ channels activate and become ‘open’. Once this threshold potential is passed voltage gated Na^+ channels open, increasing the Na^+ conductance across the membrane and facilitating the rapid depolarisation associated with the rising phase of the action potential (Fig.1.2). During the rising phase, as the Na^+ conductance is increased, V_m is brought closer to E_{Na} and further from E_K. Gradually, this increased voltage begins to inactivate voltage-gated Na^+ channels, reducing the Na^+ conductance relative to potassium conductance slowing the rate of increase of V_m. The increased V_m then fully inactivates voltage-gated Na^+ channels, at the peak of the overshoot, then causes the activation of voltage-gated potassium channels, increasing the potassium conductance and facilitating the falling phase of the action potential. During the falling phase V_m rapidly repolarises, towards E_K. Voltage-gated potassium channels are comparatively slow to shut and are thus associated with afterhyperpolarisation of the membrane, which is negative of the resting V_m and closer to E_K. This period of hyperpolarisation is frequently termed the undershoot, afterhyperpolarisation or refractory period. During the refractory period, the voltage-gated Na^+ channels are inactivated and thus the Na^+ influx responsible for the rising phase of the action potential cannot occur, this is termed the absolute refractory period. Following removal of the N^+ channel steady state inactivation there is still an increased K^+ conductance due to the slow to inactivated voltage gated Na^+ channels. This period is associated with a greatly increased threshold potential due to the increased Na^+ conductance and is termed the relative refractory period. It is for these reasons that, under normal circumstances, action potentials cannot fire during the refractory period.

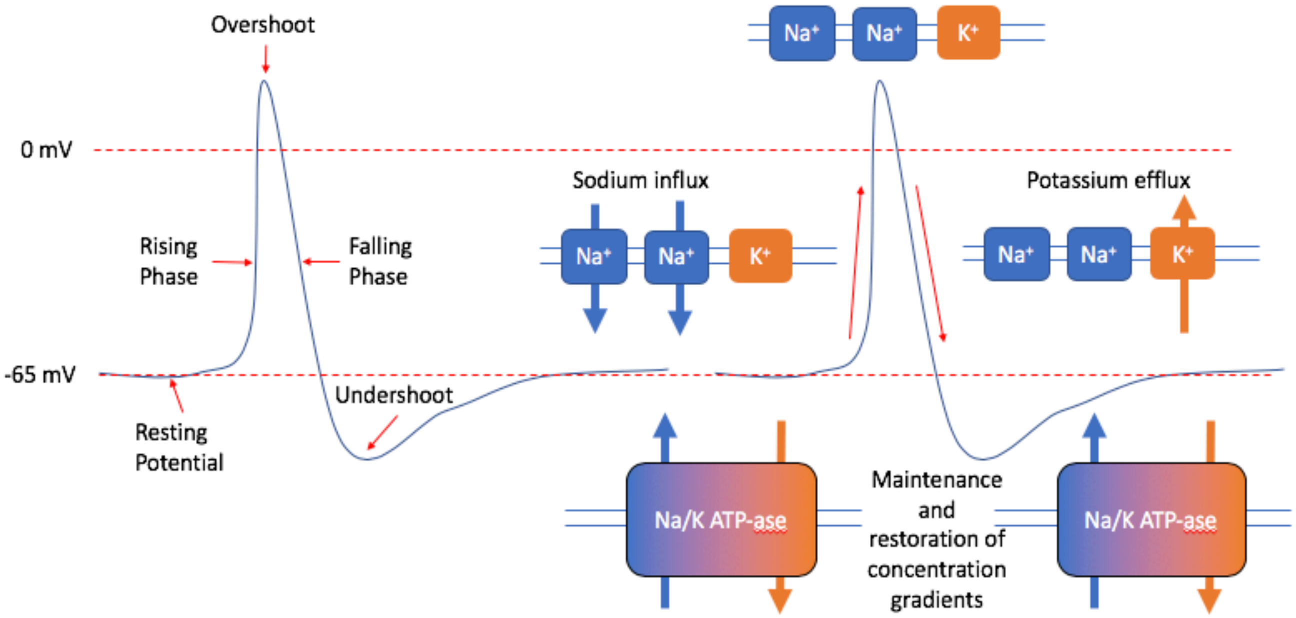

Figure 1.2: Simplified action potential is largely controlled by sodium and potassium conductance The classical action potential shape is brought about largely by Na^+ and K^+ conductances. The influx of Na^+ ions facilitates the sharp rising phase of the action potential, whilst the K^+ ion efflux facilitates the repolarization and therefore falling phase of the action potential. Due to the relative latency of the closing of potassium channels, an undershoot (otherwise termed refractory period) is formed which is corrected through Na^+/ K^+ ATP-ase pumps.
Abbreviations: Na: sodium, **K:** potassium, **ATP:** adenosine triphosphate

As the entire neuronal membrane is excitable, and the length of the neuronal axon is not separated into distinct compartments, action potentials are able to propagate along the length of the neuronal axon. As positively charged sodium ions rush into the axonal cytoplasm, this positive charge diffuses along the axon gradually depolarising the adjacent patch of membrane. Should this be sufficient to pass the threshold potential the voltage gated Na^+ channels open in this patch and initiate another action potential, and thus the chain continues along the length of the axon (Fig.1.3). Cable theory is the mathematical set of models that aim to describe this phenomena in excitable cells. Hermann first described the spread of action potentials using the theory for a “leaky telegraph cable” (Hermann, 1905).Here the neuronal axons are considered as cylindrical compartments with capacitances and resistances combined in parallel. This conduction is termed orthodromic due to the patch of membrane behind the action potential being in a refractory state, driving the propagation along the axon in one direction. Usually action potentials initiate in the axonal hillock as the result of various stimuli, and then travel the length of the axon toward synapses and initiate synaptic transmission.

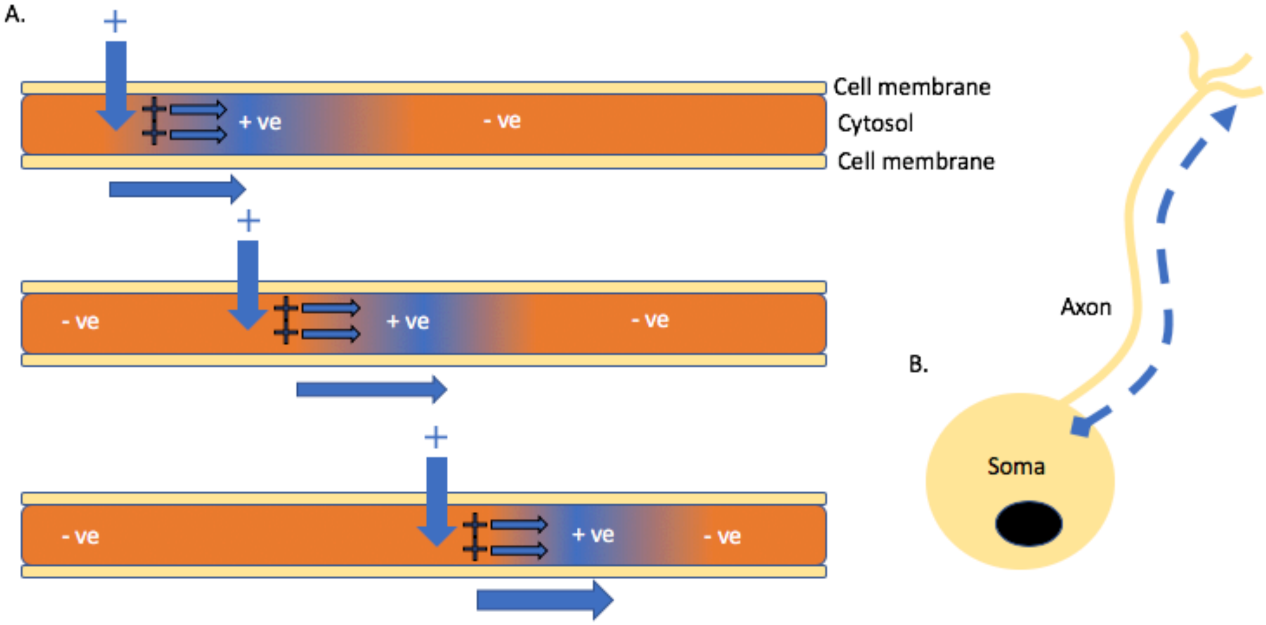

Figure 1.3: Action potential propagation along the neuronal membrane
A: The inside of the cell is relatively more negative (orange) than the external solution. As sodium ions flood into the cell, the patch around this region is gradually depolarized, or made less negative/more positive (blue). This patch of more positive membrane, if more positive than the membrane’s threshold potential, will be sufficient to trigger an action potential in the adjacent patch.
B: This movement continues along the axon of the neuron towards the synapse.
Abbreviations: **+ve:** positive, **-ve:** negative

Synaptic transmission facilitates rapid information transmission across large distances and multiple neurons. Most synaptic transmission within the mammalian nervous system is via chemical synapses; electrical synaptic transmission at specialised gap junctions made up of connexons is an exception to this rule (Hormuzdi et al., 2004). A chemical synapse is a specialised junction between two axons consisting of a presynaptic element, the synaptic cleft and the postsynaptic element. The presynaptic element contains large numbers of vesicles containing neurotransmitters such as Acetylcholine, Dopamine, Noradrenaline, Gamma-aminobutyric acid (GABA), Glutamate and Glycine. Each vesicle has multiple vesicle Soluble N-ethylmaleimide-sensitive factor Attachment protein REceptors (v-SNAREs) which interact with target-SNAREs (t-SNAREs) on the internal surface of the presynaptic terminal membrane. Release of synaptic vesicles is largely mediated by Ca^{2+} influx through voltage-gated calcium channels that activate upon membrane depolarisation as a result of an action potential reaching the presynaptic terminal. This influx of Ca^{2+} facilitates the binding of v-SNAREs to t-SNAREs through interaction with synaptotagmin to form a trans-SNARE complex. The formation of this trans-SNARE complex draws the membranes of the neurotransmitter vesicle and the presynaptic terminal so close that they fuse and release the neurotransmitters contained in the vesicle into the synaptic cleft via endocytosis.

Postsynaptic neuronal membranes, possess cell-specific arrays of neurotransmitter receptors. For example, in the case of α-amino-3-hydroxy-5-methyl-4-isoxazolepropionic acid (AMPA) receptor (AMPAR)-mediated synaptic transmission, the presynaptic element would contain Glutamate and the postsynaptic element would possess AMPARs. AMPARs are transmembrane proteins consisting of four subunits (GluR1-4) that assemble into ionotropic receptors (Greger et al., 2017) that allow passage of Na^+ and K^+ with equal permeability upon Glutamate binding to AMPAR ligand binding domains. This increased conductance to both Na+ and K+ drives the V_m towards E_{Na} (67.674 mV) and E_K (-91.171 mV) equally, thus driving V_m towards 0 mV, depolarising the membrane which, in turn, activates voltage-gated sodium channels to generate action potentials on the postsynaptic neuron. This transient depolarisation of the post-synaptic neuron as a result of presynaptic neurotransmitter release and is termed an excitatory post synaptic potential (EPSP).

Of particular interest is GABAergic signalling, as medium spiny neurons (MSNs) are the predominant type of neuron found in the striatum and are thought to be GABAergic inhibitory neurons (Gonzales et al., 2013). The majority of neurotransmitters are either seen as excitatory or inhibitory, yet GABA can function as both. GABA binds to $GABA_A$, a Cl^- selective ligand gated ion channel. In immature neurons the Cl^- levels are more concentrated intracellularly than extracellularly, whilst in mature neurons the opposite is true. This switch in Cl^- concentrations is largely controlled by relative expression of Cl^- transporters. In immature neurons the expression of the Na^+/Cl^- cotransporter (NCC) and $Na^+/K^+/Cl^-$ cotransporter (NKCC) is upregulated, resulting in a net influx of Cl^-. In more mature neurons the K^+/Cl^- cotransporter (KCC) and $Na^+/HCO_3^-/Cl^-$ exchanger (NDCBE) are upregulated resulting in a net efflux of Cl^-. In immature neurons, with a higher intracellular concentrations of Cl^-, GABA binding to $GABA_A$ opens the pore facilitating the passage of Cl^- down the concentration gradient. This efflux of negatively charged Cl^- causes the inside of the neuron to become less negative or depolarised. GABA is therefore excitatory in immature neurons. In mature neurons GABA binding to $GABA_A$ induces a net influx of Cl^-, resulting in a hyperpolarisation of the membrane. Furthermore, GABA itself has been shown to drive the transition from excitatory to inhibitory via regulation of messenger ribonucleic acid (mRNA) levels of KCC (Ganguly et al., 2001).

1.2.4 Application of theoretical principles

Recording these electrochemical signals has taken many forms and has progressed rapidly from relatively simple glass electrode, as used by Hodgkin and Huxley in the giant squid axon (Hodgkin, 1952), to complex *in vivo* multi-electrode arrays. Visualisation of any electrophysiological activity is a simple application of the theoretical principles outlined above. Multiple 'patch' techniques involving a glass micropipette exist and are broadly divided into whether the patch of membrane remains attached to the cell or whether it becomes excised.

Recordings made whilst the electrode is attached to the cell can be further divided into 'cell-attached', 'whole cell' and 'perforated patch'. Cell-attached recordings involve a glass micropipette with a very fine tip diameter of between 1-3 μm. This micropipette is filled with a conducting solution, made to mimic the extracellular solution, and houses an electrode inside the micropipette capable of simultaneously stimulating and recording. The tip must be brought in close contact with the neuronal cell, close enough to form a 'giga-seal' where the resistance between the tip of the electrode and neuronal membrane is in the order of giga-ohms (GΩ). Formation of the 'giga-seal' allows for isolation of the electrical activity seen across the patch of membrane under the tip from any electrical noise, as well as providing mechanical stability to the recording.

During cell attached experiments, the experimenter leaves the membrane intact and therefore gains access to the conductance properties of a single or very few surface receptors and ion channels. This technique is relatively non-invasive as the membrane and intracellular processes are unaffected so it therefore more representative of the cell under physiological conditions. By the same measure leaving the membrane intact does not allow manipulation of the internal solution and intracellular solutions. Cell-attached patch recordings are best employed when characterising single ion channel properties.

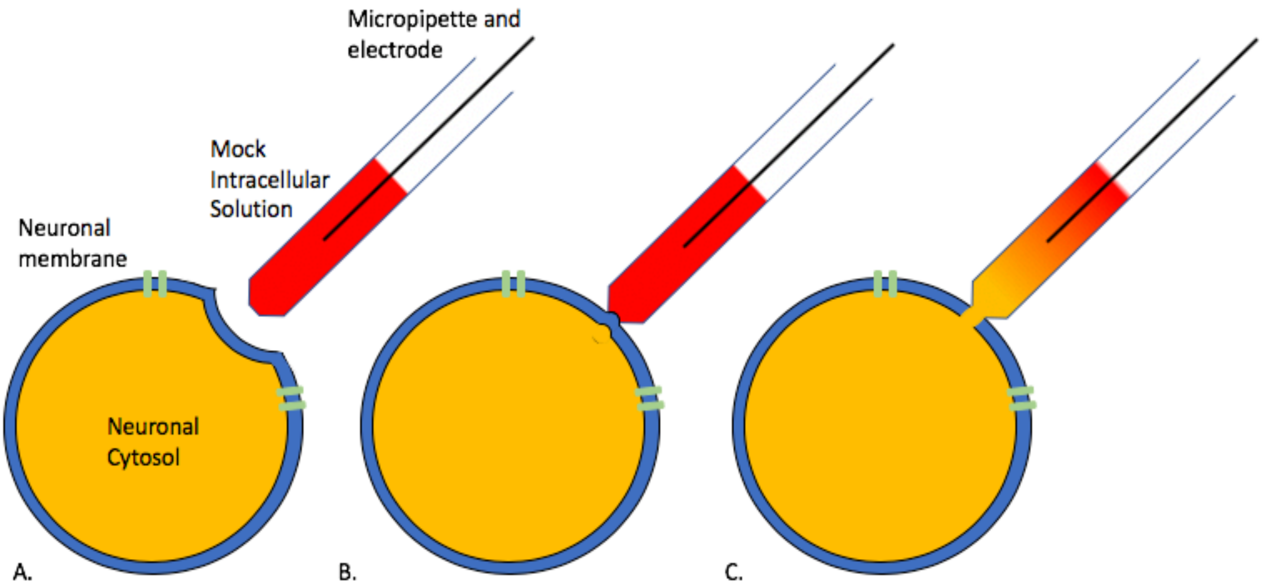

Figure 1.4: Formation of the whole cell patch clamp configuration
A: Positive pressure is applied through the tip of the micropipette which forms a 'halo' on the membrane (thick blue) of the neuron (yellow/blue) to be patched.
B: When the micropipette, containing aCSF (red) and the electrode (black), is sufficiently close to the cell surface the positive pressure is released and the neuronal membrane is pulled close to the tip of the micropipette. If done correctly this will lead to the formation of a gigaseal.
C: Negative pressure, usually applied in the form of suction, is applied to the micropipette which ruptures the patch of membrane beneath the tip of the micropipette facilitating mixing of the neuronal cytosol (yellow) and the aCSF (red). This will allow the cell to be dialysed, thus the large pipette volume compared to cell volume ensures that the inside of the cell becomes filled with the pipette solution over a period of several minutes.
Abbreviations: aCSF: artificial cerebrospinal fluid

Whole cell recordings follow a similar sealing protocol, however involve rupturing of the patch of membrane beneath the tip. Following formation of the 'giga-seal' a small patch can be ruptured allowing the micropipette tip and neuronal cell membrane to seal and facilitate mixing of the two solutions (Fig.1.4). Importantly, the solution in the pipette now is made to mimic the intracellular solution. By placing a reference electrode in the external solution the voltage can be measured internally (V_i ; by the electrode in the micropipette and subsequently mixed solutions) and externally (V_o ; 0 mV by convention; by the reference electrode) allowing visualisation of V_m as follows:

$$V_m = V_i - V_o$$

If a patched neuron then fires an action potential, this can be visualised as the membrane potential would rapidly depolarise and repolarise giving rise to the classical shape of an action potential. Action potentials can be recorded spontaneously in a current clamp configuration where I = 0 or can be induced through utilising the electrode as both a stimulating and recording electrode in current step protocols. Here, in a current step protocol, sequentially more positive currents can be injected to depolarise the cell to induce action potentials. Patch

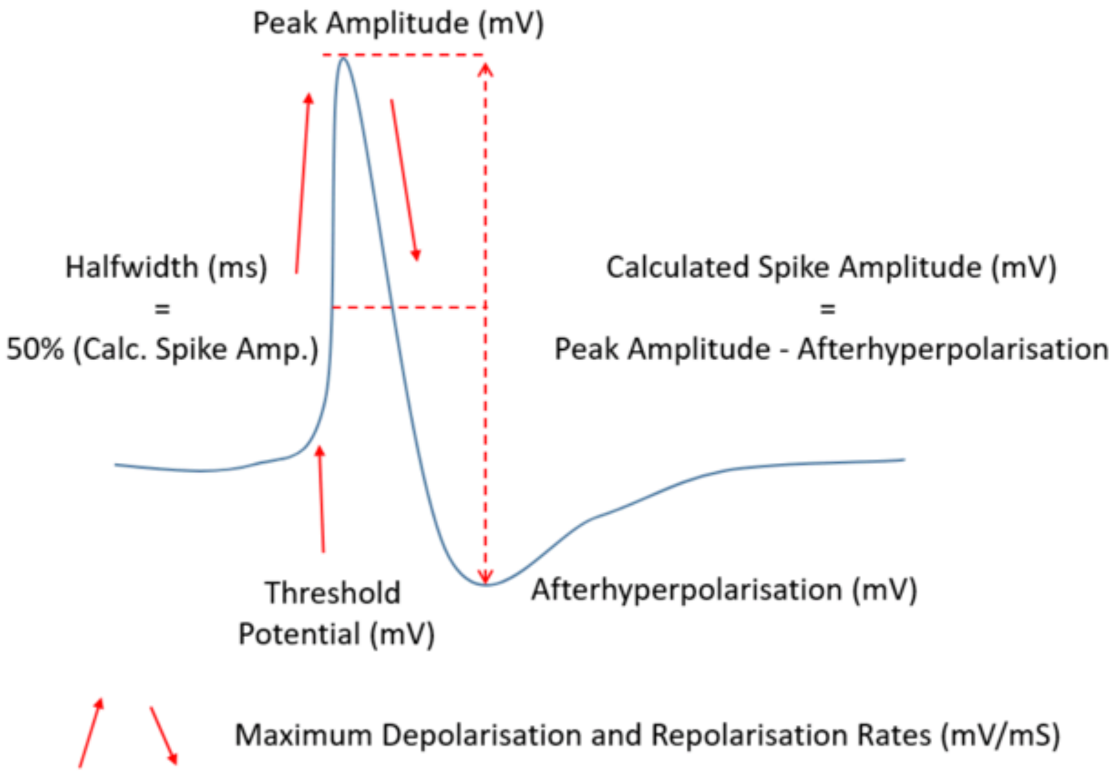

Figure 1.5: Action potential properties revealed during whole cell patch-clamp experiments
During whole cell patch clamp experiments, fluctuations in membrane potential can be observed allowing visualization of the classical action potential shape and dissection of it's properties. The threshold potential is the minimum potential required for generation of a full action potential. The halfwidth is then taken as the action potential width at 50% maximal amplitude, which is calculated as the afterhyperpolarization value minus the peak amplitude. The maximum depolarization and repolarization rates are taken as the rate of change in voltage over seconds of the rising and falling phases respectively.

clamp is widely used to investigate synaptic function and can be applied *in vitro* to cultured neurons (Telezhkin et al., 2016), *in vivo* in anaesthetised animals (Tao et al., 2015) and *ex vivo* in tissue slices (Reidling et al., 2018). This technique grants unprecedented access to the membrane properties of an entire cell at rest, during an action potential (Fig.1.5) and throughout synaptic communication. For example, voltage clamp. During voltage-clamp experiments, the experimenter is 'clamping' V_m to a command potential (V_{comm}) by continuously injecting a current to maintain this V_m. As the current being injected has to be equal to the current passing the membrane at any one time, it is therefore possible to record how the cell responds to changes in V_m. The drawbacks associated with whole cell patch clamp recordings include the invasive nature of whole cell recordings and subsequent impact on intracellular processes. Furthermore, whole cell patch clamp can struggle to capture network activity as the recordings are of single cells.

The last of the patch recordings where the cell remains attached to the micropipette is 'perforated patch'. Perforated patch is very similar to cell-attached recordings whereby the membrane is not ruptured by the user, however is perforated by pore forming antibiotics such as amphotericin-B or nyastatin in the pipette. This technique grants the user access to the properties of the entire cell as in 'whole-cell' recordings, however is less invasive and disruptive of the intracellular solution and mechanisms. This technique is best employed when the whole cell properties are required however the impact of intracellular mechanisms is thought to have a larger impact on the question being answered. A drawback of this method is the higher access resistance caused the partial membrane left under the pipette which could potentially increase noise, furthermore continued exposure to the pore forming antibiotics could weaken the membrane to the point that the membrane ruptures. When this occurs, the recording is then a whole-cell patch recording, where the internal solution is then contaminated by whichever pore forming antibiotic was used.

The type of recordings made whereby the cell is no longer attached, and is therefore termed excised, can be divided into ‘inside-out’ and ‘outside-out’. Both recordings follow a very similar technique to whole-cell recordings, yet differ in how the membrane is ruptured. During inside-out recordings following gigaseal formation, the pipette is slowly withdrawn to break a patch of membrane loose from the cell being patched. A vesicle often forms here, which is often ‘popped’ by rapid transition through the air-liquid interface. The patch of membrane within the tip of the pipette remains intact, thereby exposing the internal surface of the cell to the extracellular solution. Doing so allows investigation of the effect of various intracellular ligands on the ion channels via perfusion through the bath solution. Outside-out recordings are very similar but involve rupturing the patch of membrane between the tip of the pipette to achieve a whole-cell configuration, then withdrawing the pipette slowly so that the membrane blebs forming a vesicle on the tip of the pipette. The internal surface of this vesicle being the external surface of the cell, and the external surface of the vesicle being the internal surface of the cell. This technique affords the experimenter the unique ability to interrogate the properties of one, or a few, channels in isolation from the rest of the cell.

Extracellular recordings are recordings made where no contact is made with the membrane of the cells being recorded and are therefore visualisation of a population of neurons in close proximity to the tip of the pipette. Extracellular field potential recordings performed on slices of brain tissue use a very similar micropipette and electrode to those used in whole cell patch clamp recordings. However, these electrodes are filled with a solution that mimics the extracellular solution, most commonly cerebrospinal fluid (CSF). The micropipette, when placed close enough, can record neuronal activity as a consequence of the mass movement of charges during depolarisation across a population of neurons in close proximity; these are termed field-EPSPs (fEPSPs). It is also common during extracellular recordings to place a stimulating electrode nearby, allowing visualisation of evoked field potentials in order to examine connectivity between the stimulated region and the region being recorded. Figure 6 compares the experimental set up of whole cell patch clamp experiments to extracellular field potential recordings. Due to extracellular field potentials recording information simultaneously from a population of neurons, the data gained does not provide the detail that whole cell patch clamp recordings can provide. The technique does require less skill than whole cell patch clamp recordings, however it is still comparatively user intensive and slow.

Multielectrode arrays (MEAs) aim to circumvent the time problem of the two previously described methods by allowing for long term, non-cell-invasive visualisation of neuronal activity from multiple populations of neurons simultaneously. Multiple types of 'plates' exist for *in vitro* culture neurons, *ex vivo* slices and more recently *in vivo* in live animals (Spira and Hai, 2013). A 'plate' here referring to a bed of electrodes of varying number and profile from the plate; slice MEA recordings required electrodes with a higher profile from the plate to record from the three-dimensional brain slice. These plates work very similarly to manual user-controlled experiments, recording electrodes subtracting differences in voltage

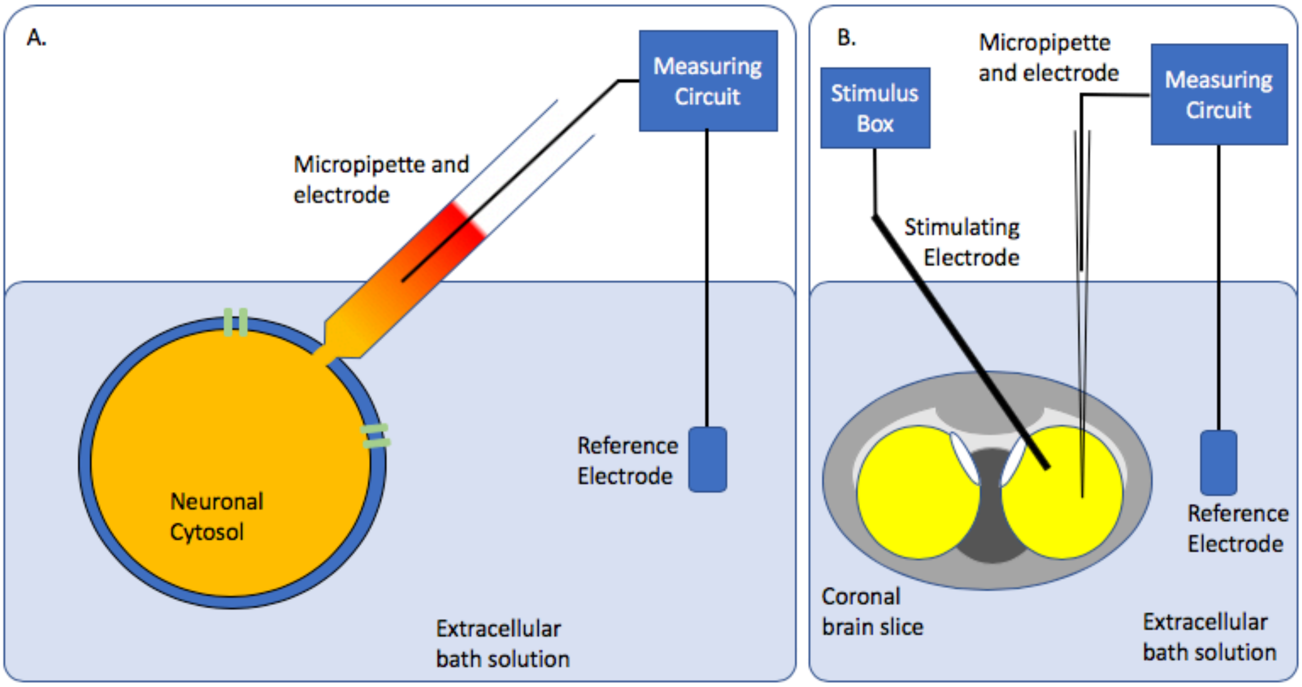

Figure 1.6: Simplified experimental set ups during whole cell patch clamp and extracellular field potential recordings
A: Whole cell patch clamp experiments require the tip of the micropipette to be sufficiently close the the neuronal membrane that a gigaseal can be created, the patch of membrane ruptured and mixing of neuronal solution and aCSF. The recordings electrode is then connected to measuring circuit which is simultaneously recording the potential difference in the bath solution and subtracting to the two to calculate the membrane potential.
B: Extracellular field potential recordings are similar in respect to the recording electrode and reference electrode however the micropipette only needs to be in the vicinity of the neurons it intends to record the potential differences in the local area as a result of sodium and potassium conductances. A stimulating electrode is also common to record evoked field potentials.
Abbreviations: aCSF: artificial cerebrospinal fluid

recorded from populations of neurons from a reference electrode, but are long-term in the sense that neurons can be cultured directly onto a plate containing 'X' amount of fixed position recording electrodes (Fig.1.7). This technique is so commonly used that commercially available kits are now available to streamline the whole process. Whilst vastly quicker, MEA experiments effectively ignore potential changes below an arbitrarily set threshold lending some bias and also do not provide the similar levels of detail to that recorded during whole cell patch clamp.

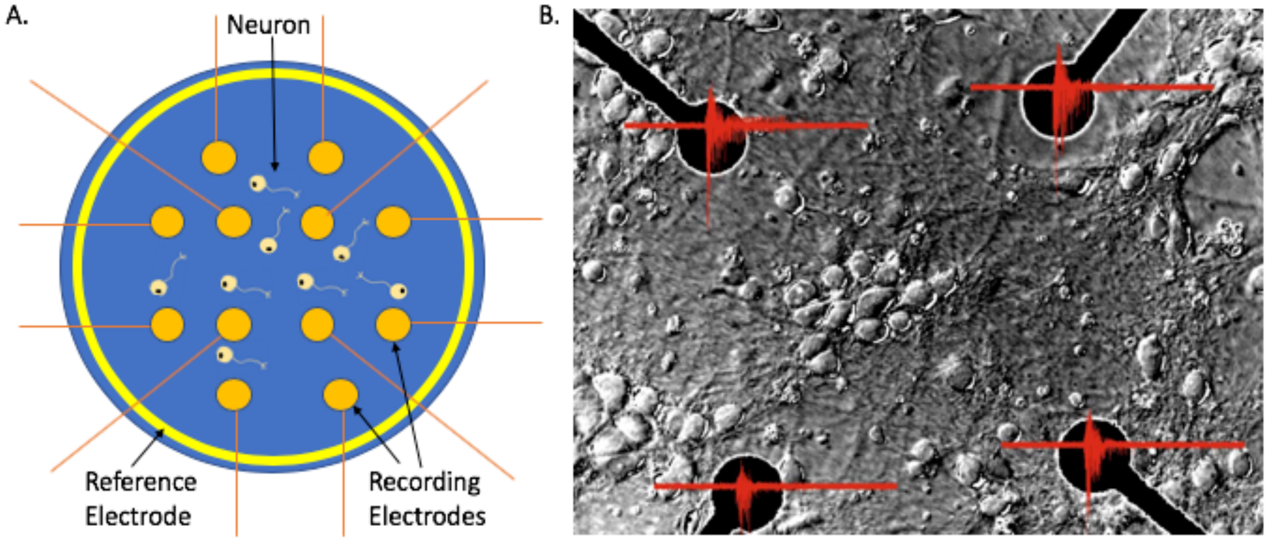

Figure 1.7: Simplified MEA recording
A: Overview of a single multi-electrode array well with twelve recording electrodes (orange) and one reference electrode (yellow).
B: Exemplary image showing neurons cultured on an MEA well and four recording electrodes present (black). Overlaid in red are exemplary traces of the extracellular field potentials recorded at each electrode. Adapted from (https://www.multielectrodearrays.com/)
Abbreviations: MEA: Multi-electrode arrays

1.3 Overall aims of the MPhil

Neurological diseases have a devastating impact on those whom they inflict. The impact of defects within the CNS on patients can range from memory loss and behavioural changes to epileptic attacks and seizures. Rarely are neurological disorders not life limiting, and more often than not are fatal. As such, research into neurological diseases is vital. Due to the difficulty in obtaining human neural tissue, stem cells are an invaluable resource in not only modelling neurological disorders but also in disease therapy. In these neurological diseases, neuronal function is impaired in myriad ways. The best technique to interrogate the functional properties remains electrophysiology. The aims of this project are to assess electrophysiologically the use of stem cells in: i) disease modelling, using h-iPSCs derived from patients with the epileptic condition, CDKL5-deficiency, and; ii) cell replacement therapy, following engraftment of h-ESCs into the striata of rats subjected to striatal lesions in order to model the fatal neurodegenerative condition, Huntington's disease.

Chapter 2 – General Methodology

2.1 Cell Culture

Synaptojuice A/B Protocol. All cells, across both the Repair HD and CDKL5 projects, were exposed to a rapid maturation protocol prior to whole-cell patch-clamp recordings. This protocol was published by Telezhkin *et al.,* (Telezhkin et al., 2016) and is commercially available as Synaptojuice. Cells were plated on poly-D-lysine (PDL) (Sigma) treated 22mm circular glass coverslips in Synaptojuice A, which contained; Advanced DMEM:F-12 (with Glutamax), 1 % penicillin/streptomycin, 2 % NeuroBrew21 (Miltenyi Biotec), 2 µM PD0332991 (Selleckchem), 10 µM DAPT (Sigma), 0.6 mM $CaCl_2$ (Sigma), 200 µM ascorbic acid (Sigma), 10 ng/ml BDNF (Miltenyi Biotec), 1 µM LM22A4 (Tocris Bioscience), 10 µM forskolin (Tocris Bioscience), 3 µM CHIR 99021 (Tocris Bioscience), and 300 µM GABA (Tocris Bioscience). Cells were then maintained in Synaptojuice A for 7 DIV. At 7 DIV, the medium was switched to Synaptojuice B, which contained: 1:1 Advanced DMEM/F-12 (with Glutamax):Neurobasal A (Life Technologies), 1 % penicillin/streptomycin (Life Technologies), 2 % NeuroBrew21 with retinoic acid (Miltenyi Biotec), 2 µM PD0332991 (Selleckchem), 3 µM CHIR 99021 (Tocris Bioscience), 0.3 mM $CaCl_2$ (Sigma-Aldrich), 200 µM ascorbic acid (Sigma-Aldrich), 10 ng/ml BDNF (Miltenyi Biotec), and 1 µM LM22A4 (Tocris Bioscience). The cells in the Repair HD arm of the project were maintained in Synaptojuice B for the following 14-21 DIV. LM22A4, CHIR 99021 and BDNF are all direct or indirect inhibitors of GSK3β, and as GSK3β is thought to be central in CDKL5 pathogenesis it was hypothesized that the GSK3β modulators present in Synaptojuice B might be masking a disease phenotype. Therefore, half of the cells in the CDKL5 arm of the project were then switched to a Synaptojuice B media at DIV14, not containing LM22A4, CHIR 99021 and BDNF hereby referred to as Reduced Synaptojuice, in an effort to reveal the disease phenotype.

2.2 Slice preparation

Lister hooded rats (Charles River) were anaesthetised with 4 µL of ketamine (Chanelle Pharmaceuticals Manufacturing Ltd., Ireland) and 2 µL of xylazine, (Bayer, UK) injected intraperitoneally in the lower abdomen, in order to preserve the intrastriatal field potentials. Reflexes were checked and, once absent, animals were culled via cervical dislocation by a colleague holding the appropriate Home Office Personal Licence and in accordance with Home Office regulations. Following removal of the head, the brain was removed, taking care not to damage the cortex or striatum. The brain was then immediately submerged in an ice-cold sucrose cutting solution containing (in mM): 189 Sucrose (VWR Chemical, Leicestershire, UK), 10 D-Glucose (Fisher Scientific), 26 $NaHCO_3$ (Sigma Aldrich), 5 $MgSO_4.7H_2O$ (Fisher Scientific), 3 KCl (Fisher Scientific), 0.1 $CaCl_2$ (Fisher Scientific) and 1.25 NaH_2PO_4 (Fisher Scientific) bubbled continuously with a 95 % O_2 / 5 % CO_2 gas mixture. From this step forward, the solution in which the brain/slices were submerged was subject to continuous bubbling with 95 % O_2 / 5 % CO_2 gas.

Following rapid cooling in sucrose, the cerebellum was removed with a surgical scalpel and the remaining brain glued onto a stage of an Integraslice PS765 (Campden Instruments, UK) equipped with ceramic blades (Campden Instruments, UK). 400 µm thick coronal slices were cut, submerged in the ice-cold sucrose cutting solution. Slices were then transferred to a storage container submerged in artificial cerebrospinal fluid (aCSF) containing (in mM); 124 NaCl (Fisher Scientific); 3 KCl (Sigma Aldrich); 24 $NaHCO_3$ (Fisher Scientific); 1.25 NaH_2PO_4 (Fisher Scientific); 1 $MgSO_4.7H_2O$ (Fisher Scientific); 10 D-Glucose (Sigma Aldrich); 2 $CaCl_2$

(Fisher Scientific). Slices were then left to recover at 37 °C for 45 minutes and then to stabilise for 60 minutes at room temperature prior to electrophysiological recording.

2.3 Two Photon Bioluminescent Imaging

Experiments were conducted in a commercially available PhotonIMAGER^{TM} Optima (Biospace Lab, Nesles la Vallé, France) system interfaced to a personal computer running Photo Acquisition (Biospace Labs) and M3Vision (Biospace Labs) software. For green fluorescent protein (GFP) imaging, slices were imaged for 2 minutes in the aCSF. Slices were then exposed to a solution of D-Luciferin cell penetration formula containing in M; 0.001 D-Luciferin, 1 $Na_3C_6H_5O_7$ (Sigma) brought to a final pH of 5.0 with acetic acid (Sigma). The slices were then imaged for 20 minutes to visualise bioluminescence.

2.4 Electrophysiology

Whole cell patch-clamp in culture. Whole cell patch-clamp recordings in culture were obtained using a Multiclamp 700A amplifier (Molecular Devices, Sunnyvale, CA, USA), digitised through a Digidata 1332A A/D convertor (Molecular Devices) and visualised on a connected personal computer running pClamp 9 (Molecular Devices) in a temperature controlled room set to 22 ± 0.5 °C. Signals were low-pass filtered at 2 or 5 kHz using and 8-pole Bessel filter and were digitised at 10 kHz. . Recordings were made on neurons in extracellular solution containing the following (in mM): 135 NaCl (Fisher Scientific, Loughborough, UK); 5 KCl (Sigma-Aldrich, Poole, UK); 5 HEPES (Sigma-Aldrich), 10 D-Glucose (Fisher Scientific); 1.2 $MgCl_2$ (Sigma-Aldrich); 1.25 $CaCl_2$ (Sigma-Aldrich); pH adjusted to 7.4 with NaOH. Cultured neurons were left to stabilise for at least 30 minutes prior to recordings.

Recording pipettes were pulled on Flaming Brown P-87 horizontal micropipette puller (Sutter Instrument Co, California, USA) from thin-walled glass capillaries (with internal filament, 1.0 mm internal diameter, 6" long cut in two with diamond tip cutter; World Precision Instruments, Florida, USA). Pipette resistance was between 3 and 8 MΩ when initially immersed into the bath solution. A standard pipette solution was used in all experiments containing (in mM); 10 NaCl, 11 HEPES, 117 KCl, 2 $MgCl_2$, 1 $CaCl_2$ 2 Na_2-ATP (Sigma-Aldrich), 2 Na-GTP (Sigma-Aldrich), 1.2 Na_2-phosphocreatine (Sigma-Aldrich) and 11 EGTA (Fisher); pH was adjusted to 7.2 with KOH.

Protocols used to interrogate membrane properties of cultured neurons were identical to those used by Telezhkin *et al.* (Telezhkin et al., 2016) and are described as follows. Following GΩ seal creation and membrane rupture, resting membrane potential (mV) was determined in a 'gap-free' protocol in current clamp mode (I = 0) as was the presence of any spontaneous action potentials. Spontaneous activity was then defined as either; 1. quiet (no activity, no significant deviation from the mean), 2. attempted (attempted activity, significant deviation from the mean not resulting in full depolarisation), 3. spontaneous (full spontaneous activity resulting in full depolarisation*, i.e.* passing 0 mV). Current was injected to hyperpolarise the cell to approximately -70 mV before a current-step protocol injected current in increments of 10 pA from -10 to +180 pA. Input resistance (MΩ) was then measured as the mean voltage difference between following -10 pA injection. The presence of any induced activity was determined and defined as; 1. quiet (no significant deviation from the mean), 2. attempted activity (significant deviation from the mean not crossing 0 mV), 3. single action potential (significant excursion from the mean resulting in depolarisation of the cell past 0 mV), 4. single action potential attempting train (single action potential followed one or more attempted action potentials), 5. train of action potentials (more than one successful action potential crossing 0 mV in close proximity to one another).

In the presence of induced action potentials, the first action potential following injection of current underwent spike analysis. The following parameters were then extracted; peak amplitude (mV), afterhyperpolarisation (mV), calculated spike amplitude (mV), depolarisation rate (mV/s), repolarisation rate (mV/s), half-width (ms), threshold potential (mV). A detailed description of the process used to extract each parameter is defined in Chapter 3 of this thesis.

Na^+ and K^+ currents were then recorded using a voltage-step protocol in the voltage clamp configuration using an initial holding potential of - 70 mV. The potential was then stepped from the holding potential to potentials ranging from - 120 mV to + 80 mV in 5 mV increments, with each sweep allowing visualisation of the Na^+ activation current (pA). This was followed by stepping to 0 mV for a further 80 ms, to visualise the Na^+ inactivation current (pA), before returning to the holding potential of - 70 mV. K^+ currents (pA) were taken from the final 50 ms prior to stepping to 0 mV. Cell capacitance (pF), allowing for calculation of current densities (pA/pF), and series resistance (MΩ) were measured and compensated prior to recording.

Extracellular field potential recordings. Extracellular field potential recordings were performed on coronal slices submerged in aCSF maintained at 33 +/- 1 ^{o}C with a TC-324B Temperature Controller (Warner Instruments, Connecticut, USA) and SH-27B In-Line Solution Heater (Warner Instruments). The aCSF was bubbled continuously with 95 % O_2 / 5 % CO_2 during recordings and recycled until drugs were added. Thin-walled glass capillaries (WPI) were pulled on a Flaming Brown P-87 horizontal micropipette puller (Sutter Instrument Co, California, USA) and used as recording electrodes. Tip resistances where 3.0 +/- 1 MΩ when initially submerged in solution. Signals from the recording electrodes were amplified through a Multiclamp 700A (Molecular Devices) amplifier and digitised through a Digidata 1320A A/D convertor (Molecular Devices) before being visualised on a personal computer running pClamp 8 (Molecular Devices).

Input/Output (I/O) curves were generated by stimulating through a CBARB100 concentric bipolar electrode (FHC Inc., Bowdoin, USA) connected to a DS2A-Mk.II constant voltage isolated stimulator (Digitimer, Welwyn Garden City, UK). I/O were generated first in order to establish the peak amplitude for each recording. A baseline stimulation protocol was used whereby the voltage of the stimulus was increased from 0 V to 80 V every 5 sweeps and the peak amplitude (mV) of the field potential recorded. The baseline stimulation protocol described was an episodic stimulation protocol, with a 1s long sweep every 20 seconds, stimulating at 55 ms for 200 μs at an intensity controlled by the digitimer. After establishment of the peak amplitude, the slice was then recorded for 5 minutes at the maximal amplitude of the field potential on baseline stimulation protocol to determine whether the recording was stable. If the recording was stable and the amplitude of the field potential remained constant, a number of the following recordings were performed as required: a) paired-pulse facilitation recordings; b) theta burst stimulation recordings, and; c) the application of drugs during the 20s baseline stimulation protocol.

The paired-pulse profiles were generated through four episodic stimulation protocols consisting of two stimuli of equal intensity 25 ms, 50 ms, 100 ms and 200 ms apart, respectively. The ratio between the paired-pulses were determined to reveal short term facilitation or depression of the field potentials. A theta burst stimulation protocol was adapted from Calabresi's protocol (Calabresi et al., 1992) , in order to visualise synaptic plasticity. The above protocols were run intrastriatally on both hemispheres, contralaterally and ipsilaterally to the graft/lesion. Following this, graft-host, host-graft and intragraft recordings were also made. Electrode positions are shown in Fig 2.1.

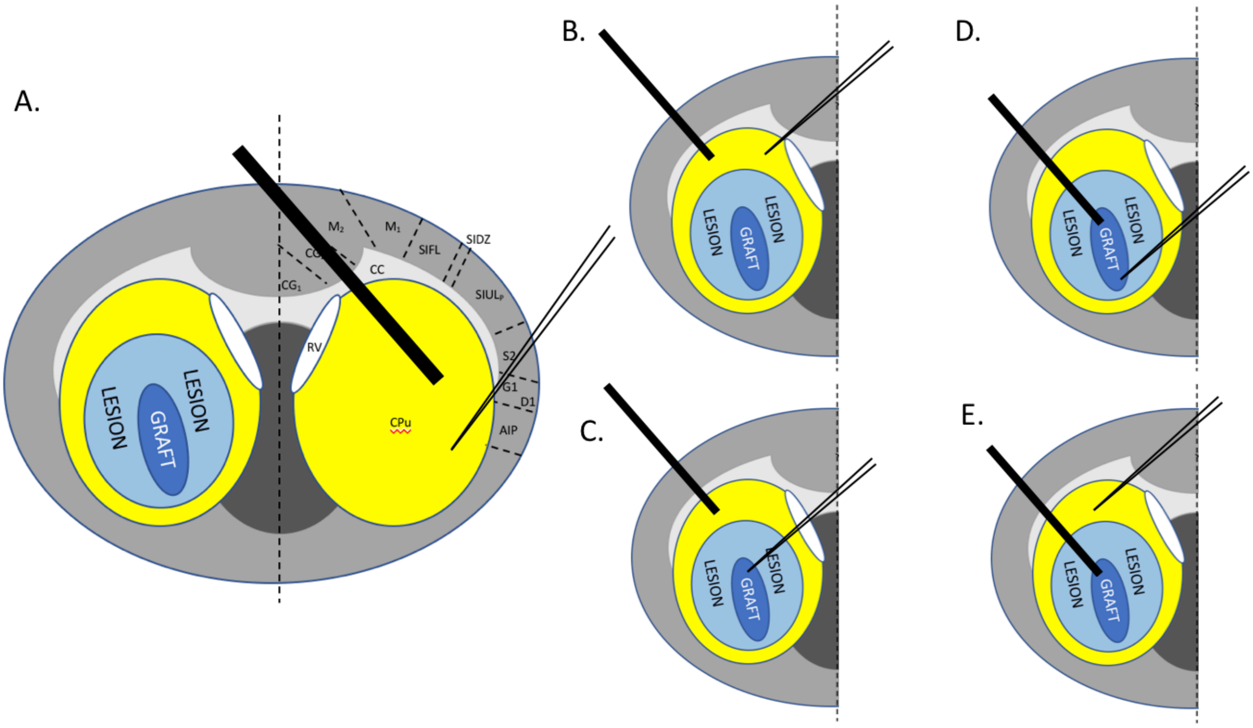

Figure 2.1. Recording and stimulating electrode positions on a coronal slice of the rat brain Coronal slices of the striatum (yellow) are shown above with recording (thin black) and stimulating (solid black) electrode positions shown for the various types of recording.; A. contralateral Intrastriatal; B. ipsilateral Intrastriatal; C. host-graft; D. intragraft and E. graft-host. **Abbreviations: CG1**: cingulate cortex area 1, **CG2**: cingulate cortex area 2, **M2**: secondary motor cortex, **M1**: primary motor cortex, **S1FL**: somatosensory 1 forelimb region, **S1DZ**: somatosensory 1 dysgranular region, **SIULp**: primary somatosensory upper limb, **S2**: second somatosensory cortex, **G1**: granular insular cortex, **D1**: dysgranular insular cortex, **AIP:** agranular insular area, RV: right ventricle, CPu: caudate putamen (striatum).

Multi-electrode array experiments. DIV16 neural progenitor cells (NPCs) were plated at a density of 150 x 10^3 cells/well onto PDL treated, 24-well multielectrode array (MEA) plates with 12 gold electrodes per well on epoxy (Multichannel Systems, Reutlingen, Germany). The plates were loaded onto a Multiwell-MEA Headstage (Multichannel Systems), for signal amplification, interfaced through a MCS-IFB Interface Board (Multichannel Systems). A baseline protocol was performed, absent of any stimulation, sampling at between 5 kHz to measure spontaneous activity. Spike activity was determined as that activity above or below 5 standard deviations of the mean of the noise. Data were then visualised through a connected personal computer running Multiwell Screen and Multi-Channel Suite programmes (Multichannel Systems). Timestamps were exported in .csv format and fed into my custom written MatLab scripts.

2.5 Data Analysis and Graphical Representation

MatLab. All data analyses and graphical representation was performed in MatLab using custom written scrips as described in the relevant chapter of this thesis. Data are shown throughout as mean values ±SEM, and significance considered as $p < 0.05$. n refers to the number of recordings performed.

Chapter 3 – Development of novel MATLAB codes to facilitate the rapid, reliable and reproducible analysis of large complex electrophysiological data sets

3.1 Introduction

MATLAB is a multi-paradigm numerical computing environment developed by MathWorks (Massachusetts, USA), providing a powerful environment for data analysis and complex modelling widely used in academic research (Telezhkin et al., 2016; Penn et al., 2017; Ridler et al., 2018). Increasingly, the data generated by neurophysiologists require extensive data analysis before the data is then interpretable. This places taxing demands on time, whilst dramatically increasing the possibility of human error. Generating code to rapidly and reliably perform analysis of the large and complex datasets means that, not only is the experimental procedure documented and repeatable, the analysis procedure is also. Human error and bias are almost completely removed, and countless hours are saved. However, care must be taken to validate the code used to ensure that the analysis performed is accurate.

3.2 Custom written code

All code is made available digitally through MathWorks/GitHub following completion of this thesis. Included below are exerts of key portions of code.

3.2.1 Automated whole cell patch clamp analysis

Analysis of data generated from whole cell patch clamp analysis is a long process full of opportunities for errors to be made. It was therefore vital to develop a robust, reliable and documented approach to analyse the large complex data sets involved, saving time in the process. To produce a MATLAB script for analysis, statistical testing and graphical representation of whole cell patch clamp recordings multiple smaller scripts that dealt with the individual parameters, as described in Chapter 2, were developed and then packaged into a master script. The output of each of the smaller scripts was then put into a final structure that updated with each iteration of the master script, repeating with each set of recordings (one set = one cell) until a master structure was generated that contained all of the data extracted from all of the cells.

Immediately following an experiment the data is saved as a '.abf' file. It was therefore necessary to import the '.abf' files into the MATLAB workspace. To do this 'abfload.m' was used, available from MATAL Central File Exchange (Hentschke, 2011). Shown in Figure 3.1, the resting membrane potential is extracted as the first ten seconds of recording in a gapfree protocol in current clamp mode (I = 0). Note the output, 'Vm', is assigned to the structure 'output' and field 'output.Vm'.

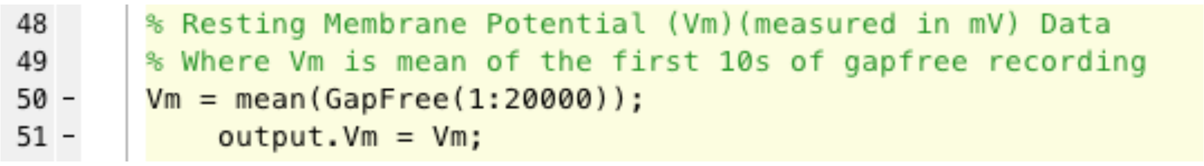

```
% Resting Membrane Potential (Vm)(measured in mV) Data
% Where Vm is mean of the first 10s of gapfree recording
Vm = mean(GapFree(1:20000));
    output.Vm = Vm;
```

Figure 3.1 Resting membrane potential MATLAB script
Resting membrane potential (V_m) was extracted as the mean of the first ten seconds of a gapfree recording in current clamp mode (I = 0) as described in Chapter 2 of this thesis. Not shown, the '.abf' file containing the gapfree recording is imported using 'abfload.m' as 'GapFree' is a separate function equal to 'GapFree = abfload('filename.abf')'.' 1:20000' is the first ten seconds due to the sample rate recordings were made at.

Calculation of resting membrane potential does not require manipulation of the data past a mean calculation. To determine the input resistance of the cells it was necessary to measure the change in membrane potential during a current step protocol. As input resistance is measured in MΩ, the input resistance can be calculated from the voltage change and current values as per Ohm’s Law (see Chapter 1). Figure 3.2 shows the code used to generate the input resistance from the data generated.

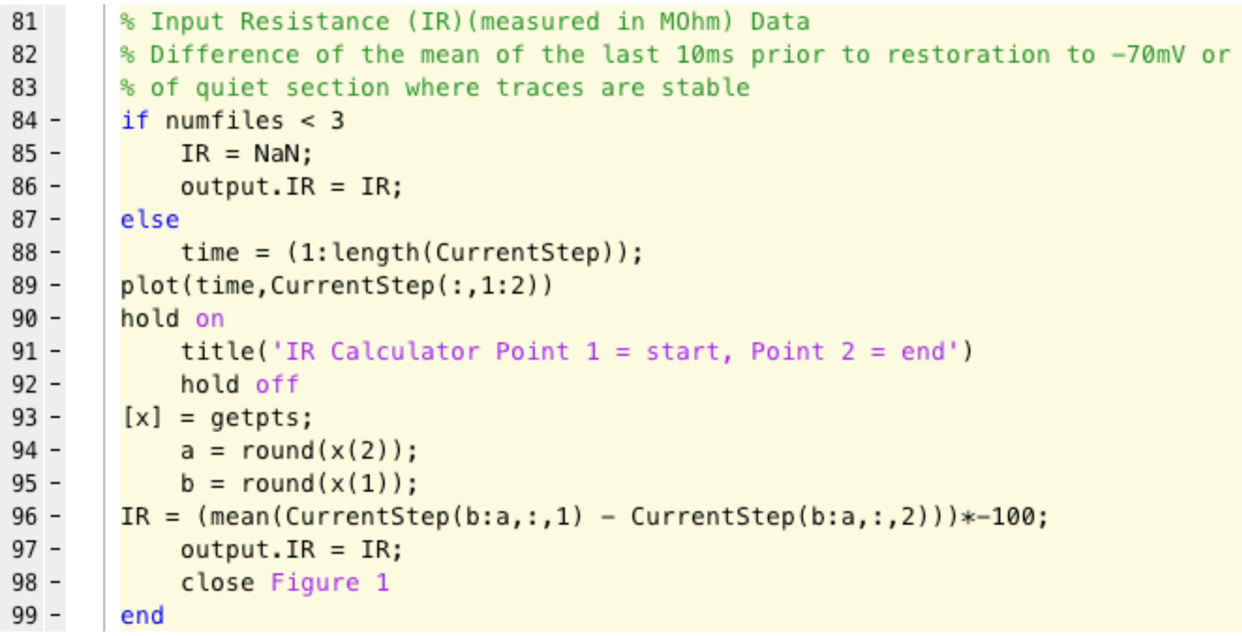

```
81        % Input Resistance (IR)(measured in MOhm) Data
82        % Difference of the mean of the last 10ms prior to restoration to -70mV or
83        % of quiet section where traces are stable
84 -      if numfiles < 3
85 -          IR = NaN;
86 -          output.IR = IR;
87 -      else
88 -          time = (1:length(CurrentStep));
89 -      plot(time,CurrentStep(:,1:2))
90 -      hold on
91 -          title('IR Calculator Point 1 = start, Point 2 = end')
92 -          hold off
93 -      [x] = getpts;
94 -          a = round(x(2));
95 -          b = round(x(1));
96 -      IR = (mean(CurrentStep(b:a,:,1) - CurrentStep(b:a,:,2)))*-100;
97 -          output.IR = IR;
98 -          close Figure 1
99 -      end
```

Figure 3.2: Calculation of input resistance during a current step protocol utilising Ohm’s Law Input resistance (shown above as IR) is calculated from the voltage change following application of current during a current step protocol as per Ohm’s Law. The above script plots the first and second sweep of the current step protocol (line 89), then allows the user to determine a quiet region devoid of activity via the function ‘getpts.m’ (line 93-95). The mean value of these two regions is then subtracted from each-other to determine the voltage difference (line 96). As the current change is 10 pA (as defined in the protocol parameters), multiplication of the voltage difference in mV by -100 allows for calculation of the input resistance in MΩ, in accordance with Ohm’s Law. Not shown, the .abf file containing the current step recording was imported using ‘abfload.m’ as ‘CurrentStep’ (“CurrentStep = abfload(‘filename.abf’);”.

Checkpoints were placed in certain scripts to allow the user to check the data is not corrupted in any way, by excessive noise or an articfact for example. The checkpoint requiring user input here is shown in lines 93 through 95. The function ‘getpts.m’, built in with the software, allows the user to identify a region to calculate the mean membrane potential from. Where possible this region is chosen as the last 10 ms of the current step prior to the membrane potential being clamped to 70 mV, for consistency between analysis. However, if an action potential occurs during this period, the mean membrane potential will be considerably affected, thus ‘getpts.m’ allows users to select a quiet region free from interference of action potentials. The ‘if’ statement in lines 84-86 allow for the rest of the master script to be performed in the absence of the current step recordings. Spike analysis was performed using a similar technique (Fig.3.3).

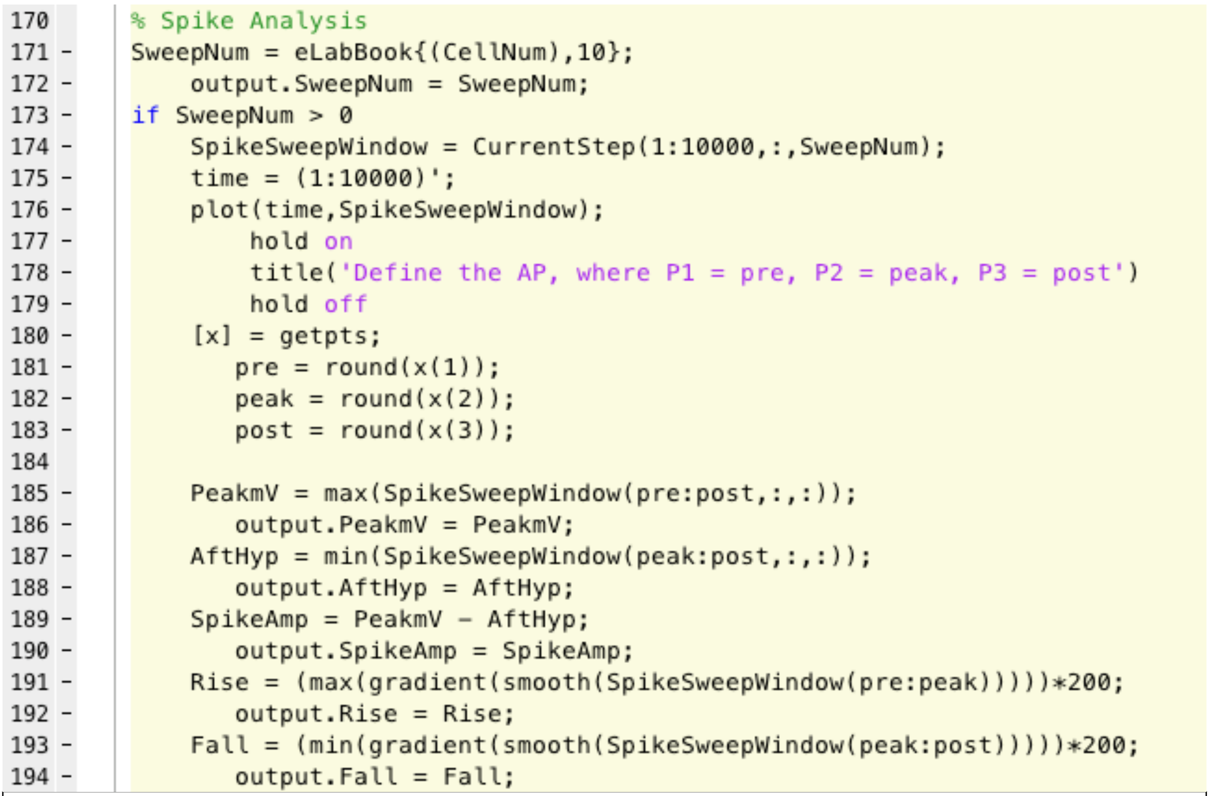

```
170     % Spike Analysis
171 -   SweepNum = eLabBook{(CellNum),10};
172 -       output.SweepNum = SweepNum;
173 -   if SweepNum > 0
174 -       SpikeSweepWindow = CurrentStep(1:10000,:,SweepNum);
175 -       time = (1:10000)';
176 -       plot(time,SpikeSweepWindow);
177 -           hold on
178 -           title('Define the AP, where P1 = pre, P2 = peak, P3 = post')
179 -           hold off
180 -       [x] = getpts;
181 -          pre = round(x(1));
182 -          peak = round(x(2));
183 -          post = round(x(3));
184
185 -       PeakmV = max(SpikeSweepWindow(pre:post,:,:));
186 -          output.PeakmV = PeakmV;
187 -       AftHyp = min(SpikeSweepWindow(peak:post,:,:));
188 -          output.AftHyp = AftHyp;
189 -       SpikeAmp = PeakmV - AftHyp;
190 -          output.SpikeAmp = SpikeAmp;
191 -       Rise = (max(gradient(smooth(SpikeSweepWindow(pre:peak)))))*200;
192 -          output.Rise = Rise;
193 -       Fall = (min(gradient(smooth(SpikeSweepWindow(peak:post)))))*200;
194 -          output.Fall = Fall;
```

Figure 3.3: Spike analysis script
The above script plots the first 10ms of the sweep of interest, defined as ‘SweepNum’, specified in the electronic lab book kept during recordings (line 174). The function ‘getpts.m’ was then used to select three points ‘x1’, ‘x2’ and ‘x3’ at three distinct points of the action potential; pre-threshold (x1), peak amplitude (x2) and post afterhyperpolarisation (x3) (lines 180-183). Peak amplitude (in mV) is taken as the maximum value between ‘x1’ and ‘x3’ (line 185). Afterhyperpolarisation (in mV) is taken as the minimum value between ‘x1’ and ‘x3’. (line 187). Calculated spike amplitude (in mV) is taken as the difference between peak amplitude and the afterhyperpolarisation (line 189). The maximum depolarisation value (in V/s) is taken as the maximum gradient between ‘x1’ and ‘x2’ (line 191) and the maximum repolarisation rate (in V/s) is taken as the minimum gradient between ‘x2’ and ‘x3’ (line 193). Not shown, the ‘.abf’ file containing the current step recording was imported using abfload.m and saved as ‘CurrentStep’ where ‘CurrentStep = abfload(‘filename.abf’)’.

To determine the properties of the individual action potential, the function ‘getpts.m’ was utilised to allow the user to select the action potential of interest. Spike analysis, as described in Chapter 2 of this thesis, was performed on the first action potential following injection of current.

In order to prepare visual representations of the experiments performed, a script was developed that plots exemplary recordings for inclusions in this thesis and future publications. As each sweep of the protocol passes, the trace is likely to shift in the window. It is therefore vital to adjust the traces so that they all start at the same level and are therefore comparable (Fig.3.4).

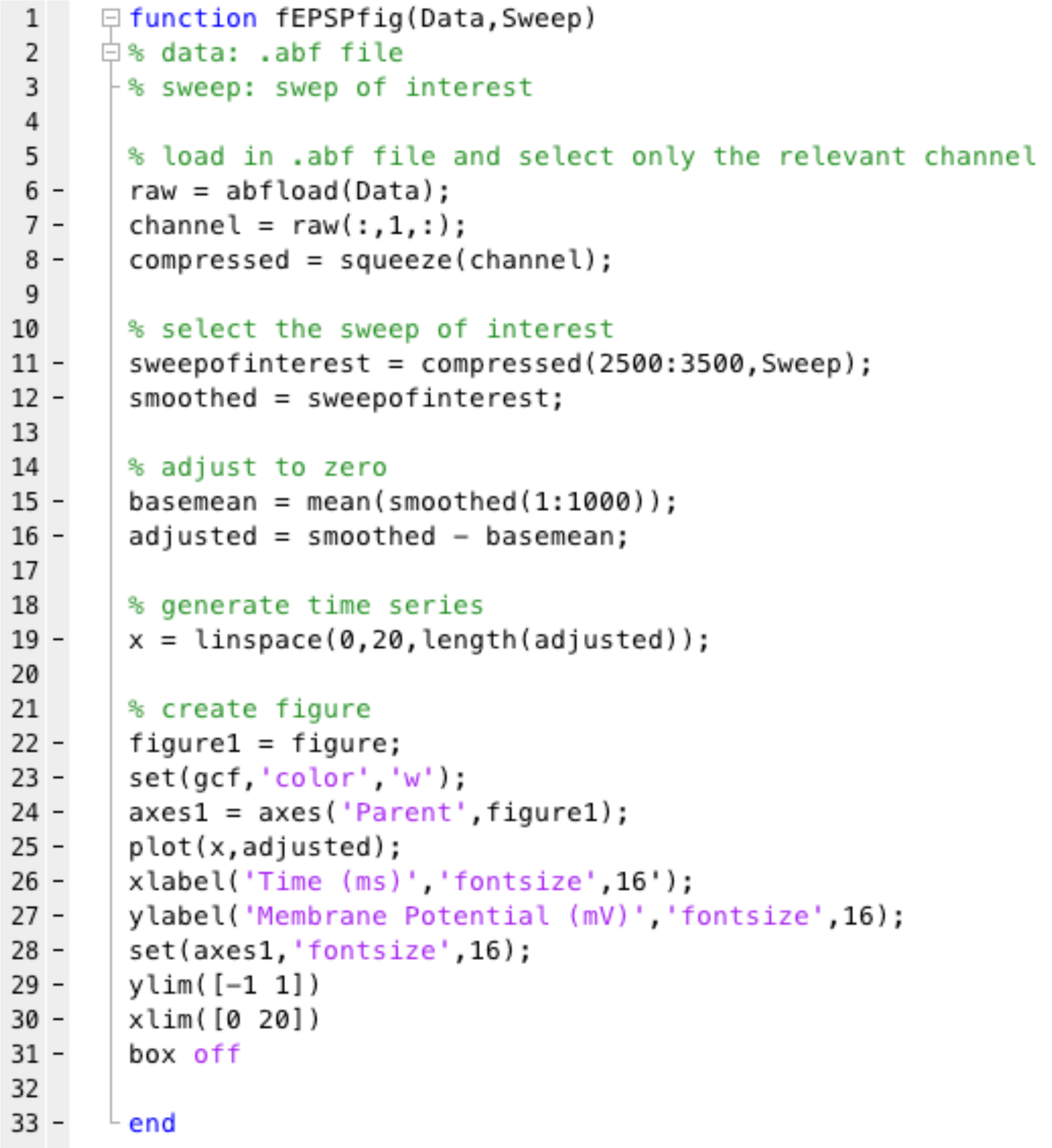

```
 1     function fEPSPfig(Data,Sweep)
 2     % data: .abf file
 3     % sweep: swep of interest
 4
 5     % load in .abf file and select only the relevant channel
 6 -   raw = abfload(Data);
 7 -   channel = raw(:,1,:);
 8 -   compressed = squeeze(channel);
 9
10     % select the sweep of interest
11 -   sweepofinterest = compressed(2500:3500,Sweep);
12 -   smoothed = sweepofinterest;
13
14     % adjust to zero
15 -   basemean = mean(smoothed(1:1000));
16 -   adjusted = smoothed - basemean;
17
18     % generate time series
19 -   x = linspace(0,20,length(adjusted));
20
21     % create figure
22 -   figure1 = figure;
23 -   set(gcf,'color','w');
24 -   axes1 = axes('Parent',figure1);
25 -   plot(x,adjusted);
26 -   xlabel('Time (ms)','fontsize',16');
27 -   ylabel('Membrane Potential (mV)','fontsize',16);
28 -   set(axes1,'fontsize',16);
29 -   ylim([-1 1])
30 -   xlim([0 20])
31 -   box off
32
33 -   end
```

Figure 3.4: Plotting of exemplary recordings
‘abfload.m’ imports the raw data in the ‘.abf’ format into the MATLAB work environment (line 6), where the relevant channel is selected (line 7) and compressed into a vector with two rows (line 8). In lines 10-12 the relevant sweep is selected and then smoothened for plotting. The traces are then adjusted to the mean of the first 1000 data points (lines 14-16). The plot is then formatted to presentation standards in lines 18 to 31.

3.2.2 Automated extracellular field potential recording analysis

In order to analyse extracellular field potential recordings, another semi-automated script was developed. The incorporation of a checkpoint requiring user action, as described earlier, was necessary to ensure the data was not interfered with by afferent fibre volleys or by large artefacts present in the recordings. It was also considerably easier to determine if a recording was actually a field potential (the presence of an afferent fibre volley and subsequent separate 'smooth' field potential) or simply an artefact (sharp and shorter) by eye rather than development of a script for this purpose. Furthermore, field potentials are highly variable responses (smoothness, amplitude, number of peaks, speed etc.) dependant on a large number of factors (age of animal, proximity of recording/stimulating electrode, site of recording in the brain etc.). Figure 3.5 shows a script that generates an input/output curve from the raw .abf file.

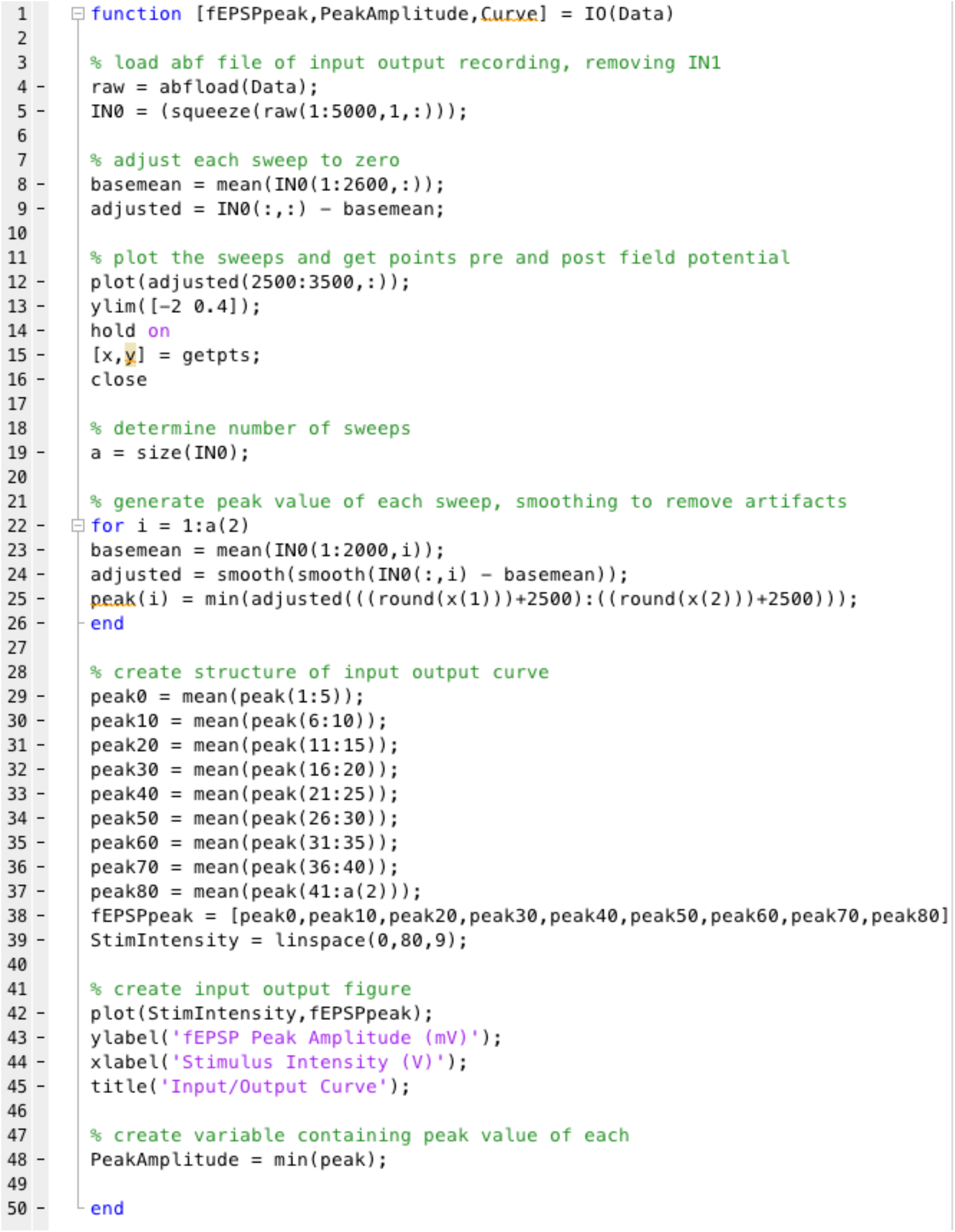

```
 1      function [fEPSPpeak,PeakAmplitude,Curve] = IO(Data)
 2
 3      % load abf file of input output recording, removing IN1
 4 -    raw = abfload(Data);
 5 -    IN0 = (squeeze(raw(1:5000,1,:)));
 6
 7      % adjust each sweep to zero
 8 -    basemean = mean(IN0(1:2600,:));
 9 -    adjusted = IN0(:,:) - basemean;
10
11      % plot the sweeps and get points pre and post field potential
12 -    plot(adjusted(2500:3500,:));
13 -    ylim([-2 0.4]);
14 -    hold on
15 -    [x,y] = getpts;
16 -    close
17
18      % determine number of sweeps
19 -    a = size(IN0);
20
21      % generate peak value of each sweep, smoothing to remove artifacts
22 -    for i = 1:a(2)
23 -    basemean = mean(IN0(1:2000,i));
24 -    adjusted = smooth(smooth(IN0(:,i) - basemean));
25 -    peak(i) = min(adjusted(((round(x(1)))+2500):((round(x(2)))+2500)));
26 -    end
27
28      % create structure of input output curve
29 -    peak0 = mean(peak(1:5));
30 -    peak10 = mean(peak(6:10));
31 -    peak20 = mean(peak(11:15));
32 -    peak30 = mean(peak(16:20));
33 -    peak40 = mean(peak(21:25));
34 -    peak50 = mean(peak(26:30));
35 -    peak60 = mean(peak(31:35));
36 -    peak70 = mean(peak(36:40));
37 -    peak80 = mean(peak(41:a(2)));
38 -    fEPSPpeak = [peak0,peak10,peak20,peak30,peak40,peak50,peak60,peak70,peak80]';
39 -    StimIntensity = linspace(0,80,9);
40
41      % create input output figure
42 -    plot(StimIntensity,fEPSPpeak);
43 -    ylabel('fEPSP Peak Amplitude (mV)');
44 -    xlabel('Stimulus Intensity (V)');
45 -    title('Input/Output Curve');
46
47      % create variable containing peak value of each
48 -    PeakAmplitude = min(peak);
49
50 -    end
```

Figure 3.5: Input/Output Curve Script
'IO.m' (shown here) takes the '.abf' raw data file containing the experimental data for the input out protocol (lines 3-5), as described in Chapter 2, before adjusting all of the baselines to match (lines 7-9) and plotting all of the sweeps on top of one another (line 12). Plotting all of the traces together ensures the region selected by 'getpts.m' (lines 15-16) fully represented the field potentials change over time. The 'for loop' in lines 22-26 extract the peak amplitude (in mV) at each stimulation intensity. Lines 29-39 then generates an array that contains the peak amplitude at each stimulation intensity for plotting in lines 41-45).

3.2.3 Automated multi-electrode array analysis

As the MEAs used in this thesis contain 24 wells, each containing 12 electrodes sampling at 5 kHz – one plate generates 1,440,000 data points per second. This enormous quantity of data requires a high powered environment capable of handling such quantities of data and performing complex analysis quickly. Therefore, a MATLAB script was developed. Much of the script developed for MEA analysis was developed in collaboration with Dr Jon Brown of the University of Exeter Medical School. As the question revolved around synchronicity as a marker of epilepsy, the emphasis of the script was placed on evaluating synchronicity using cross correlation matrices. In order to visualise the data over the course of the experiment, a raster plot was generated by using the 'plotSpikeRaster.m' function (Chiou, 2014). A modified version of 'xcorr.m', available as part of the Deep Learning Toolbox (Mathworks, 2018), was used to plot cross correlation matrices and develop a mean synchronicity index for each well. These were then packaged into a master script along with a script to produce a three dimensional plot of the spike count on each electrode in a well (Fig.3.6).

```
199 	%% 3D Bar Plots
200 
201 
202 -	if D3 == 13
203 -	spikecounts =  [0,(Well(x).channel(1).numSpikes),(Well(x).channel(2).numSpikes),0;...
204 	                (Well(x).channel(3).numSpikes),(Well(x).channel(4).numSpikes),(Well(x).channel(5).numSpikes),(Well(x).channel(6).numSpikes);...
205 	                (Well(x).channel(7).numSpikes),(Well(x).channel(8).numSpikes),(Well(x).channel(9).numSpikes),(Well(x).channel(10).numSpikes);...
206 	                0,(Well(x).channel(11).numSpikes),(Well(x).channel(12).numSpikes),0];
207 
208 -	subplot(2,2,4);
209 -	b = bar3(spikecounts);
210 -	colorbar
211 
212 -	for k = 1:length(b)
213 -	    zdata = b(k).ZData;
214 -	    b(k).CData = zdata;
215 -	    b(k).FaceColor = 'interp';
216 -	end
217 
218 -	ylabel('Y Electrode Coordinate')
219 -	xlabel('X Electrode coordinate')
220 -	zlabel('Spike Count')
221 -	else
222 -	end
```

Figure 3.6: Excerpt of MEA analysis script showing 3D Bar Plot code
Shown here, 'D3' is a marker used to determine whether the master script should carry out the 3D Bar Plot segment of code. Lines 203-206 creates a 4x4 array with the number of spikes from each electrode. Note the corner positions on the array (1,1; 1,4; 4,1; and 4,4;) are marked as zero as there was no electrode in these positions. Lines 208-220 format the plot as a subplot in the master figure (see Chapter 6), assign a colour bar and axis labels.
Abbreviations: MEA: multi electrode array; **3D**: three dimensional.

3.3 Validation of Code

3.3.1 Validation of MATLAB scripts for analysis of whole cell patch clamp experiments

To ensure that the code produced the same results as manual analysis, the developed MATLAB code was run and the manual analysis of the same dataset performed in parallel. The times taken for the MATLAB code to run, and for manual analysis to be performed, were also recorded. No significant differences were seen between manual analysis and MATLAB analysis (Fig.3.7), except in time taken to perform the analysis (11 cells analysis time in MATLAB: 00:04:34, and manually: 00:57:42). These data imply MATLAB analysis is a valid, rapid and reliable tool for the analysis of whole cell patch clamp datasets.

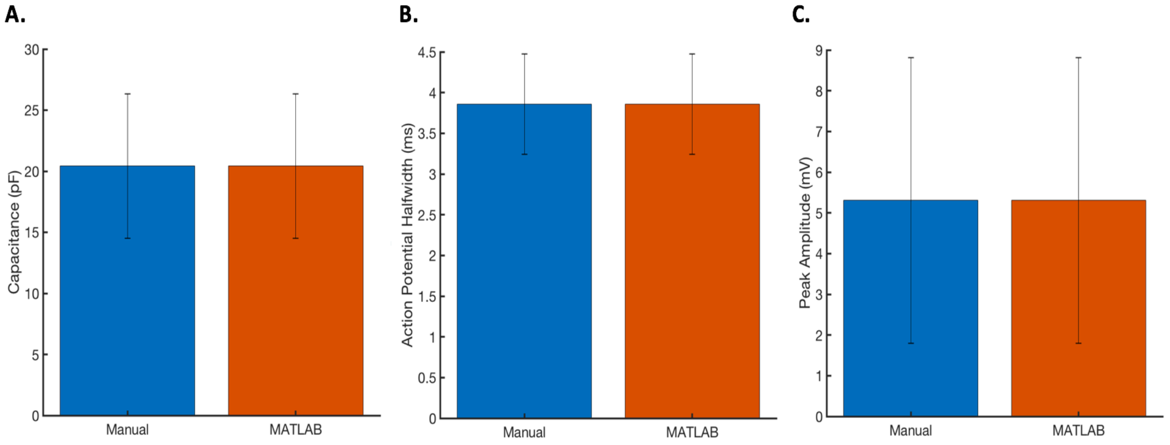

Figure 3.7: Exemplar figures of MATLAB vs Manual analysis of the same dataset of whole cell patch clamp recordings

Shown here are three parameters extracted from whole cell patch clamp recordings upon manual and automated analysis. The only difference seen (not shown) was the time taken to perform the analysis (11 cells analysis time in MATLAB: 00:04:34, and manually: 00:57:42).

A: Manual extraction of capacitance (in pF) (blue) plotted against MATLAB extracted values(orange), taken from the same dataset.

B: Manual extraction of action potential halfwidth (in ms) (blue) plotted against MATLAB extracted values (orange), taken from the same dataset.

C: Manual extraction of action potential amplitude (in mV) (blue) plotted against MATLAB extracted values (orange), taken from the same dataset.

3.3.2 Validation of MATLAB scripts for analysis of extracellular field potential recordings

To validate the use of MATLAB scripts for the analysis of extracellular field potential recordings, the data generated from 18 input/output recording experiments were analysed manually and via MATLAB in parallel, then compared for differences. Shown in Figure 3.8 are two parameters extracted during the analysis of fEPSP recordings; half maximal stimulation intensity (Fig.3.8A) and fEPSP peak amplitude (Fig.3.8B). No significant difference in the result was observed upon testing via a student's t-test, thus suggesting the use of semi-automated MATLAB analysis as a valid method of analysis. Furthermore, MATLAB analysis proved considerably faster (00:01:38) than manual analysis (00:18:06).

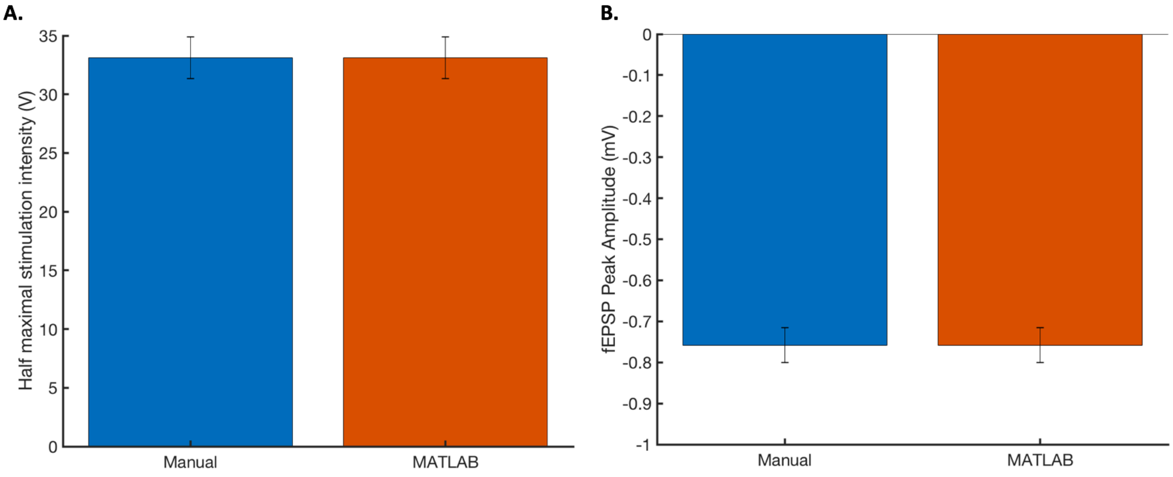

Figure 3.8: Exemplar figures of MATLAB vs Manual analysis of the same dataset of extracellular field potential recordings

Shown are two parameters from extracellular field potential data analysis with MATLAB and performed manually. The only difference seen (not shown) was the time taken to perform the analysis (18 recordings analysis time in MATLAB: 00:01:38, and manually: 00:18:06).

A: Manual extraction of half maximal stimulation intensity (in V) (blue) plotted against MATLAB extracted half maximal stimulation intensity (orange), taken from the same dataset.

B: Manual extraction of fEPSP peak amplitude (in mV) (blue) plotted against MATLAB extracted fEPSP peak amplitude (orange), taken from the same dataset.

Abbreviations: fEPSP : field excitatory post synaptic potential

3.4 Discussion & Conclusion

3.4.1 Accessibility of MatLab

MATLAB has been shown here to be a valid tool for the use of large complex datasets. Not only is the analysis accurate, almost completely devoid of human error and bias, reproducible and documented – it is considerably faster. However, there are three major flaws associated with MATLAB: a) accessibility; b) confounding errors, and; c) code writing, which will be elaborated upon further here. MATLAB, and coding in general, is notoriously considered inaccessible to those who do not have coding experience. Despite MATLAB's user-friendly graphics interface and extensive offline (and included) help section, many users are still intimidated by code and this can present a problem when trying to implement code in a project with multiple collaborators. The second flaw associated with MATLAB is the phenomena of confounding errors. MATLAB will generally not make a mistake unless it is told to make a mistake. MATLAB will rigidly follow the code laid out for it without mistake, therein lies the problem. Codes need to be written by humans and are, therefore, liable to human error. Should any errors written into the code not be noticed, and not cause a fatal error in the code, leading to it's premature termination, then all of the analysis carried out will bear that error and data will be skewed. It is for this reason that all code should be extensively and regularly validated against manual analyses. As shown here, MATLAB was vastly quicker than manual analysis, but the time taken did not account for the time taken to write the code itself. The time taken to write code is dependent on the complexity of the problem, the user's understanding of the problem, and the user's experience of code writing in MATLAB. For example, a novice coder, who is an expert electrophysiologist, will experience similar difficulties as an expert coder who has never seen electrophysiological datasets beforehand.

However, code writing is a non-linear learning process as the user's vocabulary and experience multiply with each other.

3.4.2 Semi-automation analysis allows for check points

As described, MATLAB analysis can vastly increase the speed of the analysis and remove human error. However, any errors in the code will persist and can produce results that do not represent the actual biological phenomena being observed. It is for this reason that the analysis used in this thesis is termed 'semi-automatic' as checkpoints have been placed in the analysis protocol. These checkpoints require user action, although slowing down the analysis, allow the user to ensure that the data at each checkpoint is representative of the biological phenomena being observed. These checkpoints therefore ensure the validity of the data throughout. It was especially important to place checkpoints during the analysis of electrophysiological data as the traces can look profoundly different. Similarly, the MATLAB script could not detect whether the data was corrupted or impacted by a biological/experimental change such as a changing series resistance.

3.4.3 Conclusion

Taking into account the flaws described above, the MATLAB script was validated as a highly efficient tool for the analysis of large complex datasets associated with electrophysiological experiments. Therefore, it's use throughout this thesis for analysis, statistical testing and graphical representation was justified.

Chapter 4 – Establishment of an iPSC derived model of CDKL5-deficiency for high-throughput screening of novel therapeutics

4.1 Introduction

Cyclin dependant kinase like 5 (CDKL5) deficiency is a severe, X-linked condition characterised by early onset epilepsy and mental retardation, closely resembling symptoms seen in Rett syndrome (Scala et al., 2005). Due to the condition's X-linked nature, the majority of the 100 reported cases have been seen in girls, with only 10% seen in boys. The most defining clinical manifestations include: a) normal prenatal history; b) irritability in the perinatal period; c) infantile spasms prior to 5 months; c) Rett like symptoms including, but not limited to: decelerated head growth; reduced voluntary hand movement; sleep disturbances, and; severe mental retardation (Bahi-Buisson and Bienvenu, 2011). These symptoms arise from disruptions in the serine threonine 9 gene (encoding the protein, CDKL5), such as missense, nonsense and frame-shift mutation which result in insufficient levels of the "healthy" protein;– as first described by Kalscheuer *et al.* in 2003 (Kalscheuer et al., 2003). Whilst much of the observed mental retardation is thought to arise from the severe and difficult-to-manage early-onset epilepsy, increased markers of oxidative stress have been seen in patients' peripheral lymphocytes (Pecorelli et al., 2011). This suggests that oxidative stress may also play a role in CDKL5-deficiency pathogenesis.

The precise role of CDKL5 remains elusive despite multiple cell and animal models being developed. Thus far, the cell based models have implicated CDKL5 in neuronal morphogenesis (Chen et al., 2010a) through interactions with PSD-95 (Zhu et al., 2013), a post-synaptic scaffold protein. Furthermore, the phosphorylation and degradation of CDKL5 itself appears to be regulated by neuronal activity (Montanara et al., 2015). Two animal models have been established (Wang et al., 2012; Amendola et al., 2014) which both exhibit characteristics similar to that seen in patients, and which implicate the AKT/GSK-3β pathways despite normal protein levels (Wang et al., 2012). Decreased phosphorylation of AKT and mTOR were observed, and were completely restored upon restoration of CDKL5 expression (Fuchs et al., 2014). This observation was also true for survival of immature neurons, the apoptosis of which were greatly increased in the absence of CDKL5. Thus, CDKL5 appears to play key roles in both neurite outgrowth, neuronal survival and cell signalling. CDKL5 has also been implicated in histone modifications, specifically through phosphorylation of histone deacetylase 4 (HDAC4), resulting in decreased HDAC4 nuclear localisation and neuronal survival (Trazzi et al., 2016). Both were restored through GSK-3β and HDAC4 inhibition with SB216763 and LMK235, respectively (Fuchs et al., 2015; Trazzi et al., 2016). Intriguingly, hippocampal dependant memory tests performed in these animals following SB21673/LMK235 treatment resulted in significant improvements bringing the animals close to that of wild type mice (Fuchs et al., 2015; Trazzi et al., 2016).

Despite promising studies, the precise role of CDKL5 remains elusive. Furthermore, the CDKL5-deficient mice (Wang et al., 2012; Amendola et al., 2014) did not display early onset epileptic phenotypes – the single most apparent characteristic seen in humans. This epilepsy is life-limiting and difficult to manage. Steroids are the recommended treatment for the initial infantile spasms (Pellock et al., 2010) and a variety of anti-epileptic drugs are added in combination dietary modification as the patients develop more severe seizures (Bahi-Buisson and Bienvenu, 2011). However, treatments are often not completely effective or patients with good early prognosis following treatment, patients often develop resistance to their prescribed treatment over time. Therefore, it is vital to generate a high throughput screening model of altered excitability.

4.2 Aims and rationale

The precise neurophysiological impact of a mutation in *CDKL5* is not known, and it is hoped that detailed characterisation of these properties will shed light on the causes of the life-limiting epilepsy seen in CDKL5-deficiency patients. The use of patient-derived iPSC generated neurons should complement the previously conducted animal research whilst also hopefully recreating the epilepsy seen in patients. Should this epilepsy be visible in the iPSC derived cultures, a high throughput screening method would need to be established to facilitate testing of novel therapeutic compounds. Therefore, this project aims to characterise functionally CDKL5-deficiency patient-derived iPSCs as they differentiate into cortical neurons in order to develop a reliable platform for the rapid screening of future novel therapeutics.

4.3 Methods

iPSCs were isolated from a female patient with the c.1375C>T (CAG>TAG) p.Q459X mutation. Due to the X-linked nature of CDKL5-deficiency, females carrying the mutation have one mutated copy and one wild type copy. Which copy is activated occurs at random in each cell.. Once the fibroblasts were converted to iPSCs by Dr David Millar at the Institute of Medical Genetics, Cardiff University, the cells were genotyped and isolated into colonies dependant on expression of either the mutant or wild-type CDKL5. Cells were then differentiated into neural progenitor cells and plated using the Synaptojuice protocol (Telezhkin et al., 2016), described in Chapter 2 of this thesis, on glass coverslips and multi-electrode arrays. The data shown here were generated over three plate-downs by Dr Christian Schnell (two plate-downs) and myself (one plate-down). Data generated by Dr Schnell are included only with his express permission. Data were then fed into my custom written MatLab script for analysis, statistical tests and graphical representation as described in Chapter 3 of this thesis. The MEA analysis script was written in collaboration with Dr Jonathon Brown of the University of Exeter Medical School and used within this project with his permission.

Data are represented as mean values ±SEM, where appropriate. One-way and two-way ANOVA's with *post-hoc* Bonferroni corrected t-tests, Tukey's test and students t-test, as appropriate.

4.4 Results

4.4.1 iPSC derived neurons harbouring wild type and mutated CDKL5 mature at a similar rate using the Synaptojuice protocol

To determine whether the c.1375C>T p.Q459X mutation affected the rate and extent of neuronal maturation, iPSC-derived neural progenitors were generated from an affected patient. The colonies were then isolated, plated on glass coverslips and matured using the Synaptojuice protocol (Telezhkin et al., 2016). Whole-cell patch-clamp experiments were then performed at DIV7, DIV14 and DIV21 to chart their maturation. Firstly, passive membrane properties were observed (Figure 4.1). Resting membrane potential was measured in current clamp mode (I = 0).

A two way ANOVA was conducted to determine whether the differences observed were due to age (DIV) or group (mutant or wild-type). Here, the ANOVA $p < 0.01$. Mean resting membrane potential in the mutant CDKL5 line was significantly more negative at DIV21 (-51.78 +/- 3.25 mV) than at DIV7 (-38.31 +/- 2.54 mV, $p < 0.005$, Figure 4.1A). Whilst no significant differences were seen in the wild type line, a similar trend was observed with DIV21 being more negative than DIV7. Capacitance, a measure of cellular size and complexity, and input resistance, a marker of the number of open ion channels present, were then measured during a voltage-step protocol. The mutant line had a smaller mean capacitance (16.09 +/- 0.96 pF) than the wild type line (19.38 +/- 0.14 pF) at DIV14 ($p < 0.05$, Figure 4.1B). No other significant differences were observed, although the capacitance does appear to increase over the time-course of the experiments. No significant differences in input resistance were observed between wild type and mutant neurons over 21 days post plating (Figure 4.1C).

Thus, as there are very few significant differences between the passive properties, these data suggest that the c.1375C>T p.Q459X mutation in CDKL5 does not appear to have a large influence on the rate and extent of neuronal maturation as assessed by basic, passive membrane properties.

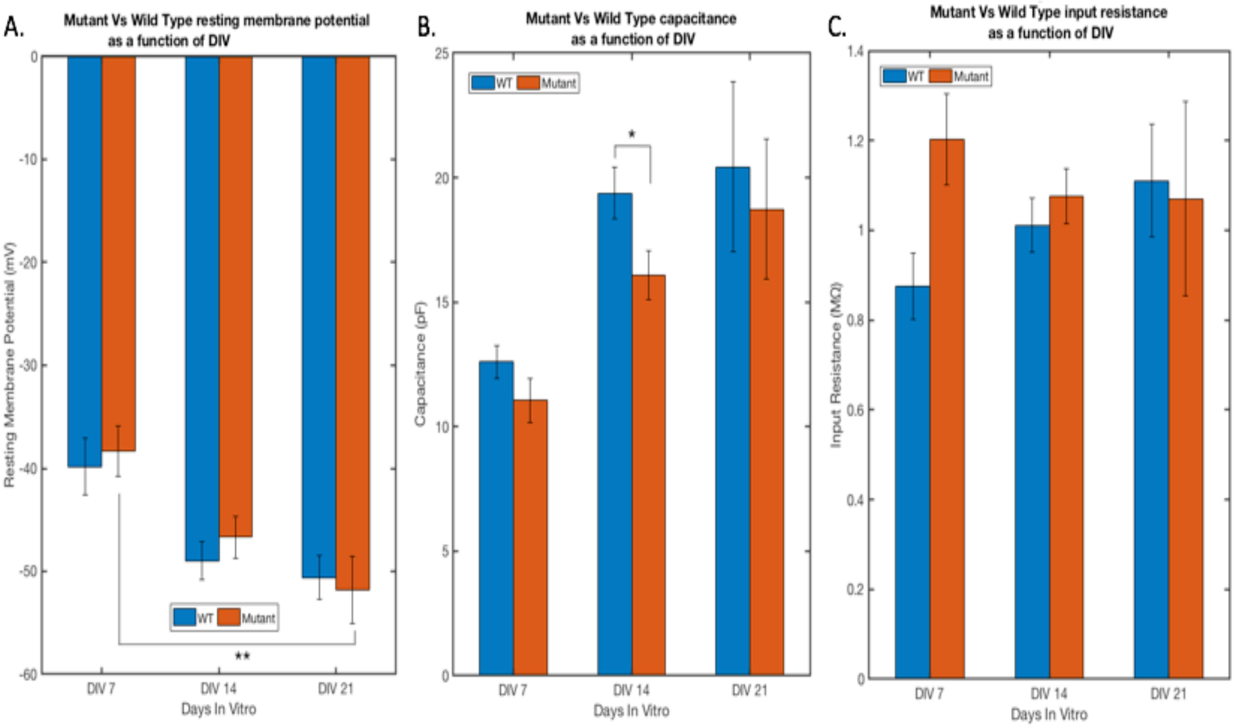

Figure 4.1: Passive membrane properties of CDKL5 iPS derived cortical neurons mature over three weeks in Synaptojuice

A-C: Bar charts plotting resting membrane potential (A), capacitance (B) and input resistance respectively of iPS derived neurons harboring both wild type CDKL5 (blue bars) and the c.1375C>T p.Q459X mutant CDKL5 (orange bars) matured over a course of 21 days post plating in line with the Synaptojuice protocol. Neurons underwent whole cell patch clamp experiments at DIV7, DIV14 and DIV21 to generate the data shown.

Data shown here as mean +/- SEM. p* <0.05, p** <0.01

Abbreviations: CDKL5: cyclin dependent kinase like five, **WT**: wild type, **DIV**: days in vitro, **iPS**: induced pluripotent stem cells

To determine whether the CDKL5 maturation affected active electrical properties, the ability of the neurons to generate spontaneous and induced activity was interrogated in whole-cell patch-clamp experiments. Spontaneous activity was observed in current-clamp mode (I = 0) and then classified as either quiet, attempting or spontaneous (as described in Chapter 2). Spontaneous activity was observed in both wild type (Figure 4.2A-C) and mutant (Figure 4.2D-E) CDKL5 lines at all stages of maturation. The number of wild type neurons exhibiting spontaneous activity also increased from 7 % at DIV7, 38 % at DIV14, to 45 % at DIV21 (Figure 4.2A-C). A similar trend was observed in the mutant CDKL5 neurons from 23 % of cells exhibiting spontaneous activity at DIV7, 67 % at DIV14 to 71% at DIV21 (Figure 4.2D-E). These data suggest that neurons with either variant of CDKL5 are able to generate spontaneous activity at their resting potentials and that this activity increases over time as the neurons mature. Neurons expressing the mutant CDKL5 appear to have a greater propensity for spontaneous activity at all stages of maturation. Inspection of the exemplar traces, such as those in Figure 2F, suggest that there are commonly more bursts of spontaneous activity in wild type than in mutant neurons (Figure 4.2C).

The levels of electrical activity were observed during a current-step protocol (holding the Vm close to -70 mV, as described in Chapter 2) and then classified as either quiet, incomplete activation, single, single attempting train or train activity (also described in Chapter 2). Induced trains of action potentials were observed in both wild type (Figure 4.3A-C) and mutant (Figure 3.3D-E) lines at all stages of maturation. The number of wild type CDKL5 cells exhibiting trains of activity also increased from 23 % at DIV7, 29 % at DIV14, to 47 % at DIV21 (Figure 3.3A-C). A similar trend was observed in the mutant CDKL5 from 7 % of cells exhibiting trains of activity at DIV7, 28 % at DIV14 to 47% at DIV21 (Figure 4.3D-E). These data suggest that neurons with either variant of CDKL5 are able to generate trains of induced action potentials that increase over time as the cells mature. Taken together these data suggest that the presence of the c.1375C>T p.Q459X mutation in the CDKL5 protein does not significantly affect the ability of neurons to generate spontaneous or induced action potential generation, nor does it significantly impair the rate of maturation of these properties.

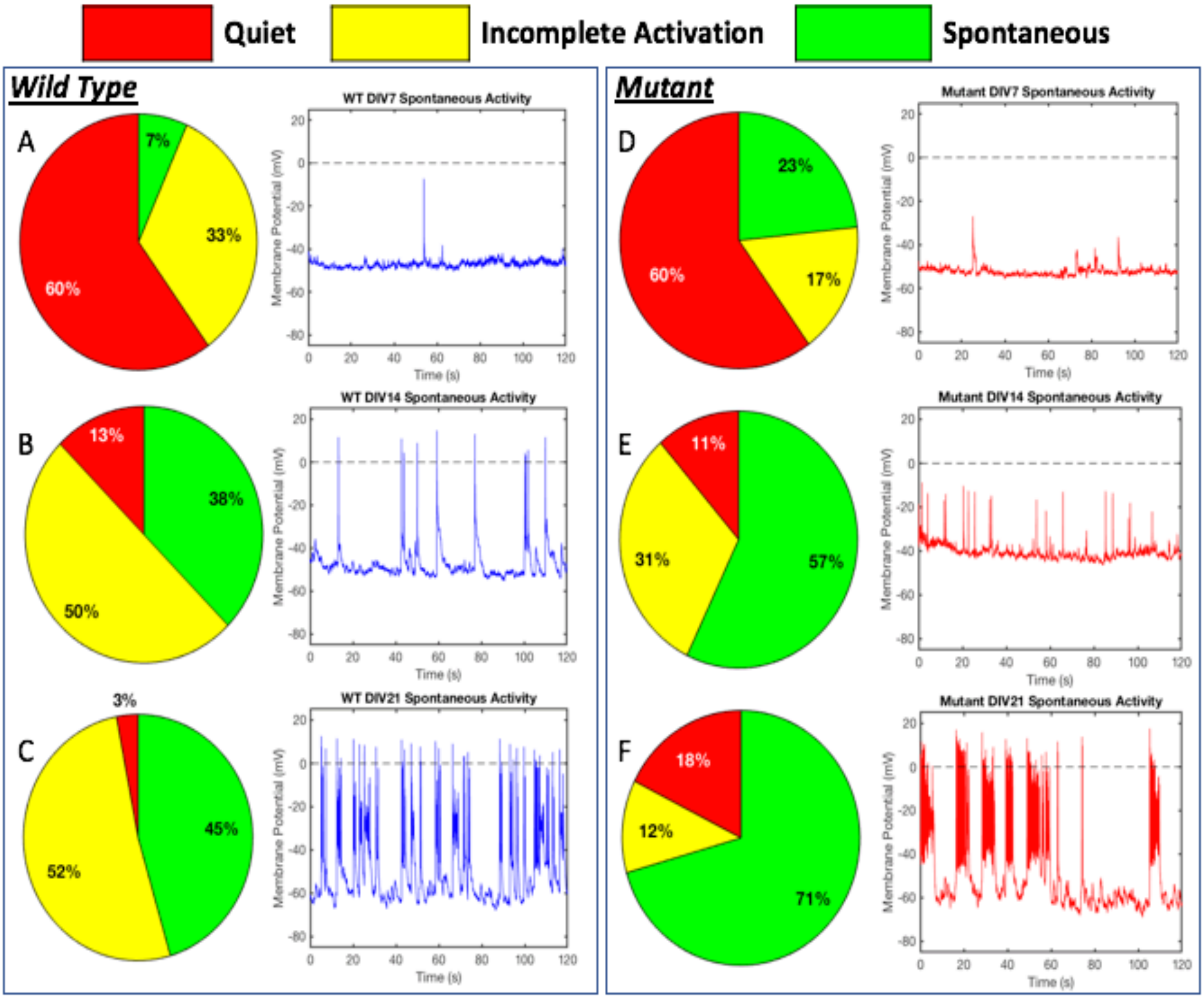

Figure 4.2: Spontaneous activity levels of CDKL5 iPS derived cortical neurons mature over three weeks in Synaptojuice
Pie charts, accompanied by exemplary recordings, showing the levels of spontaneous activity measured from iPS derived neurons harboring the wild type CDKL5 and the c.1375C>T p.Q459X mutant CDKL5 during whole cell patch clamp experiments, during maturation in line with the Synaptojuice protocol. Experiments were performed at DIV7, DIV14 and DIV21 to chart the maturation of the cells. The red segments in the pie charts represent quiet cells devoid of action potentials, the yellow represents incomplete activation of action potentials and the green represent spontaneous activity where action potentials result in complete depolarisation of the neurons crossing 0 mV.
A-C: pie charts and exemplary recordings of wild type CDKL5 neurons at DIV7, DIV14 and DIV21 respectively.
D-F: pie charts and exemplary recordings of mutant CDKL5 neurons at DIV7, DIV14 and DIV21 respectively.
Abbreviations: CDKL5: cyclin dependent kinase like five, **WT**: wild type, **DIV**: days in vitro, **iPS**: induced pluripotent stem cells

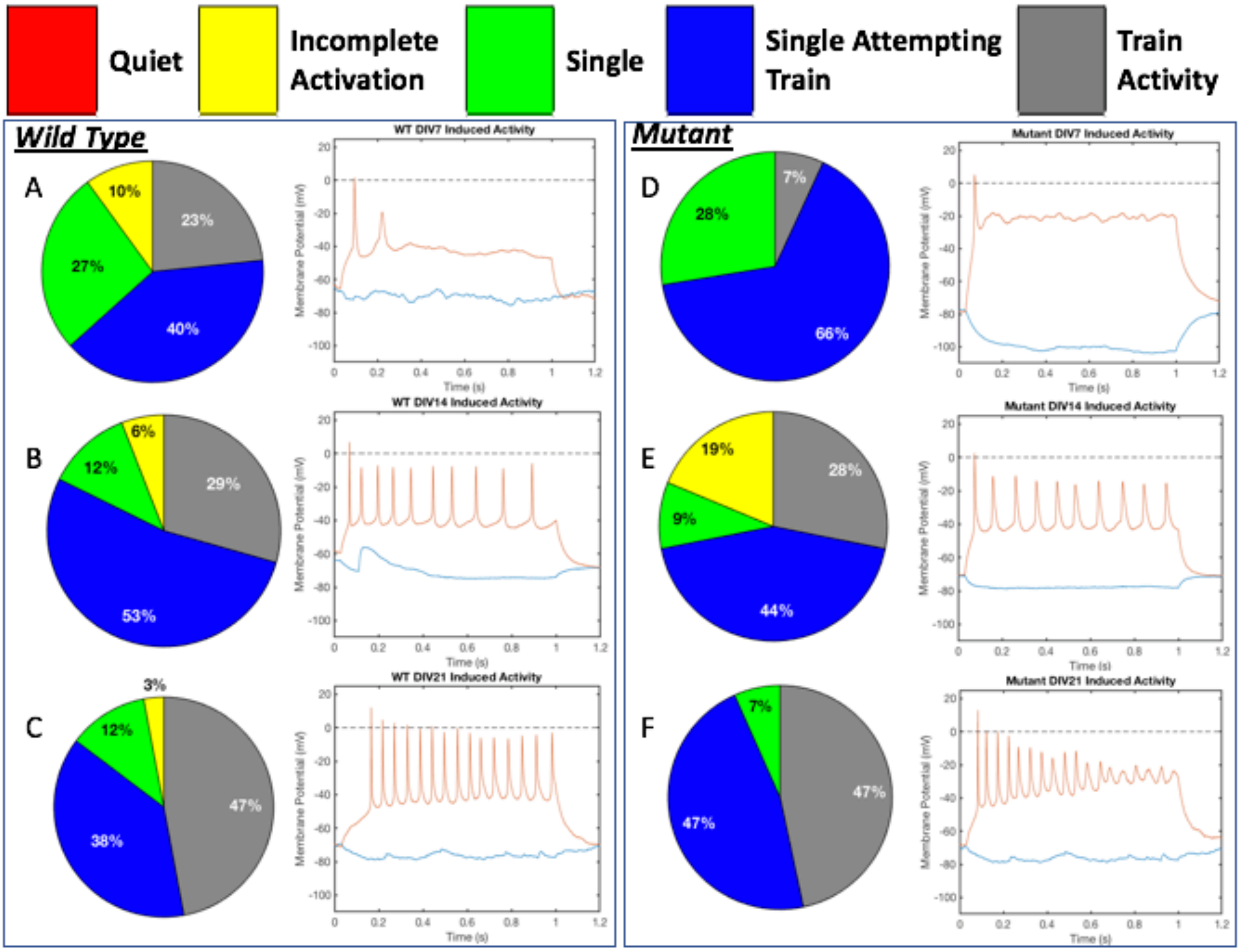

Figure 4.3: Induced activity levels of CDKL5 iPS derived cortical neurons mature over three weeks in Synaptojuice

Pie charts, accompanied by exemplary recordings, showing the levels of induced activity measured from iPS derived neurons harboring the wild type CDKL5 and the c.1375C>T p.Q459X mutant CDKL5 during whole cell patch clamp experiments, during maturation in line with the Synaptojuice protocol. Experiments were performed at DIV7, DIV14 and DIV21 to chart the maturation of the cells. The pie charts depict the proportions of cells exhibiting quiet and devoid of action potentials (red), incomplete activation of action potentials (yellow), a single action potential that results in complete depolarisation of the neuron (green), attempting train activity (blue) and trains of induced activity (grey). All exepmplary recordings show the membrane potential in response to -10 pA (light blue) and +40 pA (orange).

A-C: pie charts and exemplary recordings of wild type CDKL5 neurons at DIV7, DIV14 and DIV21 respectively.

D-F: pie charts and exemplary recordings of mutant CDKL5 neurons at DIV7, DIV14 and DIV21 respectively.

Abbreviations: CDKL5: cyclin dependent kinase like five, **WT**: wild type, **DIV**: days in vitro, **iPS**: induced pluripotent stem cells

Next, to determine whether the mutant CDKL5 impacted the properties of the induced action potentials, the first complete action potential to result from injection of current from each induced activity protocol were examined more closely using my automated spike analysis code in MatLab. The mutant CDKL5 line action potential halfwidths at DIV21 (2.986 +/- 0.09 ms) were significantly smaller than those of the wild type CDKL5 line (3.86 +/- 0.31 ms, $p < 0.05$, Figure 4.4A). A general trend towards a smaller halfwidth and, therefore, a more mature neuronal phenotype, was also observed between DIV7 and DIV21 in both wild type and mutant CDKL5 lines.. The action potential amplitude of mutant CDKL5 neurons (44.96 +/- 2.93 mV) at DIV14 is significantly lower than the amplitude of action potentials observed in wild type neurons (52.17 +/- 2.07 mV, $p < 0.05$, Figure 4.4B). However, this is reversed by DIV21, with the mutant CDKL5 action potential amplitude being significantly higher (62.02 +/- 4.69 mV) than observed in wild type neurons (50.5 +/- 2.61 mV, $p < 0.05$, Figure 4.4B). Once again, a statistically insignificant trend toward more mature, more positive, action amplitudes as the DIV pass is observed. The action potential depolarisation rates did not significantly change for both the wild type and mutant CDKL5 lines between DIV7 and DIV14. At DIV21 the wild type CDKL5 action potential depolarisation rate was at a level consistent with DIV7 and DIV14 (43.69 +/- 3.61 V/s). However, the depolarisation rate in mutant CDKL5 cells was significantly faster (68.05 +/- 8.2 V/s, $p < 0.01$, Figure 4.4C). The only significant difference in action potential threshold potential was seen at DIV7 (Figure 4.4C); a threshold value of 37.87 +/- 1.3 mV in wild type CDKL5 cells compared to 31.54 +/- 1.18 mV in mutant CDKL5 cells ($p < 0.01$). The action potential repolarisation rate at DIV7 was lower and, therefore, slower in mutant CDKL5 cells (-17.35 +/- 1.27 V/s) than in wild type CDKL5 cells (-21.25 +/- 12.8 V/s, $p < 0.05$, Figure 4.4E). The action potential afterhyperpolarisation value was significantly lower at DIV7 in mutant CDKL5 (-33.16 +/- 1.92 mV) than in the wild type cells (-38.49 +/- 2.09 mV, p < 0.05, Figure 4.4F). Taken together these data suggest that the c.1375C>T p.Q459X mutant CDKL5 has a small effect on action potential properties; although largely they are comparable to their wild type counterparts and mature at a similar rate.

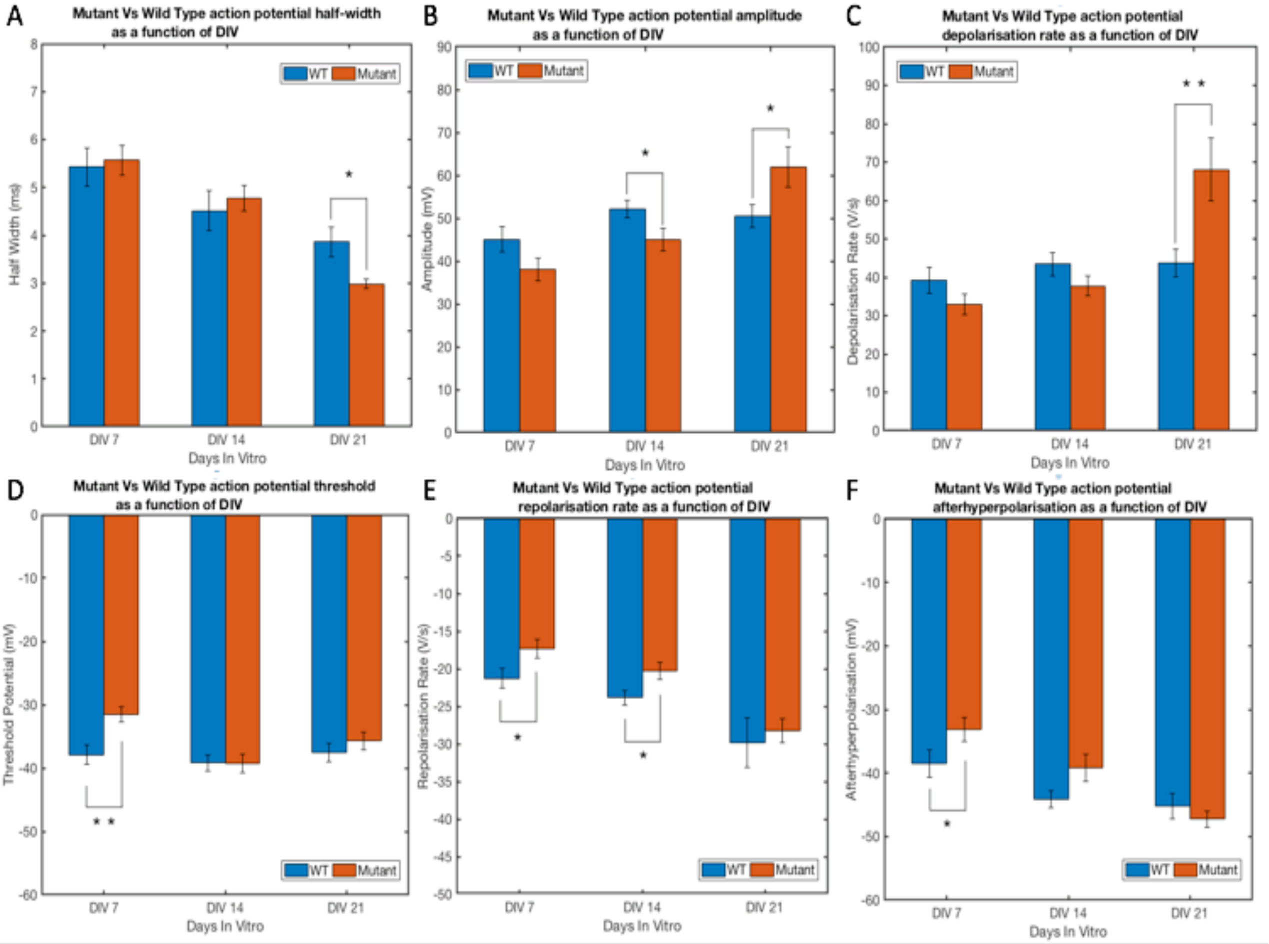

Figure 4.4: Action potential properties of CDKL5 iPS derived cortical neurons mature over three weeks in Synaptojuice

A-F: Bar charts plotting resting action potential half-width (A), amplitude (B), depolarization rate (C), threshold potential (D), repolarization rate (E) and afterhyperpolarisation (F) of iPS derived neurons harboring both wild type CDKL5 (blue bars) and the c.1375C>T p.Q459X mutant CDKL5 (orange bars) matured over a course of 21 days post plating in line with the Synaptojuice protocol. Neurons underwent whole cell patch clamp experiments at DIV7, DIV14 and DIV21 to generate the data shown.

Data shown here as mean +/- SEM. p* <0.05, p** <0.01

Abbreviations: CDKL5: cyclin dependent kinase like five, **WT**: wild type, **DIV**: days in vitro, **iPS**: induced pluripotent stem cells

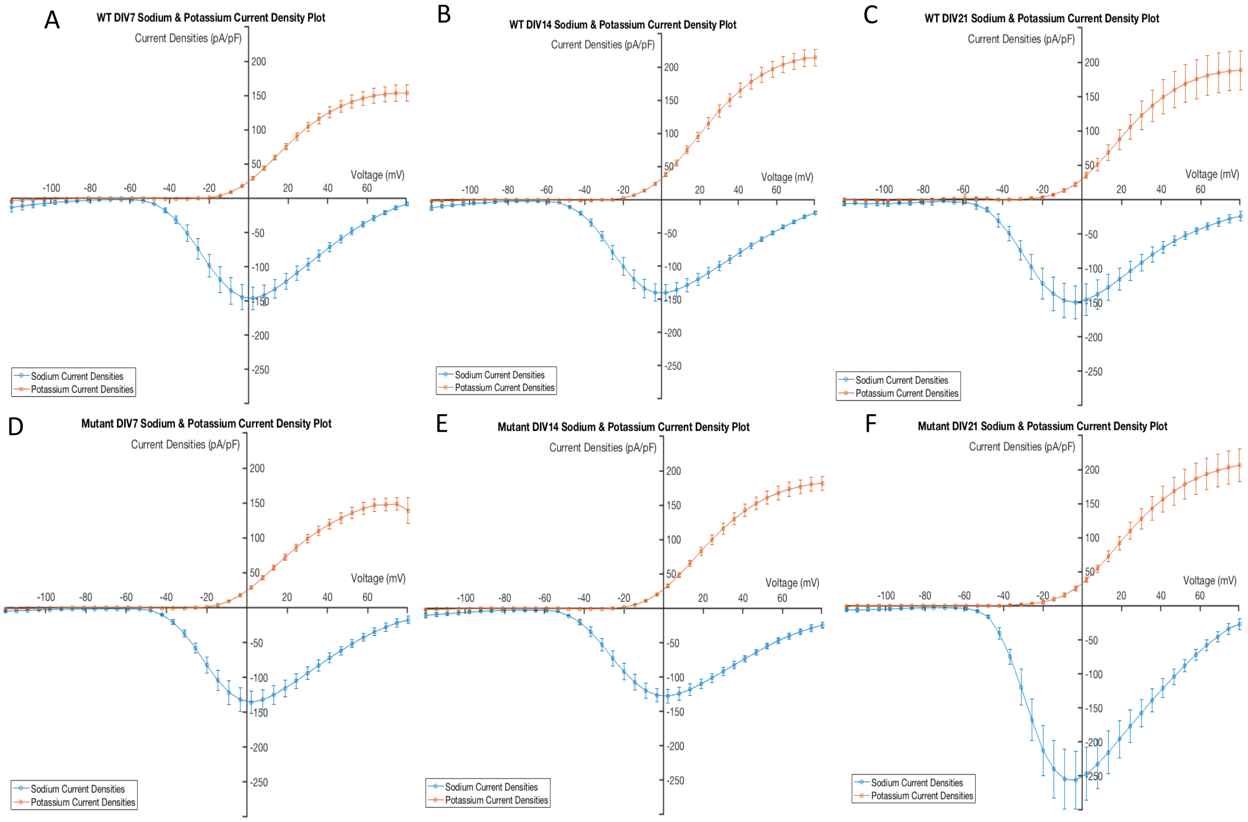

WT DIV7 Sodium & Potassium Current Density Plot

WT DIV14 Sodium & Potassium Current Density Plot

WT DIV21 Sodium & Potassium Current Density Plot

Mutant DIV7 Sodium & Potassium Current Density Plot

Mutant DIV14 Sodium & Potassium Current Density Plot

Mutant DIV21 Sodium & Potassium Current Density Plot

Figure 4.5. Maturation of sodium and potassium current densities in CDKL5 iPS derived neurons over three weeks in Synaptojuice

Mean sodium and potassium current density plots obtained during whole cell patch clamp experiments.

A-C: mean current density against voltage plots derived for maximum voltage-activated Na$^+$ (blue) and K$^+$ currents (orange) taken from iPS derived cortical neurons harbouring the wild type CDKL5 during maturation in line with the Synaptojuice protocol at DIV7, DIV14 and DIV21 respectively.

D-F: mean current density against voltage plots derived for maximum voltage-activated Na$^+$ (blue) and K$^+$ currents (orange) taken from iPS derived cortical neurons harbouring the c.1375C>T p.Q459X mutant CDKL5 during maturation in line with the Synaptojuice protocol at DIV7, DIV14 and DIV21 respectively.

Data shown here as mean +/- SEM.

Abbreviations: CDKL5: cyclin dependent kinase like five, **WT**: wild type, **DIV**: days in vitro, **iPS**: induced pluripotent stem cells

Lastly, the maturation profiles of voltage-activated sodium and potassium currents were investigated using a voltage-step protocol in whole cell patch-clamp experiments, as described in Chapter 2, at DIV7, DIV14 and DIV21. Pairing the sodium and potassium currents (pA) with the capacitance data generated earlier (pF) allowed calculation of their respective current densities (pA/pF). Surprisingly, potassium current densities did not appear to be change significantly during the course of maturation in both mutant and wild type CDKL5 cells (Figure 4.5). However, there was a striking differences in the maximum sodium current density of the mutant CDKL5 neurons at DIV21 which was above 250 pA/pF, compared to all other sodium current densities which were essentially less than to 150 pA/pF (Figure 4.5F). It is noted that the sodium curves never reach the reveral potential for sodium. The expected reversal potentials, upon extrapolation of the line appear more positive than the sodium

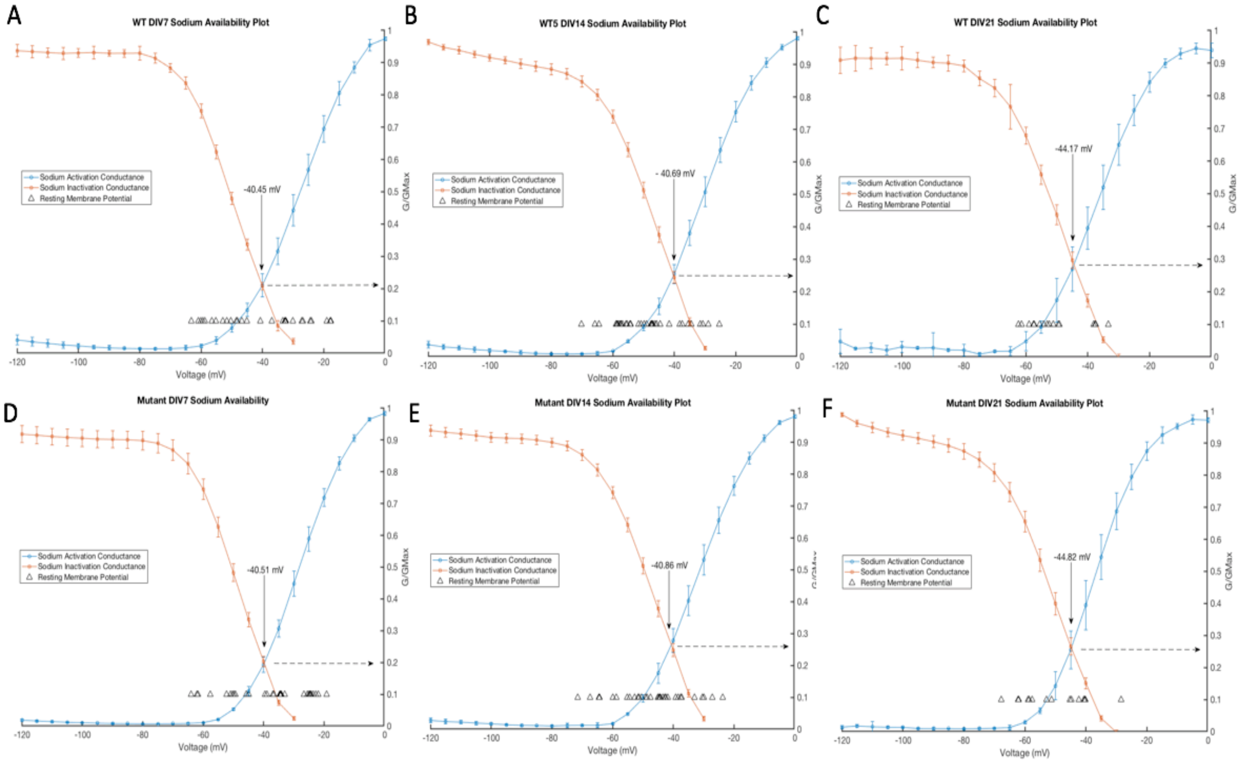

Figure 4.6. Maturation of sodium availability in CDKL5 iPS derived neurons over three weeks in Synaptojuice

Mean mean fractional conductance (*G*/*G*max) plots for voltage activation (blue) and inactivation (orange) of sodium currents obtained during whole cell patch clamp experiments of iPS derived neurons harbouring the wild type CDKL5 and the c.1375C>T p.Q459X mutant CDKL5 during maturation in Synaptojuice over 21 days post plating. Peak *G*/*G*max is indicated by the arrow. Individual *V*m values are plotted on each graph by the white triangles.

A-C: mean sodium availability plots of iPS derived neurons harbouring the wild type CDKL5 recorded at DIV7, DIV14 and DIV21 respectively.

D-E: mean sodium availability plots of iPS derived neurons harbouring the c.1375C>T p.Q459X mutant CDKL5 recorded at DIV7, DIV14 and DIV21 respectively.

Data shown here as mean +/- SEM.

Abbreviations: CDKL5: cyclin dependent kinase like five, **WT**: wild type, **DIV**: days in vitro, **iPS**: induced pluripotent stem cells

reversal potential. This is perhaps caused by calcium influx during the recording, which has a considerably more positive reversal potential. The sodium and potassium currents were recorded in the same protocol as part of a larger set of protocols whereby it was not practicially possible to pharmacologically isolate the sodium and potassium currents.

The activation/inactivation profiles of the voltage-activated sodium currents were next examined. The sodium availability window was slightly larger at DIV21 than earlier in the maturation for both wild type and mutant CDKL5 neurons with fractionally higher G/Gmax values, and a higher proportion of neurons with a resting membrane potential falling within these windows, than those for DIV7 and DIV14 (Figure 4.6).

Taken together, these data demonstrate that there are very few striking differences in the basic neuronal properties between wild type CDKL5 neurons and mutant CDKL5 neurons suggesting that the c.1375C>T p.Q459X mutation in CDKL5 has little impact on the rate and extent of maturation profiles of these neurons. This suggest that there are little differences between the two neuronal populations or that a component of the Synaptojuice might be masking the difference.

3.4.2 Removal of BDNF, CHIR99021 and LM22A4 from Synaptojuice medium appears to have little effect on basic functional properties of iPSC derived neurons harbouring wild type and mutated CDKL5

Disrupted GSK3β is thought to be central to CDKL5 pathogenesis (Fuchs et al., 2014 p.3, 2015 p.3, 2018 p.3). As Synaptojuice contains small molecules known to interact with components of the GSK3β signalling pathway, it was suggested that these might be masking the disease phenotype in mutant CDKL5 cells. To determine whether such small molecules in Synaptojuice were indeed masking the disease phenotype, the BDNF, CHIR99021 and LM22A4 were removed from the Synaptojuice medium for half of the cells during the final

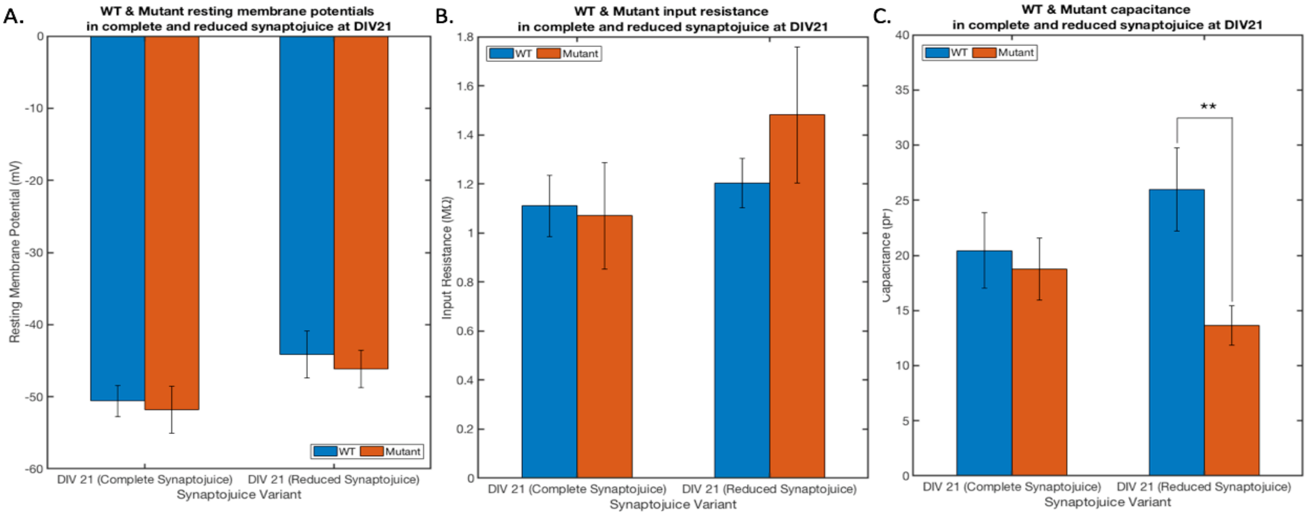

Figure 4.7: Passive membrane properties of CDKL5 iPS derived cortical neurons in Synaptojuice and Reduced Synaptojuice
A-C: Bar charts plotting resting membrane potential (A), capacitance (B) and input resistance of iPS derived neurons harboring both wild type CDKL5 (blue bars) and the c.1375C>T p.Q459X mutant CDKL5 (orange bars) matured over a course of 21 days post plating in line with the Synaptojuice protocol. Neurons underwent whole cell patch clamp experiments DIV21 to generate the data shown. Half of the cells were switched to reduced Synaptojuice, otherwise normal Synaptojuice deficient of BDNF, LM22A4 and CHIR99021, after 14 days post plating.
Data shown here as mean +/- SEM, p** <0.01
Abbreviations: CDKL5: cyclin dependent kinase like five, **WT**: wild type, **DIV**: days in vitro, **iPS**: induced pluripotent stem cells

week of maturation. Whole-cell patch-clamp experiments were then performed and basic functional properties were examined, as before.

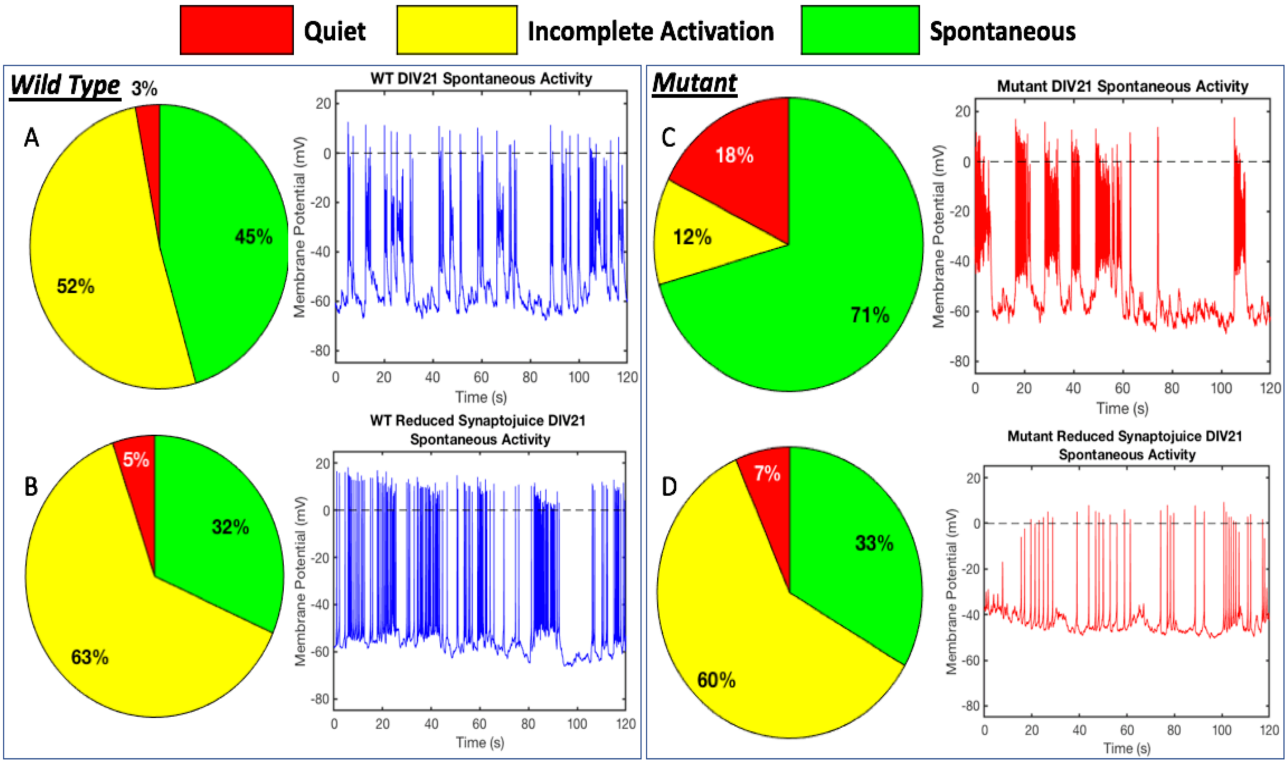

Figure 4.8: Spontaneous activity levels of CDKL5 iPS derived cortical neurons in Synaptojuice and Reduced Synaptojuice
Pie charts, accompanied by exemplary recordings, showing the levels of spontaneous activity measured from iPS derived neurons harboring the wild type CDKL5 and the c.1375C>T p.Q459X mutant CDKL5 during whole cell patch clamp experiments at DIV21. Half of the cells were switched to Reduced Synaptojuice, otherwise normal Synaptojuice deficient of BDNF, LM22A4 and CHIR99021, after 14 days post plating whilst the other half were left to mature in Synaptojuice. The red segments in the pie charts represent quiet cells devoid of action potentials, the yellow represents incomplete activation of action potentials and the green represent spontaneous activity where action potentials result in complete depolarisation of the neurons crossing 0mV.
A-B: pie charts and exemplary recordings of wild type CDKL5 neurons at DIV21 respectively following maturation in Synaptojuice and Reduced Synaptojuice respectively.
C-D: pie charts and exemplary recordings of wild type CDKL5 neurons at DIV21 respectively following maturation in Synaptojuice and Reduced Synaptojuice respectively.
Data shown here as mean +/- SEM
Abbreviations: CDKL5: cyclin dependent kinase like five, **WT**: wild type, **DIV**: days in vitro, **iPS**: induced pluripotent stem cells

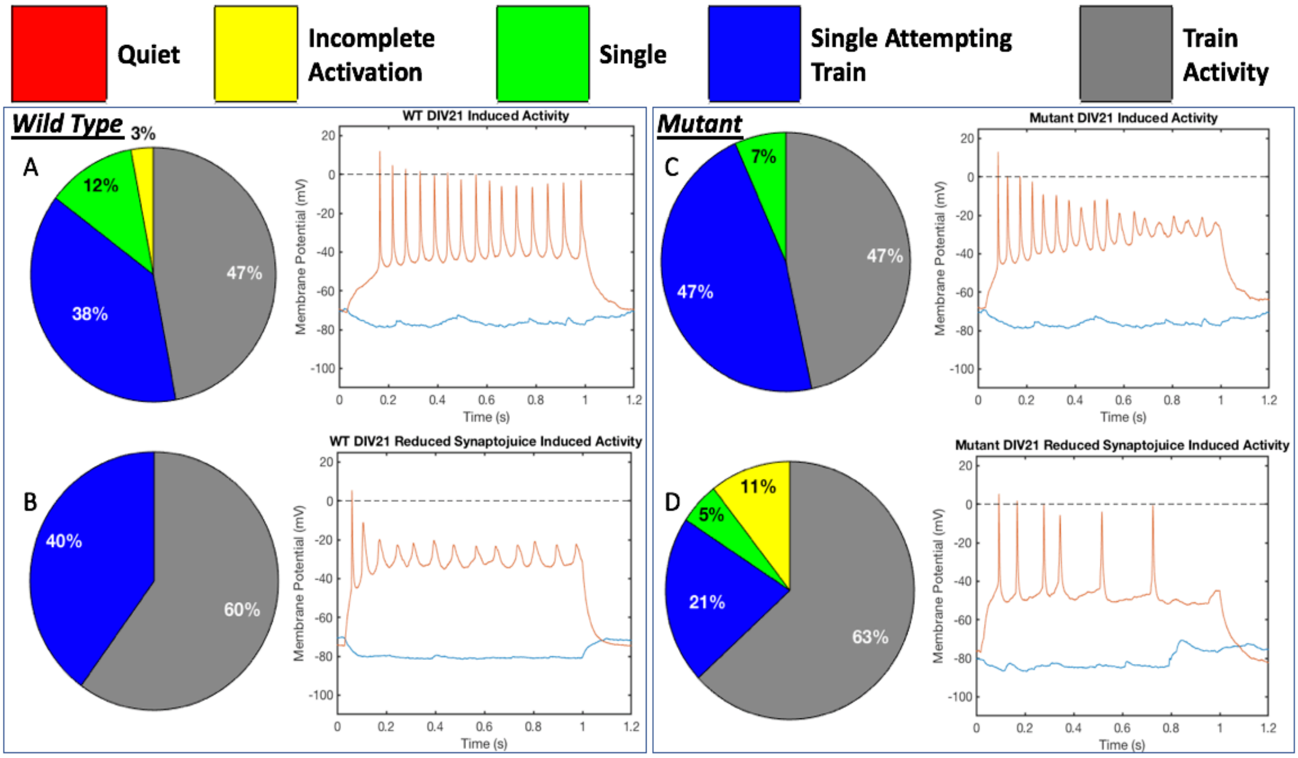

Figure 4.9: Induced activity levels of CDKL5 iPS derived cortical neurons in Synaptojuice and Reduced Synaptojuice

Pie charts, accompanied by exemplary recordings, showing the levels of induced activity measured from iPS derived neurons harboring the wild type CDKL5 and the c.1375C>T p.Q459X mutant CDKL5 during whole cell patch clamp experiments, during maturation in line with the Synaptojuice protocol. Half of the cells were were switched to Reduced Synaptojuice, otherwise normal Synaptojuice deficient of BDNF, LM22A4 and CHIR99021, after 14 days post plating whilst the other half were left to mature in Synaptojuice. Experiments were performed at DIV21. The pie charts depict the proportions of cells exhibiting quiet and devoid of action potentials (red), incomplete activation of action potentials (yellow), a single action potential that results in complete depolarisation of the neuron (green), attempting train activity (blue) and trains of induced activity (grey).

A-B: pie charts and exemplary recordings of wild type CDKL5 neurons at DIV21 respectively following maturation in Synaptojuice and Reduced Synaptojuice respectively.

C-D: pie charts and exemplary recordings of wild type CDKL5 neurons at DIV21 respectively following maturation in Synaptojuice and Reduced Synaptojuice respectively.

Data shown here as mean +/- SEM.

Abbreviations: CDKL5: cyclin dependent kinase like five, **WT**: wild type, **DIV**: days in vitro, **iPS**: induced pluripotent stem cells

The control group data (regular Synaptojuice) are included from the data taken before the change in protocol (removal of GSK3β modulators present in Synaptojuice) and are reproduced from Figures 4.1 through 4.6, for a detailed explanation of the results see 4.4.1. Firstly, the passive membrane properties (resting membrane potential, input resistance and capacitance) were examined. No significant differences were observed in resting membrane potential (Figure 7A) and input resistance (Figure 4.7B). However, capacitance was significantly smaller in the mutant CDKL5 cells (13.66 +/- 11.68 pF) than the wild type cells in reduced Synaptojuice (25.97 +/- 3.67 pF, $p < 0.01$, Figure 4.7C). Taken together, these data suggest that removal of modulators of GSK3β has little difference on passive membrane properties. However, the mutant CDKL5 cells have a smaller capacitance suggestive of cells with a smaller soma and fewer, less extensive, projections.

Next, to determine whether removal of GSK3β modulators present in Synaptojuice would alter the levels of spontaneous and induced activity seen in mutant and wild type cells, the respective levels of activity were recorded, as before. Spontaneous activity was observed in current-clamp mode ($I = 0$) of the whole-cell patch clamp configuration and classified as either quiet, incomplete activation or spontaneous (as described in Chapter 2). The proportion of cells displaying spontaneous activity in wild type cells remained comparable in Synaptojuice (45 %, Figure 4.8A) and Reduced Synaptojuice (32 %, Figure 4.8B). However, the proportion of cells displaying spontaneous activity in mutant CDKL5 cells in reduced Synaptojuice was reduced from 71% to 33% (Figure 4.8C-D). These data suggest that removal of GSK3β modulators makes very little difference to wild type CDKL5 neurons. However, it results in reduced the level of spontaneous activity seen in mutant CDKL5 cells.

Induced activity was then examined during a current-step protocol (from -70mV, as described in Chapter 2) and classified as either quiet, incomplete activation, single, single attempting train or train activity The proportion of cells exhibiting trains of activity increased in wild type CDKL5 cells when Synaptojuice was reduced (47 % to 60 %, Figure 4.9A-B). This was also observed in the mutant CDKL5 line to a similar degree (47 % to 63 %, Figure 4.9C-D). These results imply that removal of GSK3β modulators present in Synaptojuice increases the proportion of cells exhibiting trains of activity in both wild type and mutant CDKL5 neurons to a similar degree.

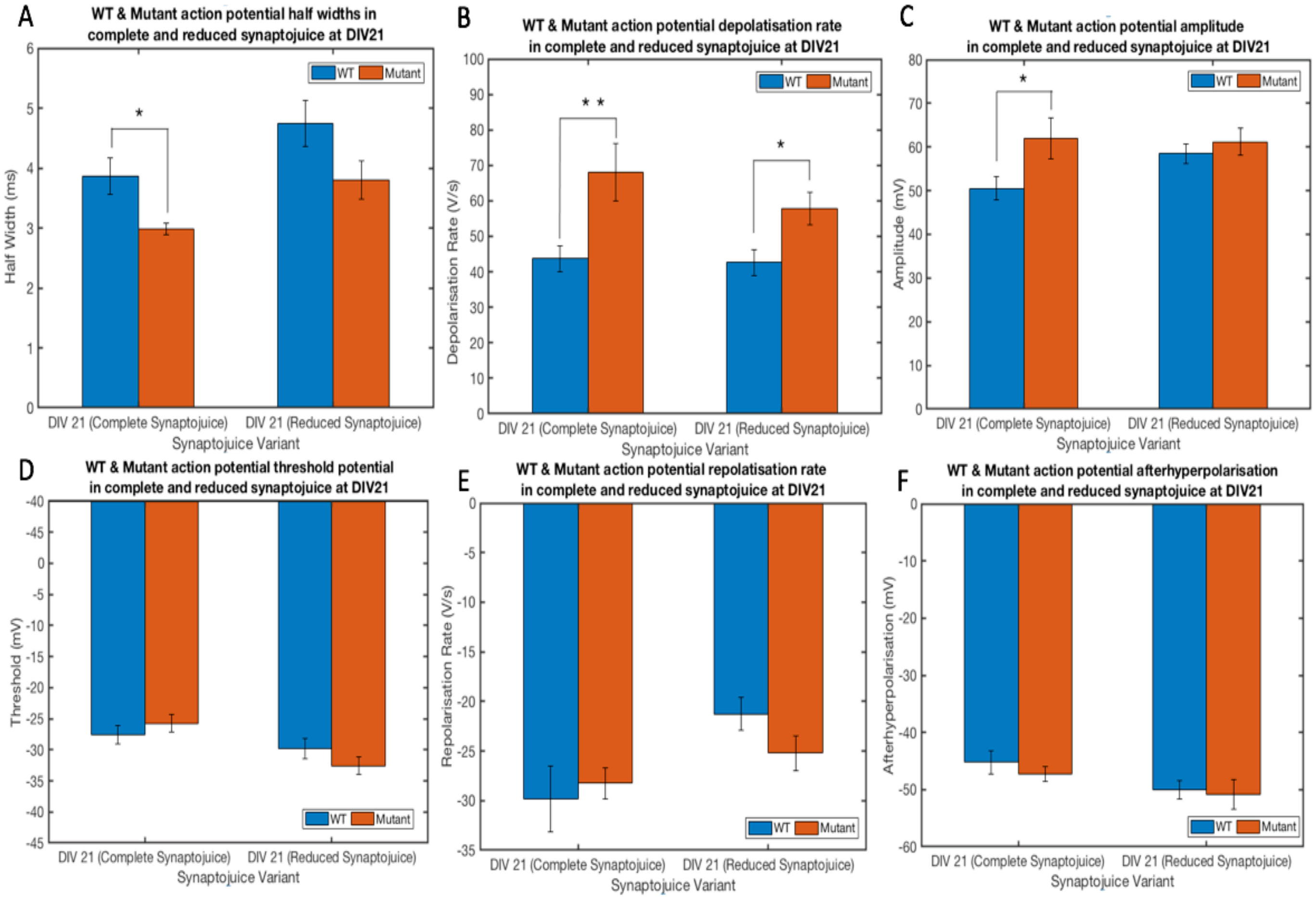

Figure 4.10: Action potential properties of CDKL5 iPS derived cortical neurons in Synaptojuice and Reduced Synaptojuice

A-F: Bar charts plotting resting action potential half-width (A), amplitude (B), depolarization rate (C), threshold potential (D), repolarization rate (E) and afterhyperpolarisation (F) of iPS derived neurons harboring both wild type CDKL5 (blue bars) and the c.1375C>T p.Q459X mutant CDKL5 (orange bars) matured over a course of 21 days post plating in line with the Synaptojuice protocol. Half of the cells were switched to Reduced Synaptojuice, otherwise normal Synaptojuice deficient of BDNF, LM22A4 and CHIR99021, after 14 days post plating whilst the other half were left to mature in Synaptojuice. Whole cell patch clamp experiments were performed at DIV21.

Data shown here as mean +/- SEM. p* <0.05, p** <0.01

Abbreviations: CDKL5: cyclin dependent kinase like five, **WT**: wild type, **DIV**: days in vitro, **iPS**: induced pluripotent stem cells

Detailed spike analysis showed that the action potential halfwidth, which was already shown to be significantly different between wild type and mutant CDKL5 neurons in regular Synaptojuice at DIV21 ($p < 0.05$, reproduced from Figure 4.4A) was not affected by removal of Synaptojuice components thought to interact with GSK3β (Figure 4.10A). In complete Synaptojuice, where the depolarisation rate was already shown to be significantly faster in the mutant CDKL5 cells compared to their WT counterparts ($p < 0.01$, reproduced from Figure 4.4B), reduced Synaptojuice still supported this significant difference (42.64 +/- 1.7 V/s in wild type cells and 57.88 +/- 4.59 V/s in mutant cells, $p < 0.05$, Figure 4.10B). The difference between mutant CDKL5 action potential amplitude and wild type amplitude was no longer statistically significantly different in reduced Synaptojuice (Figure 4.10C) having already been shown to be significant in complete Synaptojuice ($p < 0.05$, reproduced from Figure 4.4C). No significant differences when Synaptojuice was removed were observed in action potential threshold (Figure 4.10D), repolarisation rate (Figure 4.10E) and afterhyperpolarisation potential (Figure 4.10F). Taken together, these data suggest that removal of GSK3β from Synaptojuice has little to no effect on the properties of the individual induced action potentials in either wild type and mutant CDKL5 neurons at DIV21.

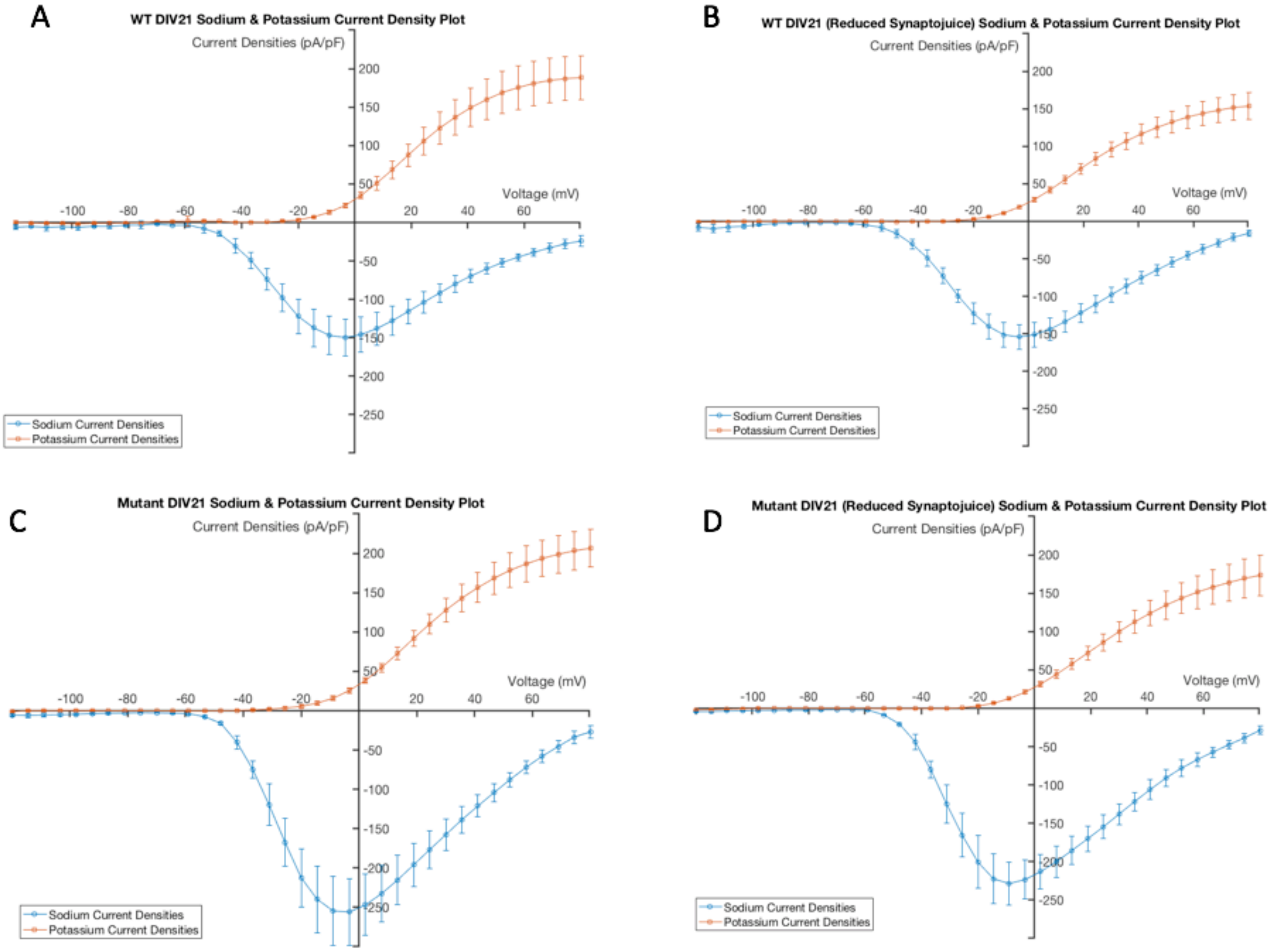

Figure 4.11: Sodium and potassium current densities in CDKL5 iPS derived neurons in Synaptojuice and Reduced Synaptojuice

Mean sodium and potassium current density plots obtained during whole cell patch clamp experiments. Half of the cells were switched to Reduced Synaptojuice, otherwise normal Synaptojuice deficient of BDNF, LM22A4 and CHIR99021, after 14 days post plating whilst the other half were left to mature in Synaptojuice. Whole cell patch clamp experiments were performed at DIV21.

A-C: mean current density against voltage plots derived for maximum voltage-activated Na^+ (blue) and K^+ currents (orange) taken from iPS derived cortical neurons harbouring the wild type CDKL5.

D-F: mean current density against voltage plots derived for maximum voltage-activated Na^+ (blue) and K^+ currents (orange) taken from iPS derived cortical neurons harbouring the c.1375C>T p.Q459X mutant CDKL5.

Data shown here as mean +/- SEM.

Abbreviations: CDKL5: cyclin dependent kinase like five, **WT**: wild type, **DIV**: days in vitro, **iPS**: induced pluripotent stem cells

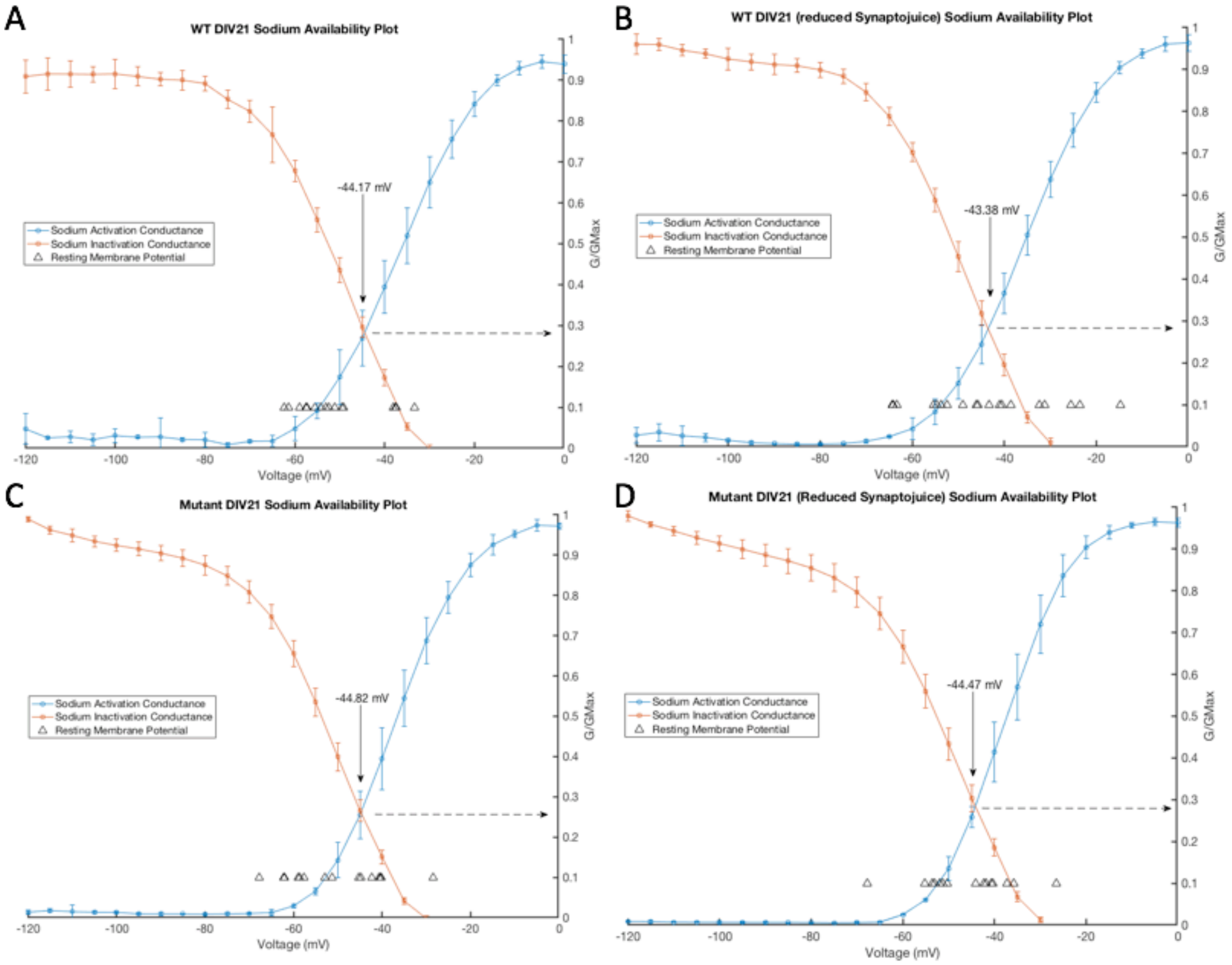

Figure 4.12: Sodium availability in CDKL5 iPS derived neurons in Synaptojuice and Reduced Synaptojuice
Mean mean fractional conductance (*G*/*G*max) plots for voltage activation (blue) and inactivation (orange) of sodium currents obtained during whole cell patch clamp experiments of iPS derived neurons harbouring the wild type CDKL5 and the c.1375C>T p.Q459X mutant CDKL5. Peak *G*/*G*max is indicated by the arrow. Individual *V*m values are plotted on each graph by the white triangles. Half of the cells were switched to Reduced Synaptojuice, otherwise normal Synaptojuice deficient of BDNF, LM22A4 and CHIR99021, after 14 days post plating whilst the other half were left to mature in Synaptojuice. Whole cell patch clamp experiments were performed at DIV21
A-C: mean sodium availability plots of iPS derived neurons harbouring the wild type CDKL5.
D-E: mean sodium availability plots of iPS derived neurons harbouring the c.1375C>T p.Q459X mutant CDKL5.
Data shown here as mean +/- SEM.
Abbreviations: CDKL5: cyclin dependent kinase like five, **WT**: wild type, **DIV**: days in vitro, **iPS**: induced pluripotent stem cells

Lastly, the voltage-activated sodium and potassium currents were interrogated using a voltage-step protocol (as described in Chapter 2). Figure 4.11 shows that removal of GSK3β modulators appears to have very little impact on sodium and potassium current density properties in both wild type and mutant cells. This also appears to be true for the activation/inactivation profiles represented in Figure 4.12. Sodium availability windows, G/Gmax peaks and proportion of cells within the sodium availability window remained roughly consistent despite removal of GSK3β modulators in Synaptojuice. Taken together, these data suggest that the presence or absence of GSK3β modulators in Synaptojuice has little bearing on sodium and potassium currents in patient iPSC derived neurons harbouring either wild type or mutant CDKL5.

When considering all of these data together, few striking differences are seen in the basic properties between wild type CDKL5 neurons and mutant CDKL5 neurons when the modulators of GSK3β are removed. This suggests BDNF, LM22A4 and CHIR99021 are unlikely to be masking any functional differences, or that whole cell patch clamp recordings are not able to reveal these differences.

4.4.3 Mutated CDKL5 has little impact on the ability of iPSC-derived to display network activity at DIV21

Interrogation of the differences between wild type and mutant CDKL5 neurons via whole-cell patch clamp experiments revealed few differences between their maturation profiles. Although whole-cell patch-clamp is an invaluable tool to investigate the membrane properties of electrically active cells, this technique can only investigate a single cell at a time. As epilepsy is, in part, the result of changes in network activity across huge populations of neurons, patient iPS derived neural progenitor cells, were plated onto commercially available MEA plates in order to investigate network activity at DIV21. The spike raster plots clearly display unsynchronised activity across all wells in both wild type CDKL5 neurons (Figure 13A) and mutant CDKL5 neurons (Figure 4.14A), supported by similar three-dimensional spike count plots (Figures 4.13C and 4.14C) and cross correlation matrices (Figures 4.13B and 4.14B). Mean synchronisation indexes from the two populations the two were also not significantly different. Taken together, these data suggest that this mutation in CDKL5 does not lead to any significant alteration in network activity in patient iPS derived cortical neurons, a conclusion consistent with the single cell data derived from whole-cell patch-clamp recordings.

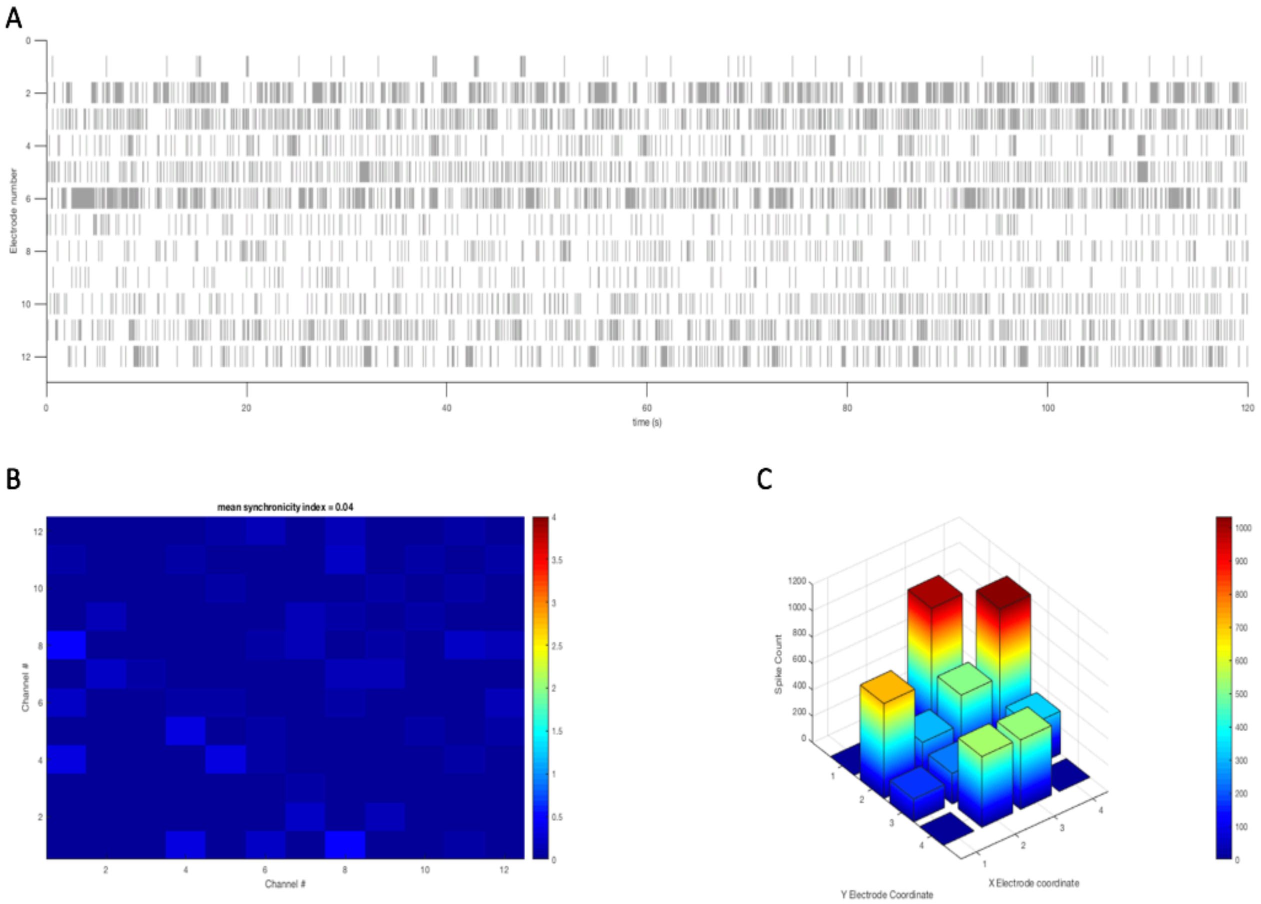

Figure 4.13: Exemplary MEA analysis from wild type CDKL5 neurons at DIV21 in Synaptojuice
iPS derived neurons harboring the wild type CDKL5 were plated on commercially available MEA plates and matured in line with the Synaptojuice protocol and recorded at DIV21

A: Spike raster plots showing an individual line representing a spike that exceeded five standard deviations of the background noise from each electrode (y axis) over time in a single well.

B: cross correlation matrix heat map showing level of synchronization between electrodes and mean synchronicity index between 0-5 (top) calculated for the top left triangle (bottom right triangle is a mirror image).

C: 3D bar plot displaying spike count per electrode from the well.

Abbreviations: CDKL5: cyclin dependent kinase like five, **DIV**: days in vitro, **iPS**: induced pluripotent stem cells, **MEA:** multi electrode array

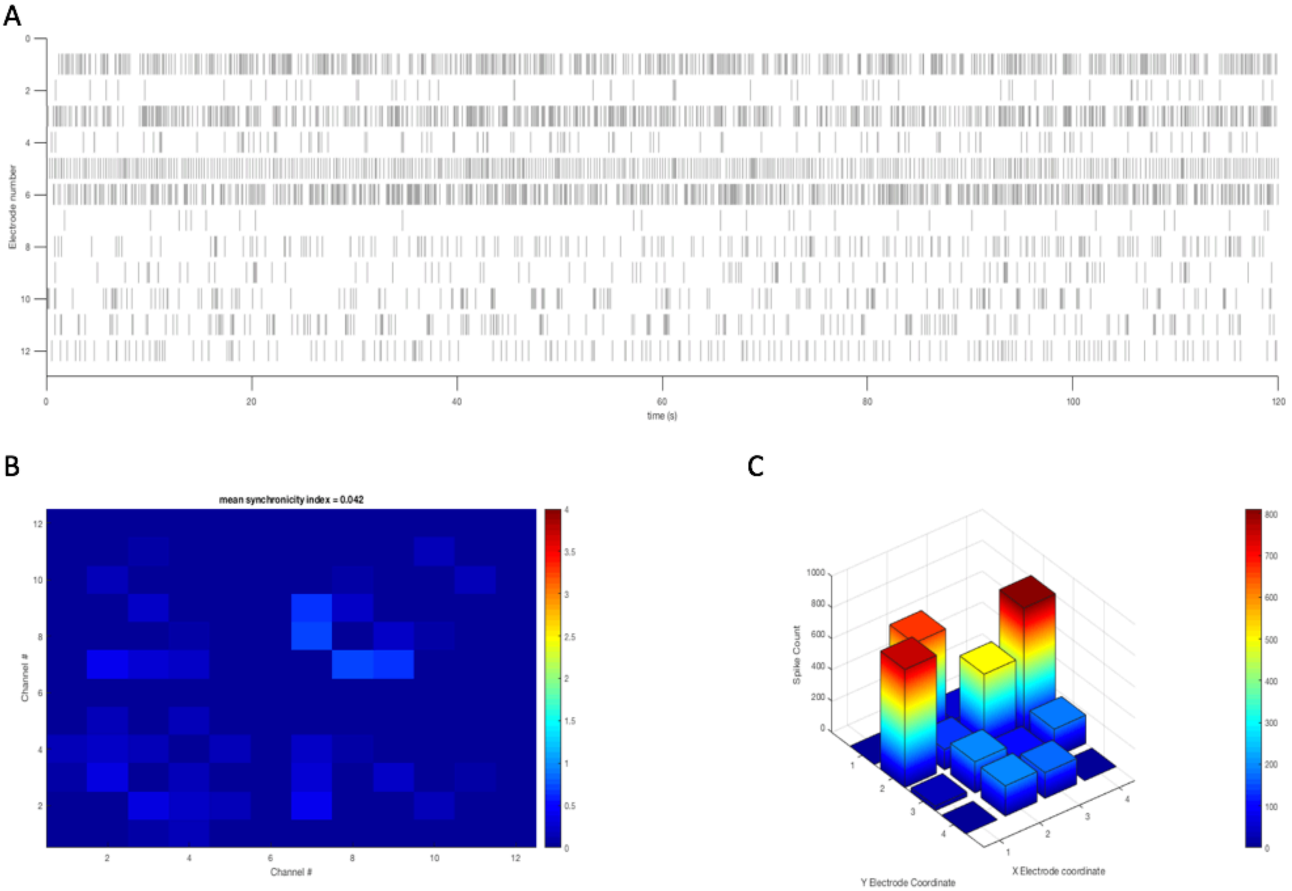

Figure 4.14: Exemplary MEA analysis from mutant CDKL5 neurons at DIV21 in Synaptojuice
iPS derived neurons harboring the c.1375C>T p.Q459X mutant CDKL5 were plated on commercially available MEA plates and matured in line with the Synaptojuice protocol and recorded at DIV21.
A: Spike raster plots showing an individual line representing a spike that exceeded five standard deviations of the background noise from each electrode (y axis) over time in a single well.
B: cross correlation matrix heat map showing level of synchronization between electrodes and mean synchronicity index between 0-5 (top) calculated for the top left triangle (bottom right triangle is a mirror image).
C: 3D bar plot displaying spike count per electrode from the well.
Abbreviations: CDKL5: cyclin dependent kinase like five, **DIV**: days in vitro, **iPS**: induced pluripotent stem cells, **MEA:** multi electrode array

4.4.4 Removal of BDNF, CHIR99021 and LM22A4 from Synaptojuice medium reveals hyper synchronised network activity in the mutant-CDKL5 harbouring neurons

The removal of BDNF, CHIR99021 and LM22A4, (termed ‘Reduced Synaptojuice’) revealed only small differences in single cell properties. To investigate the effect of removal of these small molecules on neuronal network activity, thought to be key in epilepsy, MEA recordings were made following switching from Synaptojuice to Reduced Synaptojuice for the final week of maturation. The spike raster plot of the mutant CDKL5 MEA activity in Reduced Synaptojuice shows striking hyper-synchronised network activity (highlighted in red, Figure 4.16A). Although, the total three-dimensional spike count plots do not differ dramatically between wild type (Figure 4.15C) and mutant (Figure 4.16C), the hyper-synchronicity as a result of Synaptojuice reduction is further highlighted by the vastly different cross correlation matrices (Figure 4.15B and Figure 4.16 B). Figure 4.17 shows the mean synchronisation index of the wild type and mutant CDKL5 lines in both Synaptojuice and Reduced Synaptojuice. The mean synchronisation index of the mutant CDKL5 neurons in Reduced Synaptojuice (1.78 +/- 0.39) was significantly higher than the synchronisation index of both the wild type neurons in Reduced Synaptojuice (0.14 +/- 0.11, $p < 0.01$) and the mutant CDKL5 neurons in Synaptojuice (0.04 +/- 0.01, $p < 0.001$). Taken together, these data strongly suggest that removal of the modulators of GSK3β (BDNF, CHIR99021 and LM22A4) unmasks hyper-synchronised network activity, a characteristic disease phenotype of CDKL5-deficieny which is visible upon MEA analyses.

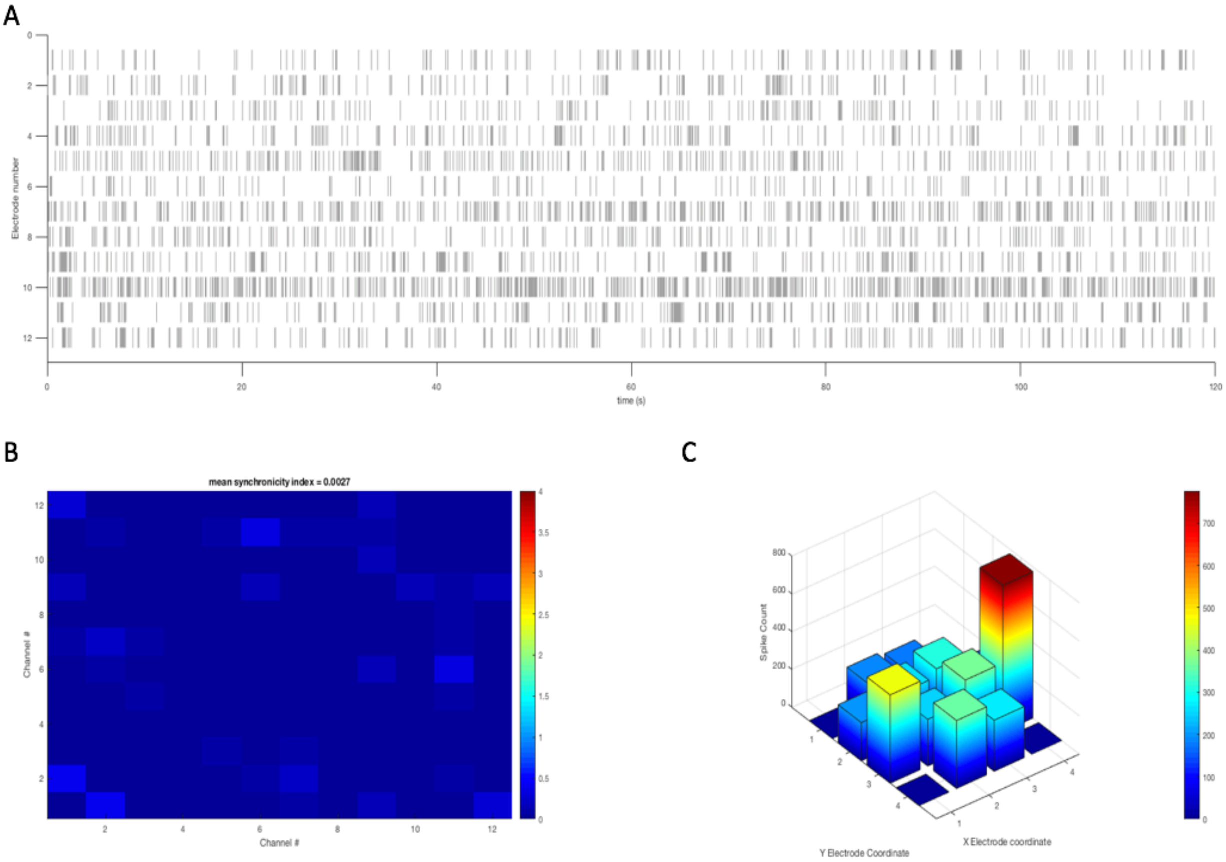

Figure 4.15: Exemplary MEA analysis from wild type CDKL5 neurons at DIV21 in Reduced Synaptojuice

iPS derived neurons harboring the wild type CDKL5 were plated on commercially available MEA plates and matured in line with the Synaptojuice protocol and recorded at DIV21. The cells were switched to Reduced Synaptojuice, otherwise normal Synaptojuice deficient of BDNF, LM22A4 and CHIR99021, after 14 days post plating.

A: Spike raster plots showing an individual line representing a spike that exceeded five standard deviations of the background noise from each electrode (y axis) over time in a single well.

B: cross correlation matrix heat map showing level of synchronization between electrodes and mean synchronicity index between 0-5 (top) calculated for the top left triangle (bottom right triangle is a mirror image).

C: 3D bar plot displaying spike count per electrode from the well.

Abbreviations: CDKL5: cyclin dependent kinase like five, **DIV**: days in vitro, **iPS**: induced pluripotent stem cells, **MEA:** multi electrode array

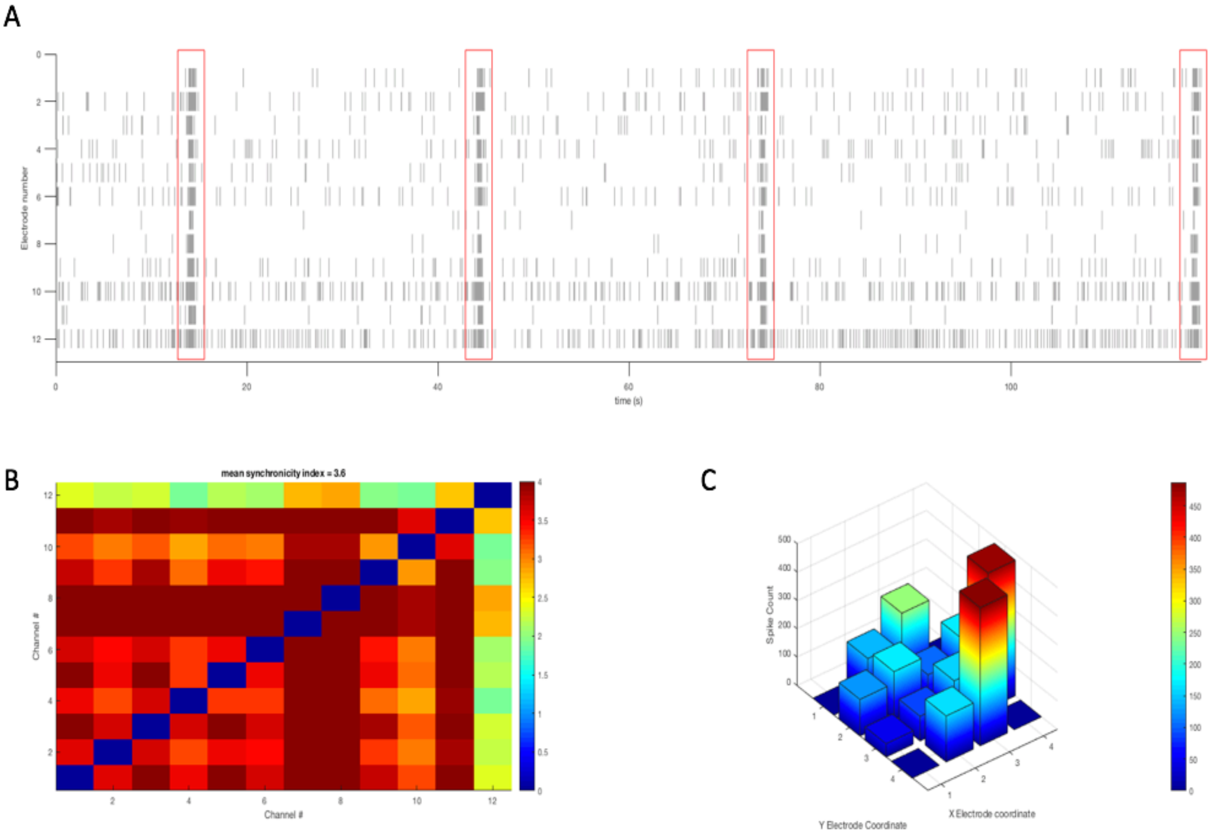

Figure 4.16: Exemplary MEA analysis from mutant CDKL5 neurons at DIV21 in Reduced Synaptojuice

iPS derived neurons harboring c.1375C>T p.Q459X mutant CDKL5 were plated on commercially available MEA plates and matured in line with the Synaptojuice protocol and recorded at DIV21. The cells were switched to Reduced Synaptojuice, otherwise normal Synaptojuice deficient of BDNF, LM22A4 and CHIR99021, after 14 days post plating.

A: Spike raster plots showing an individual line representing a spike that exceeded five standard deviations of the background noise from each electrode (y axis) over time in a single well. Synchronized bursts are highlighted in red.

B: cross correlation matrix heat map showing level of synchronization between electrodes and mean synchronicity index between 0-5 (top) calculated for the top left triangle (bottom right triangle is a mirror image).

C: 3D bar plot displaying spike count per electrode from the well.

Abbreviations: CDKL5: cyclin dependent kinase like five, **DIV**: days in vitro, **iPS**: induced pluripotent stem cells, **MEA:** multi electrode array

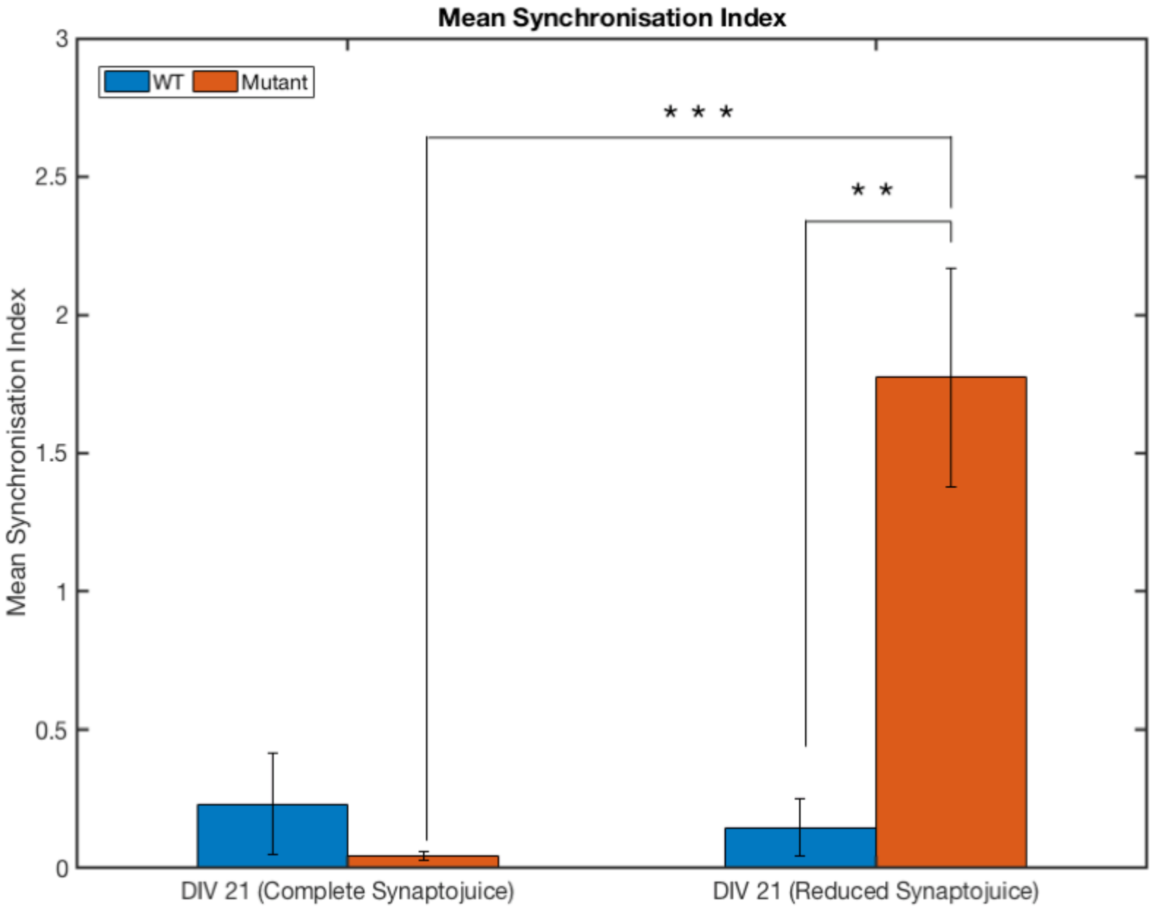

Figure 4.17: WT & Mutant mean synchronization index in complete and reduced Synaptojuice at DIV21.
iPS derived neurons harboring c.1375C>T p.Q459X mutant CDKL5 (orange) and wild type CDKL5 (blue) were plated on commercially available MEA plates and matured in line with the Synaptojuice protocol and recorded at DIV21. Half of the cells were switched to Reduced Synaptojuice otherwise normal Synaptojuice deficient of BDNF, LM22A4 and CHIR99021, after 14 days post plating whilst the other half were left to mature in Synaptojuice prior to recording. Data shown here as mean +/- SEM. p* <0.05, p** <0.01
Abbreviations: CDKL5: cyclin dependent kinase like five, **DIV**: days in vitro, **iPS**: induced pluripotent stem cells, **MEA:** multi electrode array, **WT**: wild type

3.5 Discussion & Conclusion

3.5.1 CDKL5 and GSK3β signalling

To date the precise physiological role of CDKL5, a serine-threonine kinase, remains unclear. Roles in neuronal morphogenesis are amongst the most commonly reported potential functions, with decreased dendritic arborisation and spine density seen *in vivo* (Chen et al., 2010a; Ricciardi et al., 2012; Fuchs et al., 2014; Della Sala et al., 2016) and *in vitro* (Ricciardi et al., 2012; Zhu et al., 2013). A second commonly implicated role is as a component of the GSK3β signalling pathway, as suggested in experiments designed to disrupt GSK3β signalling (Wang et al., 2012; Fuchs et al., 2014) and by the beneficial effects of GSK3β inhibition, *in vivo* (Fuchs et al., 2014, 2018). Whilst the data presented in my thesis focus primarily on electrophysiological properties, one interesting result stands out. Cellular capacitance, which is a reliable indicator of neuronal size and complexity; a larger cell being able to hold more charge and is, therefore, said to have a larger capacitance. Figure 4.1C shows that the cellular capacitance of both wild type and mutant CDKL5 iPSC-derived neurons mature at a similar rate and are not significantly different at any point, suggesting the mutation has no impact on neuronal size and complexity. However, when the modulators of the GSK3β (BDNF, CHIR99021 and LM22A4) were removed from Synaptojuice, the cellular capacitance was significantly smaller in CDKL5 mutant than in WT neurons (Fig.4.7C). Not only does this result support the existing literature which suggests a role of CDKL5 in neuronal morphogenesis, they also further implicate GSK3β in CDKL5-deficiency.

CHIR99021 is a well-documented GSK3β inhibitor(Chen et al., 2014; Wu et al., 2015; Huang et al., 2017),whereas the inhibitory effect of BDNF and/or LM22A4 on GSK3β is less direct. BDNF initiates it’s effect largely through the tropomysin receptor kinase B (TrkB) signalling cascade (Gupta et al., 2014) which in turn actives phosphatidylinositide 3-kinase (PI3K) and Akt (otherwise known as protein kinase B). Akt is a serine/threonine kinase that inhibits the action of GSK3β through phosphorylation of the Ser9 residue (Hu et al., 2013). Removal of BDNF results in reduced TrkB activation and a consequent reduction in GSK3β inactivation. LM22A4, a potent TrkB agonist, inhibits the TrkB activation (Massa et al., 2010), therefore reducing GSK3β inactivation by the same pathway. Increased GSK3β activation has been shown to result in neuronal cell death (Lucas et al., 2001; Mishra et al., 2007) and increased sodium currents resulting in increased spontaneous action potentials (Paul et al., 2016), markers of neurodegeneration and epilepsy, respectively. Increased sodium currents have been reported as a causal factor behind the epilepsy in a related disorder, Dravet's Syndrome (Liu et al., 2013), and decreased neuronal survival is commonly reported in CDKL5 studies (Fuchs et al., 2014; Trazzi et al., 2016). Interestingly, decreased microtubule polymerisation through inhibition of CRMP2 (Fukata et al., 2002; Yoshimura et al., 2005) has also been reported as a consequence of increased GSK3β activation, potentially accounting for the decreased dendritic arborisation seen in the literature and decreased cellular capacitance seen here. The crucial role of the GSK3β signalling cascade in CDKL5 was further supported by the work of Fuchs *et al.,* that highlighted components of the GSK3β pathway downstream of PI3K exhibited decreased phosphorylation (Fuchs et al., 2014) in a knockout model of CDKL5 deficiency. As the mutation studied here is a nonsense mutation (Zhao et al., 2014) resulting in either decreased levels of the protein or non-functional versions of it, it can be expected that the mutation would also result in decreased phosphorylation of GSK3β. It is as yet unclear whether the serine/threonine kinase activity of CDKL5 works directly or indirectly on GSK3β.

Another target implicated in the pathogenesis of CDKL5-deficiency is histone deacetylase 4 (HDAC4). HDAC4 is thought to play crucial roles in the transcriptional regulation of processes essential for synaptic plasticity (Sando et al., 2012), a process thought to be crucial in learning and memory. CDKL5-deficiency patients often show striking cognitive deficits. Much less research emphasis is focused on HDAC4 in CDKL5-deficiency. However, treatment with the HDAC4 inhibitor, LMK235, improved both memory performance and neuronal survival in mice (Trazzi et al., 2016).

3.5.2 Modelling difficult-to-manage epileptic disorders

One of the biggest problems associated with the development of novel therapeutics for CDKL5-deficiency is that none of the existing animal models exhibit the most defining clinical feature of CDKL5-deficiency: epilepsy (Chen et al., 2010b; Ricciardi et al., 2012; Amendola et al., 2014; Della Sala et al., 2016). A combination of the consequences of increased GSK3β activity, caused by decreased inactivation by loss of CDKL5 kinase activity, could lead to the life-limiting epilepsy seen in patients. This is further supported by the striking differences seen in network activity when GSK3β inhibitors are removed from the media (Fig4.16 and Fig.4.17). Whilst synchronisation is widely accepted as a fundamental part of physiology and pathophysiology within the CNS (Varela et al., 2001), hyper-synchronised activity is more commonly associated with epilepsy (Lehnertz et al., 2009). Seen in Figure 16, the repeated synchronised activity recorded at every electrode in the well can be seen as hyper-synchronicity. Furthermore, as this hyper-synchronicity is only seen when GSK3β inhibitors are removed from the maturation media and, therefore, no longer masking the effect of decreased CDKL5 related GSK3β inhibition, it can be suggested that the hyper-synchronised network activity visible on the MEA could be used a surrogate of the epileptic phenotype of CDKL5-deficienc in drug-screening studies.

It is currently unclear how decreased inactivation, and subsequently increased activity, of GSK3β can lead to the epilepsy seen in patients and hypersynchronization in the MEA studies. Paul *et al.,* suggested that increased GSK3β activity caused increased levels of spontaneous activity by altering the threshold potential and, therefore, increasing spontaneous activity (Paul et al., 2016). It was noted that neurons with a mutant CDKL5 exhibited increased levels of spontaneous activity at all stages of maturation (Figure 4.2), potentially supportive of Paul's suggestion. This is especially interesting considering no clear difference in resting V_m or input resistance suggestive of increased presynaptic input from neighbouring cells. However, in the absence of GSK3β inhibitors (and therefore increased GSK3β activity) the level of spontaneous activity dropped to that of wild type levels (Fig.4.8). Increased sodium currents (Fig.4.11) and altered threshold potentials (Fig.4.10) as a result of GSK3β dis-inhibition were not observed during the experiments conducted in this study. Furthermore GSK3β dis-inhibition appeared to reduce the level of spontaneous activity closer to that of wild type neurons (Figure 8). Seemingly contradictorily, Ricciardi et al., suggested that decreased CDKL5 levels resulted in decreased the numbers of excitatory synapses and, as a consequence, fewer miniature excitatory post-synaptic currents (Ricciardi et al., 2012). CDKL5's reported interactions with post-synaptic density protein 95 (PSD-95) (Ricciardi et al., 2012; Della Sala et al., 2016) and amphiphysin 1 (Sekiguchi et al., 2013), proteins involved in synapse formation and vesicle endocytosis, seem to support the suggestions made by Ricciardi *et al.,* yet do not shed light on how defects in CDKL5 can lead to epilepsy seen in patients. However, the results presented herein support the existing literature surrounding the central role of GSK3β in the pathogenesis of CDKL5-deficiency.

The promising early results shown here suggest that the mutant CDKL5 did not appear to cause functional differences on a single cell level (Fig.4.1 through Fig.4.6). However, when recording networks of activity on MEA plates, significant differences were seen in synchronicity. This is of particular interest as these data suggest human iPSC derived from patients are able to model the epilepsy seen in patients, a key feature missing from animal studies. The presence of such a defining clinical feature validates the use of patient iPSC as a model for CDKL5-deficiency. The presence of this phenotype on the MEA present an exciting opportunity to test the efficacy of existing therapeutic targets such as the HDAC4 inhibitor LMK235 (Trazzi et al., 2016), GSK3β inhibitor Tideglusib (Fuchs et al., 2018) and the positive allosteric GABA modulator Ganaxolone (Carter et al., 1997) currently in clinical trials (ClinicalTrials.gov, 2015). Furthermore, the presence of this previously difficult to model phenotype allows for the testing of novel therapeutic compounds on a high throughput scale not previously available.

Chapter 5 - Stem cell based cell replacement therapies for Huntington's Disease

5.1 Introduction

The fatal neurodegenerative condition Huntington's Disease (HD) is caused by a mutation in the huntingtin protein. Under physiological circumstances, the gene responsible for production of the huntingtin protein contains < 35 CAG repeats (Rubinsztein et al., 1996; Craufurd et al., 2001) that are translated into a polyglutamine sequence (PolyQ). However, patients show incomplete penetrance between 36 and 40 CAG repeats and complete penetrance above 40 CAG repeats. This expanded PolyQ sequence results in severe movement, cognitive and psychiatric impairment (Craufurd et al., 2001) at a mean age of onset of 35 and is usually fatal in 15-20 years following onset of symptoms. The severity and age of onset has been reported to scale with the length of CAG repeat (Rubinsztein et al., 1996), whilst environmental and other genetic factors are thought to influence this further (Rosenblatt et al., 2001; Wexler et al., 2004; Chattopadhyay et al., 2005). HD contributes to dementia, the single leading cause of death in the UK (Office for National Statistics, 2016), and as no effective therapy exists there is a pressing demand for research into innovative therapies.

Key to understanding to the HD pathogenesis is understanding the physiological role of the huntingtin protein. However, this remains elusive despite extensive studies. Huntingtin has thus far been implicated in multiple facets of neuronal development. Huntingtin KO mice perish prior to proper nervous system development, suggesting a vital role in embryonic development (Nasir et al., 1995). The protein has also been closely associated with BDNF production (Zuccato et al., 2001) and transport (Gauthier et al., 2004), as well as anti-apoptotic functions (Dragatsis et al., 2000; Zhang et al., 2003; Leavitt et al., 2006). Whilst all of these roles could potentially produce a phenotype consistent with that seen in HD, in man it appears that mutant huntingtin has a toxic gain of function (Walker, 2007), due to the formation of toxic protein aggregates, rather than a loss of function.

Perhaps the most defining feature of HD is the neuronal cell loss, seen earliest and most strikingly in medium spiny neurons (MSNs) of the striatum. It is thought that the mutant huntingtin aggregates contribute to this cell loss the increased caspase 3 activation (Zhang et al., 2006). Another hallmark of early stage HD is an apparent increased level of quinolinate in the striatum (Guidetti et al., 2004), a metabolite produced in the kynurenine pathway and potent excitotoxin within the CNS. Other metabolites of the kynurenine pathway include 3-hydroxykynurenine (3-HK) and kynurenate. Of interest is 3-HK, suggested to produce "HD-like" MSN cell death via free radical production (Okuda et al., 1996) and potentiation of the excitotoxic properties of quinolinate (Guidetti and Schwarcz, 2008). Quinolinate, or quinolinic acid, is believed to exert its toxic effects through excessive activation of N-methyl-D-aspartate receptors NMDARs (Perkins and Stone, 1983; Schwarcz and Köhler, 1983) and through the increase of glutamate in the synaptic microenvironment. Both increased presynaptic release of glutamate and decreased reuptake of glutamate (Tavares et al., 2000, 2002) contribute to elevated synaptic glutamate levels. The elevated glutamate leads to chronic NMDAR activation, subsequently resulting in massive Ca^{2+} influx. Ca^{2+} influx is vital during synaptic communication and long term potentiation, yet unregulated Ca^{2+} influx can initiate a cascade of reactions resulting in apoptotic cell death (Dong et al., 2009; Ndountse and Chan, 2009). The cell loss likely accounts for most of the HD phenotype, yet is not the only contributing factor. Indeed, impaired α-amino-3-hydroxy-5-methyl-4-isoxazolepropionic acid receptor (AMPAR) receptor trafficking has been reported to be impaired in HD potentially accounting for some of the cognitive impairment seen (Mandal et al., 2011; Zhang et al., 2018).

Whilst a small number of therapeutic targets exist to manage the symptoms of HD, such as anticonvulsants and antidepressants, no effective therapy exists that prevents or slows with the underlying neuronal loss. A cell replacement therapy, aimed at replacing the neurons lost to the disease process, may provide novel therapeutic strategy. Stem cells have the unique ability of being able to differentiate into any other cell type (dependant on their state of differentiation) and thus represent a tantalising possible solution to this problem. 'Repair HD' is a consortium of European universities collaborating over 5 years towards a stem cell based cell replacement therapy for HD (https://huntingtonstudygroup.org/hd-insights/repair-hd/). Having successfully developed protocols to differentiate stem cells into MSNs (Nicoleau et al., 2013; Arber et al., 2015; Noakes et al., 2015), the next stage was the transplantation of stem derived neural progenitors into an HD animal model in the hope this will inform the work needed to progress towards first-in-man clinical trials.

Animal models of HD consistently show behavioural improvements following embryonic (Campbell et al., 1993; Döbrössy and Dunnett, 2006; Aubry et al., 2008; Ma et al., 2012; Reidling et al., 2018) and foetal (McBride et al., 2004; Ryu et al., 2004) stem cell derived grafts. This behavioural improvement has been partially obtained in early transplant studies in human patients (Bachoud-Lévi et al., 2000; Gaura et al., 2004; Reuter et al., 2008). Despite several of these studies suggesting connectivity between host and graft tissue using immunohistochemistry (Ma et al., 2012), 18F-fleurodeoxyglucose (18F-FDG)-positron emission tomography (Gaura et al., 2004) and high performance liquid chromatography (Campbell et al., 1993), there is an almost complete lack of functional electrophysiological recordings supporting this suggestion. For a therapy to be fully effective, the engrafted neuronal progenitors must differentiate into functional MSNs and must electrophysiologically communicate with the host striatum.

5.2 Aims & Rationale

Transplant therapies have shown promise in a similar neurodegenerative condition, Parkinson’s Disease, and this project hopes to replicate this in HD. For any transplant therapy to be truly effective, functional synaptic integration is required. The best method to interrogate synaptic activity remains to be electrophysiology. This project will therefore electrophysiologically assess, via whole cell patch clamp *in vitro* and extracellular field potential recordings *ex vivo,* the functional integration of stem cell derived grafts into the striatum of a quinolinic acid lesioned rat model of Huntington Disease.

5.3 Methodology

Lister hooded rats (Charles River) were maintained, strereotaxically unilaterally lesioned via quinolinic acid (Sigma), grafted with a variety of stem cell-derived neuronal progenitors and culled prior to recordings in line with Home Office regulations by a fully trained colleague, Dr Ana Garcia Aguirre. The stem cells of origin were either human embryonic stem cell (hESC) neural progenitor cells, human whole ganglionic eminence (hWGE) cells of rat WGE (rWGE) cells. The stem cells were also transfected with green fluorescent protein (GFP) and luciferase via a trained colleague Dr Ngoc-Nga Vinh, with the assistance and supervision of Dr Amit Jathoul. Animals were culled, as described in Chapter 2 of this thesis, at 22 weeks (+/- 2 weeks) post transplantation for functional recordings. A detailed explanation of the electrophysiological experiments performed can also be found in Chapter 2 of this thesis.

It is important to note that very few previous studies have been performed/reported of striatal recordings in rat brain slice, making it important that lesion-only animals were included in the experimental strategy. Furthermore, unilateral lesions were employed in order that a non-lesioned, contralateral striatum was left intact for intra-slice comparisons and control recordings. Thus, the experimental groups were as follows; Group L consisted of lister hooded rats subject only to a single unilateral lesion (n = 16); Group A consisted of lister hooded rats subject to unilateral lesion, and subsequent grafting of hESC derived neural progenitors, transfected with GFP and luciferase, into the lesion site (n = 16); Group B consisted of lister hooded rats subject to unilateral lesion, and subsequent grafting of hWGE derived neural progenitors, transfected with GFP and luciferase, into the lesion site (n = 16); Group C consisted of lister hooded rats subject to unilateral lesion, and subsequent grafting of rWGE derived neural progenitors, transfected with GFP and luciferase, into the lesion site (n = 16);

5.4 Results

5.4.1 Intrastriatal synaptic transmission is AMPAR dependant

Prior to lesioning and grafting, it was important to establish the contributing factors of basal intrastriatal synaptic transmission. To do this, coronal slices were cut and extracellular field potential recordings were performed intrastriatally during perfusion of receptor antagonists. Figure 5.1B shows that following the recording of baseline activity (0.978 +/- 0.031 mV, n = 11), exposure to 5 μM 2,3-dihydroxy-6-nitro-7-sulfamoyl-benzoquinoxaline

(NBQX), a potent AMPAR antagonist, significantly reduced the peak amplitude of post-synaptic field potentials to 0.09 ± 0.01 mV, n = 11, $P < 0.01$). Co-application of 500 nM TTX, a potent and highly selective blocker of several classes of voltage-gated sodium channels, did not significantly reduce activity further (0.0151 +/- 0.0142, n = 11, $P = 0.1$,). It is important to note that NBQX exposure only impaired the post-synaptic field potential and not the afferent fibre volley, which itself is pre-synaptically mediated, as indicated by the exemplary traces in Figure 5.1C. Taken together, these data imply that intrastriatal synaptic transmission is mediated almost entirely by AMPARs, supporting the findings of Skiteva *et al* (Skiteva et al., 2018).

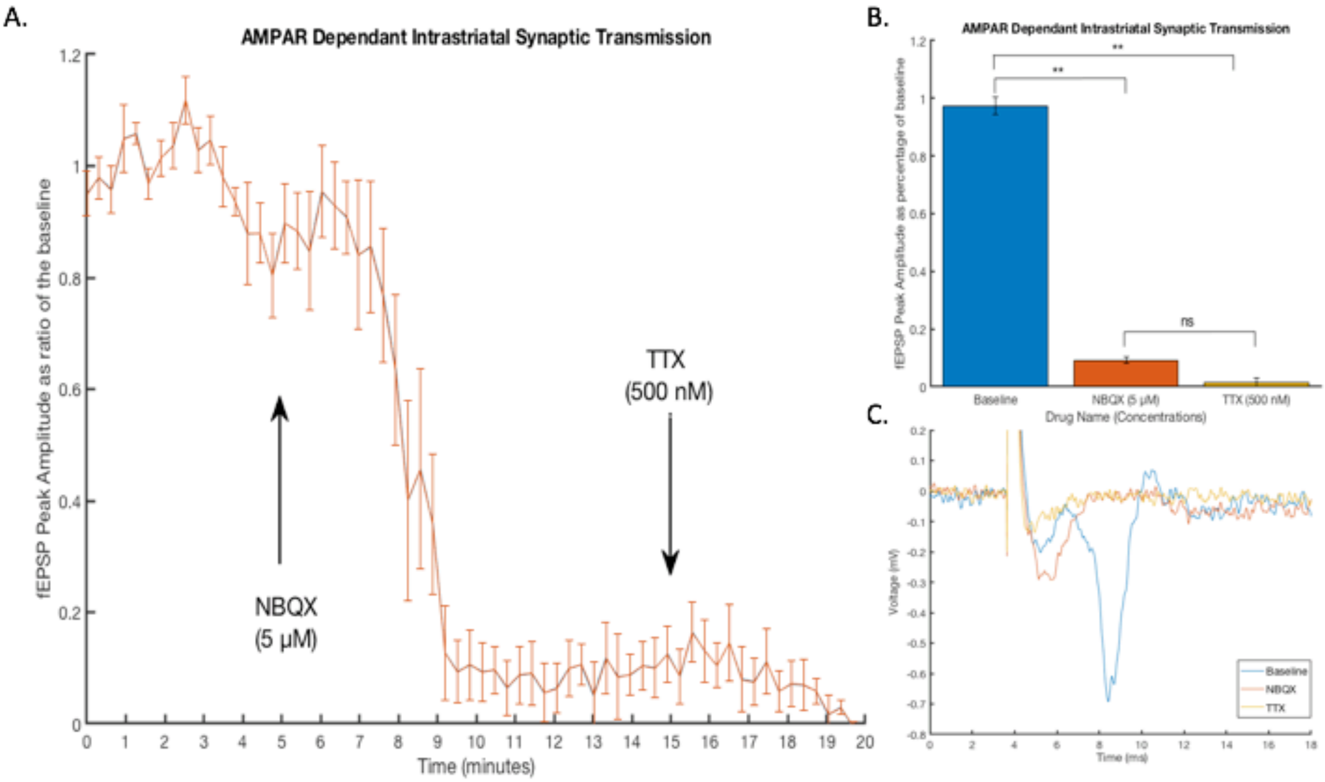

Figure 5.1: Intrastriatal synaptic transmission is AMPA-R dependent
Extracellular field potential recordings were performed intrastriatally in the contralateral hemisphere to interrogate healthy striatal function.
A: Intrastriatal fEPSP peak amplitude as compared to the average baseline peak amplitude (first 5 minutes of recording) following NBQX exposure (at 5 minutes) and TTX exposure (at 15 minutes),(n = 11).
B: Mean values +/- SEM during the final 2 minutes of the fEPSP peak amplitude compared to the baseline prior to drug exposure (blue, n = 11), following NBQX exposure (orange, n = 11) and TTX exposure (yellow, n = 11).
C: Exemplary fEPSP traces before drug exposure (blue), following NBQX exposure (orange) and following TTX (yellow).
Data shown as mean values +/- SEM. p** < 0.01.
Abbreviations: fEPSP: field excitatory post synaptic potential**, NBQX:** 2,3-dihydroxy-6-nitro-7-sulfamoyl-benzo[f]quinoxaline**, TTX:** Tetrodotoxin**, AMPA-R:** α-amino-3-hydroxy-5-methyl-4-isoxazolepropionic acid receptor

5.4.2 Quinolinic acid lesions impair synaptic transmission

To determine the effect of quinolinic acid lesion on the previously described intrastriatal synaptic transmission, coronal slices were taken and extracellular intrastriatal field potential recordings were performed in the ipsilateral hemisphere to the lesion and then compared to the contralateral hemisphere. Figure 5.2A shows a marked difference upon visual inspection through an infra-red camera. This visual disturbance also translated to a functional impairment. Figure 5.2B shows that intrastriatal synaptic transmission was significantly impaired in the hemisphere ipsilateral to the quinolinic acid lesion (-0.23± 0.03 mV, n = 8) when compared to the contralateral hemisphere (-0.79 ± 0.03 mV, n = 57, $P < 0.05$, Student's t-test). These data suggest the quinolinic acid lesions significantly impair Intrastriatal synaptic function and validate its use as an approach to generate an animal models of HD in this study.

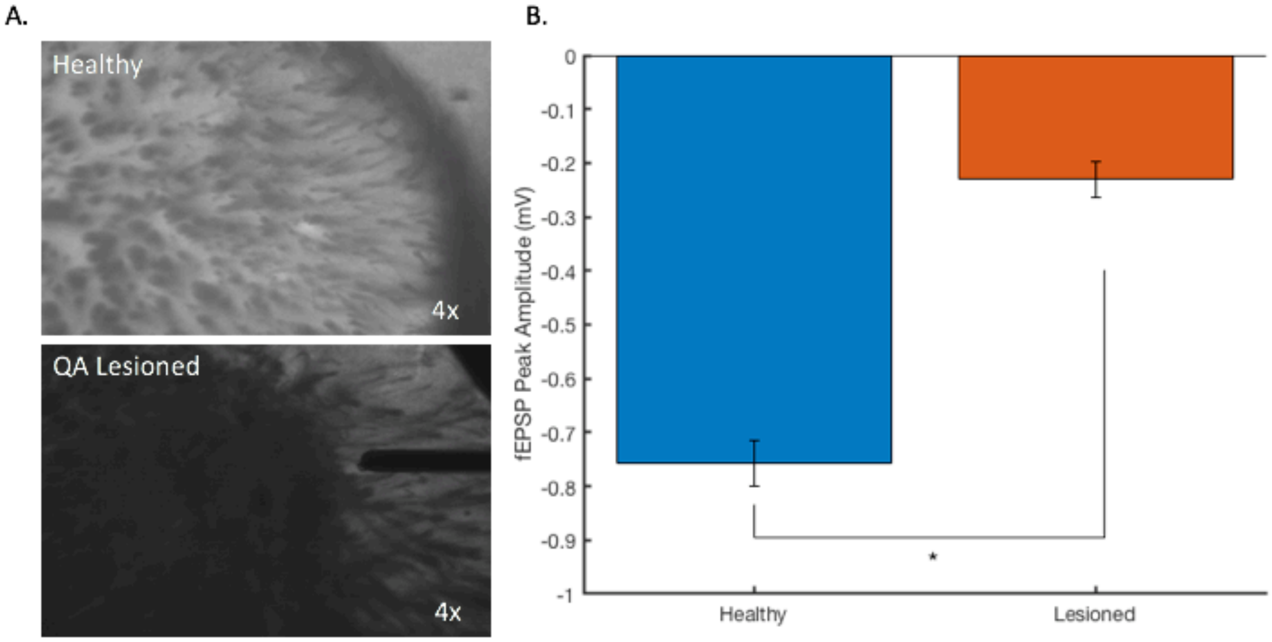

Figure 5.2: Quinolinic acid lesions significantly impair synaptic transmission in the rat striatum
Extracellular field potential recordings were performed intrastriatally in the contralateral hemisphere and in the lesioned hemisphere and images taken.
A: Healthy rat striatum (top left) and the quinolinic acid lesioned striatum (bottom left) imaged imaged through an infra-red camera.
B: Intrastriatal fEPSP peak amplitudes in both the healthy (blue, n = 57) and lesioned hemispheres (red, n = 8).
Data shown as mean values +/- SEM. p* < 0.05.
Abbreviations: QA: quinolinic acid, **fEPSP:** field excitatory post synaptic potential, ***:** p < 0.05

5.4.3 rWGE derived MSNs display the most mature functional properties at DIV21 in vitro

To validate the efficacy of stem cell differentiation to medium spiny neurons, and to act as a quality control, the stem cell derived neural progenitor cells (hESC/hWGE/rWGE) were plated onto glass coverslips and matured using the Synaptojuice protocol (Telezhkin et al., 2016). As already discussed in Chapter 5 at DIV21, the basic functional properties of the neurons were then interrogated using whole-cell patch-clamp electrophysiology. It is important to note, that these neural progenitors are from the same batches as used in the subsequent transplantation therapies, and were plated at the same time as transplantation (+/- 2 hours). Plotting the basic functional properties from each group on a polar plot normalised to the most mature value of each respective property, revealed rWGE-derived MSNs as the most mature in all properties (Fig.5.3A). rWGE-derived MSNs produced neurons were also capable of spontaneous activity (Fig.5.3C). These data suggest the rWGE-derived neural progenitor cells produce the most mature MSN-like neurons and may, therefore, be expected to provide the greatest functional improvement in the grafted animals.

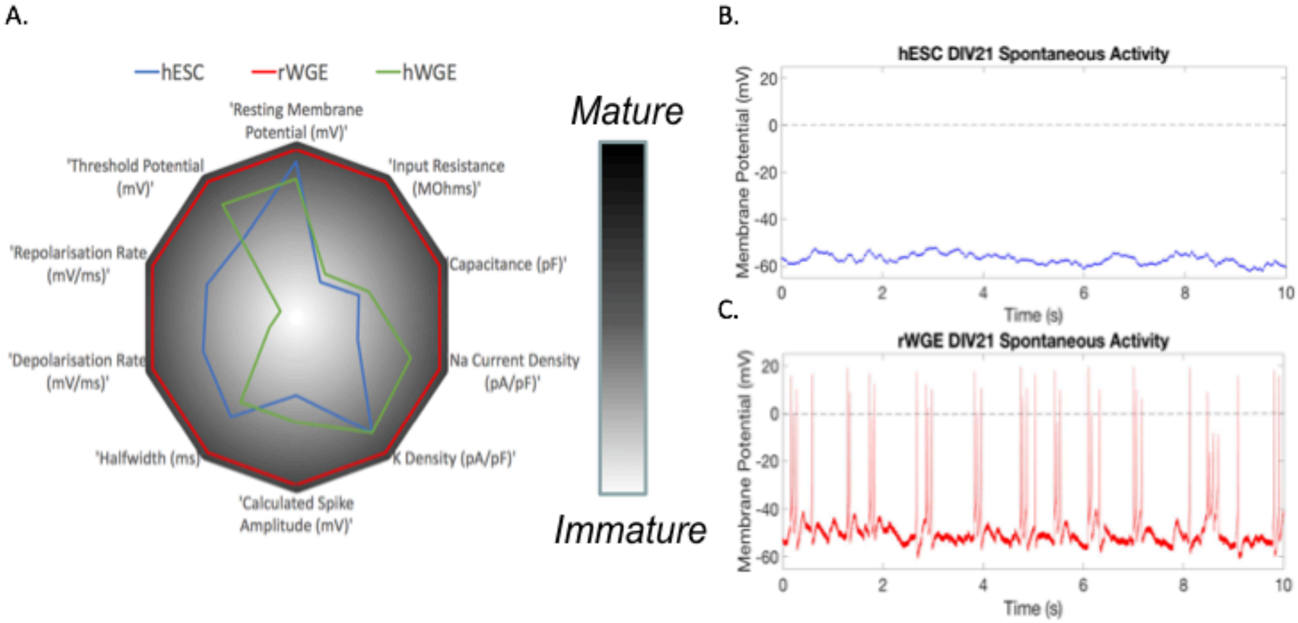

Figure 5.3: rWGE cells appear to produce MSN populations with the most mature functional properties

Basic functional properties of the neural progenitors were interrogated via whole cell patch clamp recordings at DIV21 post plating following maturation in line with the Synaptojuice protocol.

A: A polar plot of all the basic properties obtained during whole-cell patch-clamp recordings from each cell line; hESC (blue, n = 16), rWGE (red, n = 14), hWGE (green, n = 15). All properties are normalised to their peak of maturity (more negative resting membrane potential, larger capacitance, smaller halfwidth etc), the further out therefore indicating the more mature. This is also indicated by the maturity bar showing the darker regions to be more mature. SEM bars have been removed for clarity.

B: hESC exemplary recordings of spontaneous activity during whole cell patch clamp recordings in current clamp mode (I = 0).

C: rWGE exemplary recordings of spontaneous activity during whole cell patch clamp recordings in current clamp mode (I = 0).

Abbreviations, hESC: human embryonic stem cells, **rWGE:** rat whole ganglionic eminence, **hWGE:** human whole ganglionic eminence, **DIV:** days in vitro, **MSN:** medium spiny neurons

5.4.4 Bioluminescence and GFP facilitate multi-stage graft visualisation

Should transplantation therapy be translated to human subjects in the future, it would be vital to be able to visualise the graft *in vivo* at multiple stages of development. This is also vital for animal studies, in order to be able to check the growth of the graft over time and for accurate placement of recording and stimulating electrodes during recordings. To facilitate the multi-stage visualisation of the grafts during *in vitro* differentiation, *in vivo* maturation and *ex vivo* in the slices without the use of immunohistochemistry, the NPCs were transfected with luciferin and GFP. This unique approach allowed the transfected cells and slices to be visualised upon exposure to a luciferase substrate (a 'luciferin penetration formula'), whilst the animals were injected with 30 mM AkaLumine-HCL peritoneally, and imaged using a two photon microscope as described in Chapter 2. *In vivo* deep tissue bioluminescent imaging was performed according to previously published methods (Iwano et al., 2018). Bioluminescence was successfully detected *in vitro* (Fig.5.4A)*, in vivo* (Fig.5.4C) and *ex vivo* (Fig.5.4B). GFP visualisation was also successful in aiding the accurate placement of recording and stimulating electrodes in brain slices (Fig.5.4D-E). These data represent an important step in translating the work toward human studies, as deep tissue graft visualisation *in vivo* will be vital for minimally invasive evaluation of graft survival.

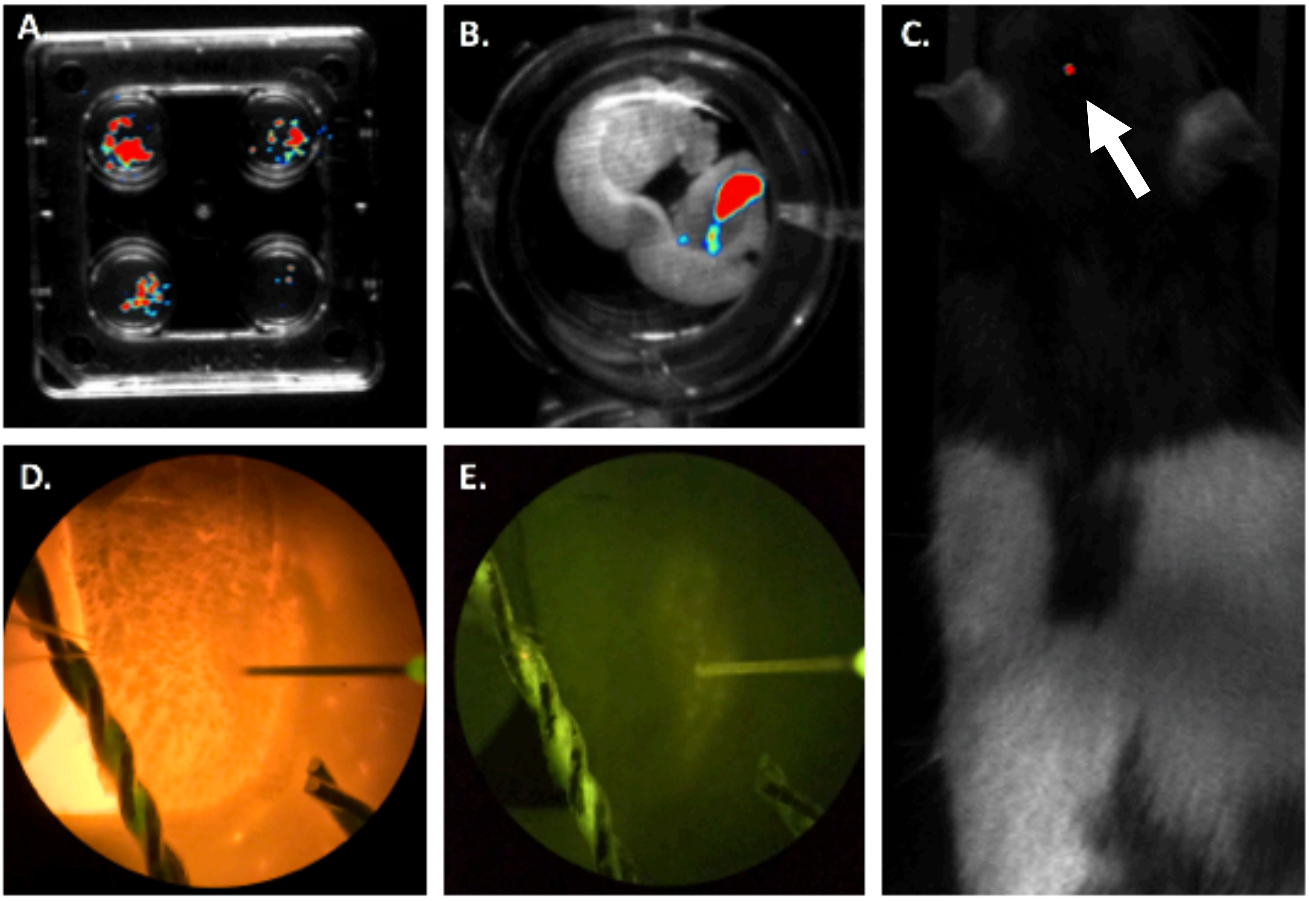

Figure 5.4: Bioluminescence and GFP transfection allow for graft visualisation *in vitro*, *in vivo* and *ex vivo*

All cells were transfected (by Dr Ngoc-Nga Vinh) with a viral construct containing both GFP and luciferase (created by Dr Amit Jathoul) to allow visualisation of the graft multiple stages of development. Bioluminescence was observed in a two-photon imager.

A: Bioluminescence in hWGE derived neuronal cells *in vitro* at DIV21 following exposure to D-Lucierfin in a cell penetration formula as described in the methods chapter of this thesis.

B: Bioluminescence in hWGE derived graft *ex vivo,* importantly only in one hemisphere in line with the grafting procedure.

C: Bioluminescence in rWGE grafted lister hooded rat, showing clearly deep tissue two-photon bioluminescence *in vivo,* further highlighted with the white arrow.

D: hESC grafted striatum in brightfield, with stimulating (right) and recording (left) electrodes. Braided silver wire was used to secure the slice for recordings.

E: hESC grafted striatum showing GFP illumination, with stimulating (right) and recording (left) electrodes. Same slice as shown in D.

Abbreviations: GFP: green fluorescent protein, **hWGE:** human whole ganglionic eminence, **rWGE:** rat whole ganglionic eminence, **hESC:** human embryonic stem cell

5.4.5 Functional integration of stem cell-derived graft within host striatum is minimal

To investigate the synaptic transmission between the graft and host, extracellular field potential recordings were performed in the engrafted animals. Extracellular field potentials were performed at various recording positions, as described in full in Chapter 2. Figure 5.1. and described briefly again below. Intrastriatal field potential recordings were taken in the hemispheres contralateral and ipsilateral to the stem cell derived grafts in order to establish baseline activity. The graft-host recordings were taken by placing the stimulating electrode in the graft and recording within the host, then swapped to achieve the host-graft recordings. The intragraft recordings were taken with both electrodes placed within the graft. The location of the graft was determined using the GFP as shown in Figure 5.4.

rWGE engrafted animals. In the rWGE (yellow, Figure 5.5A) engrafted animals, the contralateral (-0.74 +/- 0.07 mV, n = 16) and ipsilateral (-0.67 +/- 0.14 mV, n = 16) intrastriatal recordings were not significantly different ($p > 0.05$). The graft-host (-0.07 +/- 0.02 mV, n = 14), intragraft (-0.07 +/- 0.02 mV, n = 14) and host-graft (-0.07 +/- 0.02 mV, n = 14) recordings were also insignificantly different from each other ($p > 0.05$). The hashtag (#) i shows that both contralateral ($p < 0.01$, $p < 0.01$, $p < 0.01$, respectively) and ipsilateral ($p < 0.01$, $p < 0.01$, $p < 0.01$, respectively) intrastriatal peak amplitudes were significantly different from each of the three other recordings.

hESC engrafted animals. In the hESC (green, Figure 5.5B) engrafted animals, the contralateral (-0.73 +/- 0.08 mV, n = 21) and ipsilateral (-1.31 +/- 0.34 mV, n = 21) intrastriatal recordings were shown to be significantly different ($p < 0.01$). The graft-host (-0.07 +/- 0.01 mV, n = 18), intragraft (-0.17 +/- 0.07 mV, n = 18) and host-graft (-0.09 +/- 0.02 mV, n = 18) recordings were not significantly different from each other ($p > 0.05$). Not shown due to space constraints, *post hoc Bonferoni corrected t-test* analyses also revealed that the contralateral ($p < 0.01$, $p < 0.01$, $p < 0.01$ respectively) and ipsilateral ($p < 0.01$, $p < 0.01$, $p < 0.01$ respectively) intrastriatal peak amplitudes were also significantly different from each in the three other recordings.

hWGE engrafted animals. In the hWGE (purple, Figure 5.5C) engrafted animals the contralateral (-0.82 +/- 0.09 mV, n = 18) and ipsilateral (-0.79 +/- 0.08 mV, n = 18) intrastriatal recordings were not significantly different ($p > 0.05$). The graft-host (-0.11 +/- 0.01 mV, n = 13), intragraft (-0.12 +/- 0.01 mV, n = 13) and host-graft (-0.11 +/- 0.03 mV, n = 13) recordings were not significantly different from each other ($p > 0.05$). The hashtag (#) indicates that both contralateral ($p < 0.01$, $p < 0.01$, $p < 0.01$, respectively) and ipsilateral ($p < 0.01$, $p < 0.01$, $p < 0.01$, respectively) intrastriatal peak amplitudes were significantly different from each of the three other recordings.

Shown in Figure 5.5, normal fEPSPs were seen contralaterally, in all experimental groups, whilst no synaptic transmission was seen between the graft and the ipsilateral host striatum. Importantly, normal fEPSPs were seen in the remaining striatum ipsilaterally. Interestingly, a small presynaptic response was occasionally seen intragraft.

Taken together, these data suggest the slices are healthy and alive, as indicated by healthy fEPSPs contralaterally and in the remaining ipsilateral striatum. However, functional integration appears to be severely limited which implies either that the grafts do not survive to the time point at which recordings were taken (22 weeks post transplantation +/- 2 weeks) or that the grafts do not functionally integrate with the host striatum.

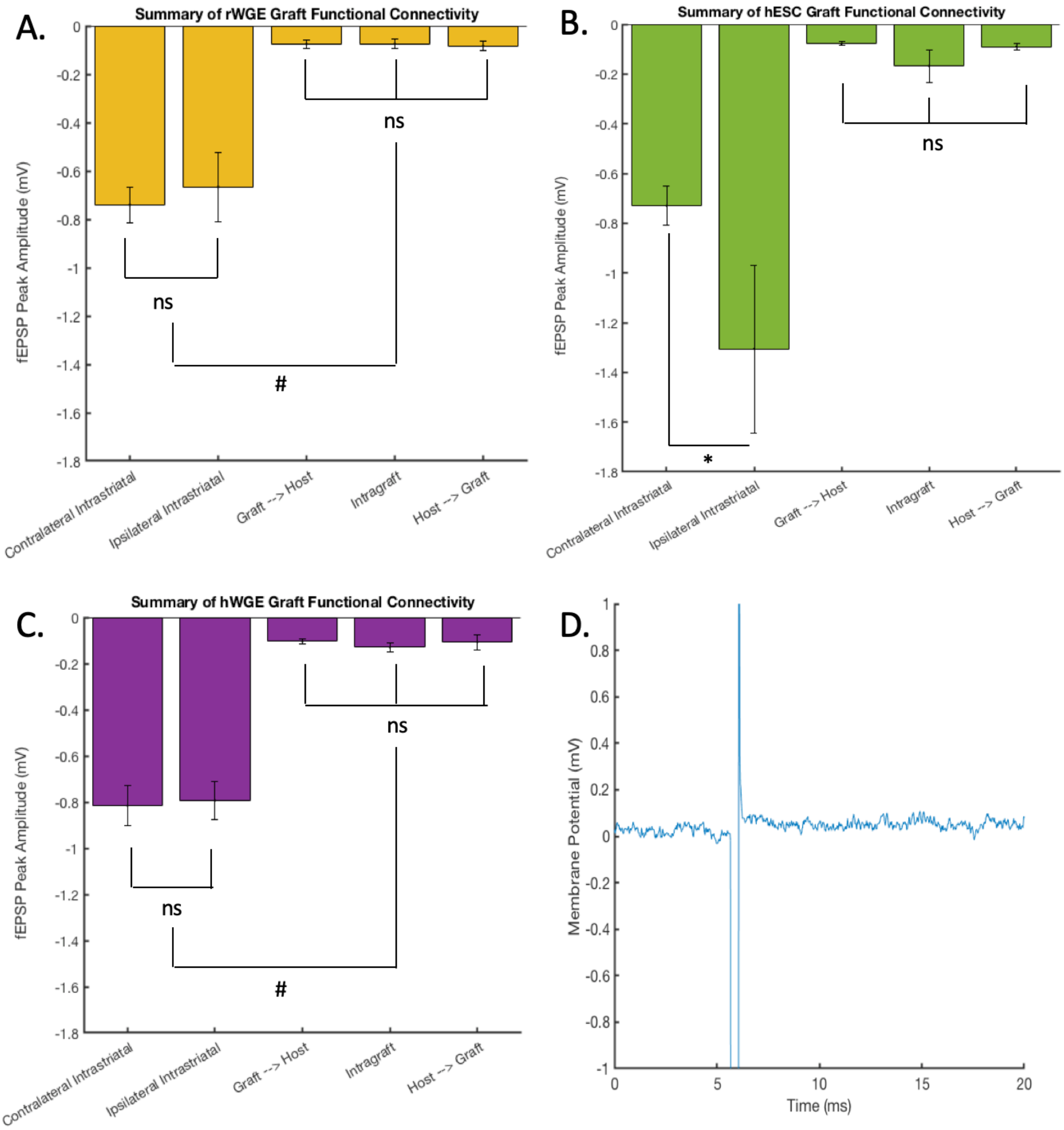

Figure 5.5: Little to no functional integration of graft and host striatum
Extracellular field potential recordings were performed in coronal slices at various recording positions as described in full in Chapter 2. Figure 1, to generate the fEPSP peak amplitude values shown here.
A: Summary of the fEPSP peak amplitude values at various recordings positions in rWGE grafted striatum (yellow). The hashtag (#) is denoted to show that both contralateral and ipsilateral intrastriatal peak amplitudes were significantly different from each of the three other recordings ($p < 0.01$ each)
B: Summary of the fEPSP peak amplitude values at various recordings positions in hESC grafted striatum (green). The contralateral and ipsilateral intrastriatal peak amplitudes were shown to be significantly different from each other ($p < 0.05$). The peak amplitudes of the other three recordings were shown to be statistically indifferent ($p = 1$) from eachother. The contralateral intrastriatal response was significantly different from each of the three recordings ($p < 0.05$, $p < 0.05$, $p < 0.05$ respectively, not shown due to space restrictions), as was the ipsilateral response ($p < 0.01$, $p < 0.01$, $p < 0.01$ respectively, also not shown).
C: Summary of the fEPSP peak amplitude values at various recordings positions in hWGE grafted striatum (purple). The hashtag (#) is denoted to show that both contralateral and ipsilateral intrastriatal peak amplitudes were significantly different from each of the three other recordings ($p < 0.01$ each)
D: The bottom right panel shows an exemplary trace from a rWGE host → graft recording. Visible is the stimulus artifact, but a lack of presynaptic afferent volley or post-synaptic field potential.
Data shown throughout, except in the exemplary recording, as mean values +/- SEM. $p^* < 0.05$. n defined in text.
Abbreviations: rWGE: rat whole ganglionic eminence **hESC:** human embryonic stem cells, **hWGE:** human whole ganglionic eminence, **fEPSP:** rat whole ganglionic eminence

5.4.6 Stem cell derived grafts restore ipsilateral intrastriatal synaptic communication

To examine whether the grafts were able to produce a beneficial effect without functional integration, the healthy contralateral responses were grouped and then the ipsilateral intrastriatal responses from each of the groups (rWGE not shown) were plotted and analysed by ANOVA, Bonferroni post-hoc tests..

In Figure 5.6A the mean input/output curves demonstrate that fEPSPs have smaller peak amplitudes intrastriatally in the ipsilateral lesioned hemisphere (red), than those of the grouped contralateral striatum; the group described as healthy (blue). The ipsilateral field potentials were completely restored in rWGE (yellow) and hWGE (purple) engrafted animals, and increased in hESC engrafted animals (green). The peak amplitudes from each group were then plotted and compared (Figure 5.6C). The ipsilateral fEPSP peak amplitude in lesioned animals (-0.23 +/- 0.03 mV, n = 8) was significantly smaller than the grouped contralateral fEPSP peak amplitude, termed healthy, (-0.75 +/ 0.05 mV, n = 57, $p < 0.05$). The ipsilateral intrastriatal fEPSP peak amplitude in hWGE grafted animals (-0.79 +/- 0.08 mV, n = 18) was not significantly different from that seen in the healthy striatum ($p > 0.05$). The ipsilateral intrastriatal fEPSP peak amplitude in hESC engrafted animals (-1.31 +/- 0.34 mV, n = 21) was significantly higher than the ipsilateral response seen in hWGE grafted ($p < 0.05$), lesioned ($p < 0.001$) and healthy striatum ($p < 0.05$). The ipsilateral hWGE engrafted response was not significantly different from either the lesioned hemisphere ($p > 0.05$), the healthy ($p > 0.05$) or the rWGE engrafted striatum ($p > 0.05$), but smaller than the hESC engrafted striatum ($p < 0.05$).

Figure 5.6B shows the input/output curves when normalized to their respective maximal amplitude, revealing few differences. Figure 5.6D then shows the half maximal value from each group, taken as the stimulus intensity required to reach 50% maximal fEPSP peak amplitude. This can be seen as a rudimentary measure of how much stimulus is required to evoke a response. One-way ANOVA revealed no significant differences between the means of each group; Healthy (33.16 +/- 1.76 V, n = 57), Lesioned (30.07 +/- 15.31 V, n = 8), rWGE engrafted (30.61 +/- 3.22 V, n = 16), hWGE engrafted (29.94 +/- 5.56 V, n = 18) and hESC engrafted (19.95 +/-2.27 V, n = 21, p = 0.2012).

Thus, the fEPSPs were restored in all stem cell engrafted hemispheres and, in the case of hESCs, improved significantly. This implies the graft does in fact have a beneficial effect on the health of the ipsilateral striatum despite a lack of functional integration by an as yet unknown mechanism.

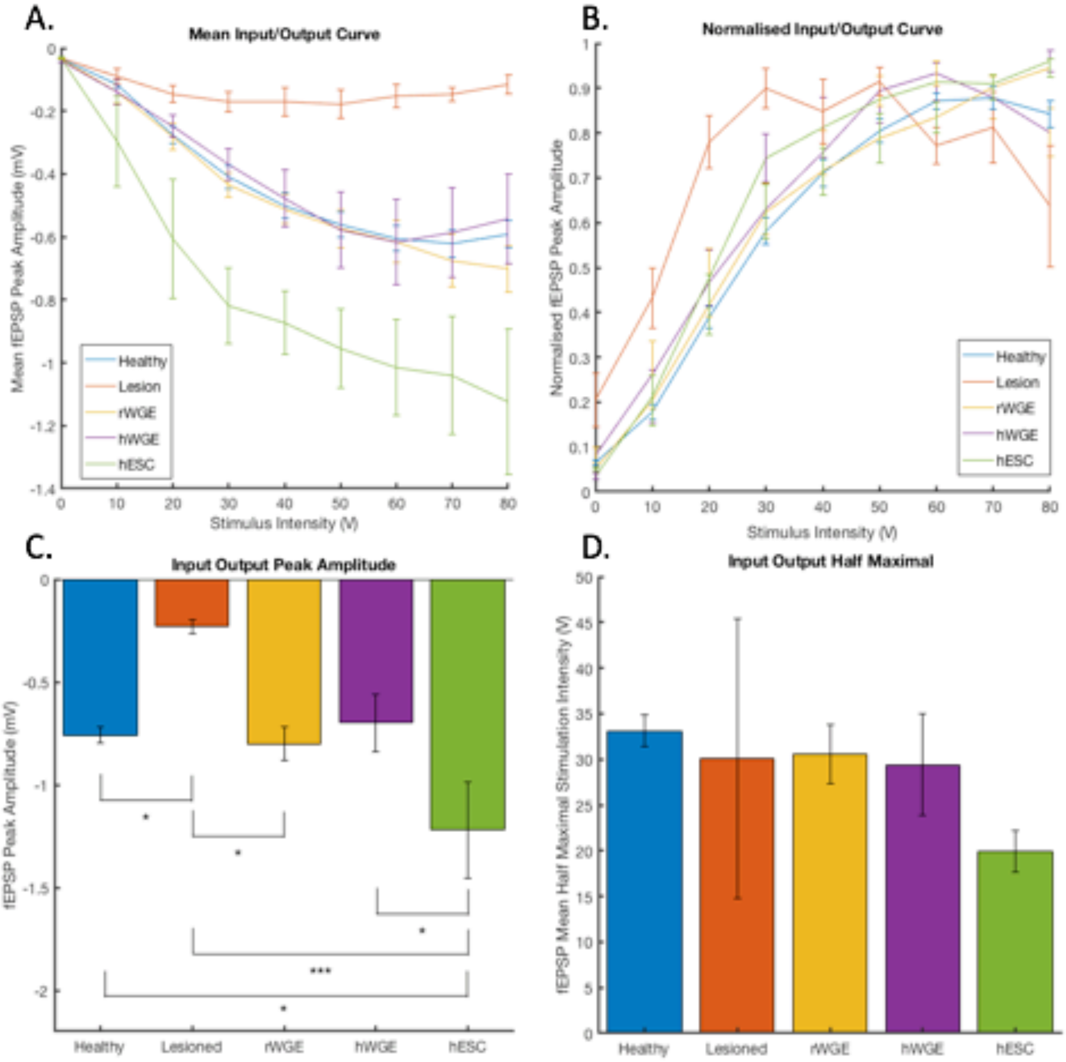

Figure 5.6: Increased Ipsilateral Intrastriatal fEPSP Peak Amplitude in hESC grafted striatum

Extracellular field potential recordings were performed in coronal slices at various recording positions as described in full in Chapter 2. Figure 1, to generate the fEPSP peak amplitude, and input output curves shown here. Input/Output curves were generated by sequentially increasing the stimulus strength from 0 V to 80 V and recording the fEPSP peak amplitude at each intensity.

A: Mean input output curves showing the response in the ipsilateral lesioned hemisphere (red), the grouped contralateral striatum termed healthy (blue), rWGE grafted hemispheres (yellow) hWGE grafted hemispheres (purple) and in hESC grafted animals (green).

B: Mean input output curves, normalized to the maximal value from each group, showing the response in the ipsilateral lesioned hemisphere (red), the grouped contralateral striatum termed healthy (blue), rWGE grafted hemispheres (yellow) hWGE grafted hemispheres (purple) and in hESC grafted animals (green).

C: Mean fEPSP peak amplitude from the ipsilateral lesioned hemisphere (red), the grouped contralateral striatum termed healthy (blue), rWGE grafted hemispheres (yellow) hWGE grafted hemispheres (purple) and in hESC grafted animals (green).

D: Mean half maximal value from each group, taken as the stimulus intensity required to reach 50% maximal fEPSP peak amplitude. The ipsilateral lesioned hemisphere (red), the grouped contralateral striatum termed healthy (blue), rWGE grafted hemispheres (yellow) hWGE grafted hemispheres (purple) and in hESC grafted animals (green) are shown.

Data shown throughout, except in the exemplary recording, as mean values +/- SEM. p* <0.05, p*** < 0.001. n defined in text.

Abbreviations: hESC: human embryonic stem cell**, hWGE:** human whole ganglionic eminence**, fEPSP:** field excitatory post synaptic potential

5.5 Discussion & Conclusion

5.5.1 Lack of functional integration

Existing electrophysiological data to support functional stem cell derived graft-host striatum connections is limited, despite the wealth of literature surrounding foetal (McBride et al., 2004; Ryu et al., 2004) and embryonic (Campbell et al., 1993; Döbrössy and Dunnett, 2006; Aubry et al., 2008; Ma et al., 2012; Reidling et al., 2018) grafts into HD animal models. Several studies have suggested functional integration, but few are based on electrophysiological studies. Through extensive use of immunohistochemical staining, Ma *et al.* suggested hESC derived grafts received both glutamatergic and dopaminergic inputs (Ma et al., 2012). Whilst a highly valid experimental approach, the presence of protein markers support the presence of synapses but cannot be seen as definitive proof of synaptic functionality. Gaura *et al.,* reported seeing increased cortical metabolism through the use of FDG-positron enhanced tomography in human subjects following bilateral foetal grafts (Gaura et al., 2004). Similarly, this cannot be taken as proof of functional electrochemical corticostriatal connectivity.

One paper did examine the electrophysiological connectivity of foetal grafts in a lesion rodent model of Huntington's Disease. In this paper, Mazzochi-Jones *et al*., reported bidirectional electrophysiological connectivity between the engrafted foetal cells and the lesioned host striatum (Mazzocchi-Jones et al., 2009). This finding is in direct contrast to the fidnings in this report; that there is no functional electrochemical connectivity. Mazzochi-Jones *et al*., used mice in their experiments compared to the experiments performed in rats shown here. Furthermore, a slightly different recording was performed as Mazzochi-Jones was investigating the coritco-striatal pathways, yet these differences combined are not expected make such a confounding difference. However, the timeline of the experiments and the age of the animals is not clear, which could make a very large difference. It is clearly referenced that the animals were grafted 7 days post lesion surgery, yet the time between transplantation surgery and electrophysiological recordings is not specified. The graft-host electrophysiological recordings presented here were performed in 9 month old animals at 22 weeks post transplantation. Perhaps the grafts simply didn't survive as long as 22 weeks *in vivo,* making recordings of functional connections not only technically challenging but essentially impossible.

This observation of poor graft survival is supported in the literature. Reidling *et al.,* noted that at four weeks post transplantation graft survival had already dropped to 41 %, falling further to roughly 25 % six months post transplantation (Reidling et al., 2018), and could also be a contributing factor in this project.. The very low intragraft fEPSP peak amplitudes (Fig.4) and the poor level of spontaneous activity seen in hESC/hWGE cultures at DIV21 (Fig.3) further support the notion that the graft health may be low. However, that the rWGE derived MSNs produced fully spontaneous action potentials *in vitro* suggests these neurons at least had the potential to mature into fully functional MSNs *in vivo.* Furthermore, the presence of bioluminescent signals *in vivo* and *ex vivo* (Fig.3) suggest the grafts are indeed alive as the enzymatic reactions required to produce bioluminescence could not occur within dead cells. Therefore, it seems sensible to assume that engrafted material was alive at the time of the experimentation but suggest that they had differentiated poorly into functionally active neurons *in vivo*. Immunohistochemical studies on these slices could clarify whether the cells at least expressed the relevant markers of mature MSNs such as DARP32 and did not express markers of pluripotency, such as Oct-4 and Nanog.

One previous study has reported whole-cell patch-clamp recordings of hESC-derived MSNs transplanted into a rodent HTT fragment model of HD, reporting spontaneous post-synaptic currents (Reidling et al., 2018). Spontaneous post-synaptic currents being indicative of synaptic connections from other neurons being registered on grafted cells. However, it cannot be concluded definitively that this is communication with host neurons and not exclusively communication from other engrafted cells. This is indeed a problem that would have been faced had this project uncovered synaptic communication between the engrafted cells and the host. Despite the nature of recordings performed in this project (selectively stimulating in the graft and recording in the host, and *vice versa*) this would still not have been definitive. The best way to confirm definitively host-graft connectivity would incorporate the use of channel rhodopsins. If the engrafted cells were also transfected with a channel rhodopsin sensitive to blue light, subsequent exposure to blue light post transplantation and recording in the host striatum would definitively confirm whether the engrafted cells functionally innervate the host striatum as cells do not natively respond to blue light. Liske *et al.,* recently utilised a single channel rhodopsin capable of stimulating and inhibiting neuronal firing (Liske et al., 2013), and would be suitable for use in future transplantation experiments.

5.5.2 Beneficial effect of stem cell derived graft despite functional integration

Numerous stem cell transplantation studies have described beneficial effects in behaviour and learning tests, both in animal models of HD (Campbell et al., 1993; McBride et al., 2004; Ryu et al., 2004; Döbrössy and Dunnett, 2006; Aubry et al., 2008; Reidling et al., 2018) and human HD patients (Bachoud-Lévi et al., 2000; Gaura et al., 2004; Reuter et al., 2008). Indeed, unpublished work, conducted by Dr Ana Garcia Aguirre, on these same animals prior to electrophysiological interrogation (not included in this thesis) support these claims by suggesting behavioural improvements in all of the grafted experimental groups. Thus, it seems beyond doubt that stem cell derived grafts do indeed confer a beneficial effect in this animal model of HD. However the mechanism by which this occurs remains elusive.

The first, and perhaps most logical hypothesis, is beneficial effect via electrophysiological integration. As discussed previously, there have been limited studies conclusively reporting electrophysiological integration of stem cell derived grafts. This is supported further by the findings presented in this thesis, suggesting that minimal to no functional integration (Fig.5.5). Therefore, it is unlikely the beneficial mechanism is via electrophysiological interrogation; however this cannot be disproved completely without future channel rhodopsin experiments. Interestingly, a benefit can be detected electrophysiologically as shown in this thesis via restoring ipsilateral intrastriatal field potentials (Fig.6). Reidling *et al.,* also demonstrated an electrophysiological benefit by suggesting that the hyperexcitability of the host striatum was reduced when grafted with hESC derived grafts (Reidling et al., 2018). Direct comparisons are difficult to draw between the Reidling study and the work in this thesis due to the use of different animal models. Reidling *et al.,* used the transgenic R6/2 fragment model of HD, whereby the animals express exon 1 of the human HD gene with an expanded CAG repeat first established by Mangiarini *et al.,* (1996). Hyperexcitability has been demonstrated in these animals through a possible impairment of excitatory corticostriatal glutamatergic pathways (Cepeda et al., 2003) and GABAergic inhibitory pathways (Cummings et al., 2009). As the excitotoxic QA model of HD used in this thesis only damages the striatum and does not possess any mutant huntingtin, corticostriatal pathways were not considered. Experimentally it also proved impossible to interrogate the corticostriatal pathways due to the vastly extended age of these animals compared to other groups and the ongoing effects of synaptic pruning. Corticostriatal pathways undoubtedly still existed in these animals but the number of the pathways would have decreased significantly over time making the likelihood of interrogation via extracellular field potential recordings close to impossible.

Another potential theory could simply be through mechanical support, whereby the graft occupies the space that the cells have lost during model progression thus preventing the further collapse within the striatum. Whilst this is likely a contributing factor, it is unlikely the only factor due to the benefit being seen electrophysiologically in this thesis and by Reidling *et al.* The work conducted by Campbell *et al.,* (Campbell et al., 1993) suggesting graft specific release of GABA as a result of host derived afferent activity, also do not support a solely mechanical hypothesis.

A further hypothesis for the mechanism behind the beneficial effect of neural transplantation is via the release of neurotrophic factors, such as (BDNF). First isolated by Barde et al. (1982), BDNF has been shown to have roles in neuronal growth, survival and function (see reviews by Chao (2003) and Binder & Scharfman (2004) for details) as well as memory and learning. BDNF has been suggested to play roles in synapse formation through disruption of cadherin-β-catenin complexes (Bamji et al., 2006) and axonal outgrowth (Blurton-Jones et al., 2009), processes thought to be central to learning and memory. Furthermore, hippocampus specific knock-down of BDNF significantly impairs cognitive function in a lentiviral Cre recombinase deletion of the BDNF gene in otherwise wild type adult mice (Heldt et al., 2007), suggestive of BDNF’s key role in cognition. As cognitive decline is also a feature of HD as it is of AD, the role of BDNF in HD must be further examined. HD patients often present with reduced levels of BDNF (Ferrer et al., 2000; Zuccato et al., 2001, 2011) likely as a consequence of decreased BDNF transcriptional activation (Zuccato et al., 2001) as well as transport from the cortex to the striatum (Gauthier et al., 2004). This reduction in BDNF is also mirrored in animal models of HD (Spires et al., 2004; Gharami et al., 2008), prompting therapies aimed at increasing

BDNF levels. In an AD animal model cognitive performance was fully restored following transplant of stem cells overexpressing BDNF (Wu et al., 2016). Interestingly, the overexpression of BDNF in this study was also suggested to aid functional integration with “existing neuronal networks”. In HD animal model studies, increased BDNF levels have also been seen in transplant therapies of stem cell derived grafts not overexpressing BDNF (Blurton-Jones et al., 2009; Reidling et al., 2018), with functional improvements seen in both cases. Recently, Zimmerman *et al.,* took the step to combine BDNF therapy with neural cell replacement therapy by transplanting ESC-derived neural progenitor cells that have been programmed to overexpress BDNF resulting in restoration of motor function across three different animal models of HD. Taken together, the existing literature and the results presented in this thesis strongly support the hypothesis that the graft may have a beneficial effect through release of secretory vesicles and neurotrophic factors.

5.5.3 QA lesioned model and combined therapies

Direct comparisons between studies is difficult due, in part, to the range of different models of HD. In this study, the QA lesion rat model was used. The QA acid lesion HD model has been widely adopted due to the excitotoxicity of QA (Schwarcz and Köhler, 1983; Tavares et al., 2000, 2002), damage to MSN populations (Schwarcz and Köhler, 1983) and mimicry of the classical HD phenotype (Beal et al., 1991). The increased levels of QA in early HD patients (Guidetti et al., 2004) lends further credibility to the use of QA lesions to model HD. However, the QA lesion model lacks perhaps the most common hallmark of HD; mutant huntingtin aggregates. For this reason the QA lesion model does not fully recapitulate HD. Therefore, the results from this study need to be considered within the constraints of the model itself. Shown here, stem cell-derived grafts can restore synaptic communication intrastriatally following excitotoxic damage in the striatum, excitotoxic damage being one possible cause of the cell death seen in HD. To claim that stem-derived grafts can provide functional electrophysiological benefits in HD, the impact of mutant huntingtin aggregates in graft experiments on electrophysiological properties needs to be examined. The mutant huntingtin may damage the graft in the same way that the native cells are damaged, either preventing graft success at all or severely shortening lifespan. As described earlier, previous graft experiments conducted in HD models containing the genetic mutation for HD, and therefore the toxic aggregates, have included little electrophysiological interrogation.

An alternative approach to HD therapy is to reduce the build-up of mutant huntingtin in the hope of preventing or slowing damage to the brain. Significant progress has been made in reducing the huntingtin aggregates, largely through the use of antisense oligonucleotide (ASO) therapy (Carroll et al., 2011; Kordasiewicz et al., 2012; Stanek et al., 2013; Østergaard et al., 2013; Evers et al., 2014; Skotte et al., 2014; Southwell et al., 2014; Rué et al., 2016). ASOs are short singular strands of ribonucleic acid (RNA) that facilitate the degradation of complementary target sequences of messenger RNA (mRNA) preventing the translation of mRNA into protein. ASO therapy has been shown in mice fragment models of HD to reduce huntingtin mRNA levels (Carroll et al., 2011; Kordasiewicz et al., 2012; Stanek et al., 2013; Østergaard et al., 2013; Evers et al., 2014; Skotte et al., 2014; Southwell et al., 2014; Rué et al., 2016) and subsequently improve both psychological parameters (Stanek et al., 2013) and motor function (Kordasiewicz et al., 2012; Stanek et al., 2013; Rué et al., 2016). These studies have culminated in a recent phase three clinical trial that reported success in reducing circulated CSF huntingtin levels in a dose dependant manner (Tabrizi et al., 2018), subsequently gaining significant media attention (Devlin, 2017; Gallagher, 2017; New Scientist, 2017).

Whilst a promising step towards an effective therapy for HD patients, the therapy would only be effective at preventing damage either taking place or progressing. ASO therapy would not be able to reverse disease progression and treat the underlying cell loss, for this a cell replacement therapy will be required. A more long-term solution may be to utilise a cell replacement therapy to treat the cell loss in conjunction with an ASO therapy to reduce mutant huntingtin levels, in turn enhancing the lifespan of the graft and the overall benefit to the patient. Using stem cell-derived grafts appears a promising avenue for the cell replacement but is associated with a host of ethical problems related to the source of the stem cells and practical issues such as the possibility of immune rejection. Using patient derived stem cells and autografting them could alleviate the immune rejection possibility and a lot of the ethical concerns surrounding embryonic stem cells. Using the patient's own stem cells does present two further problems; 1) the patient has a limited source of adult stem cells and 2) these stem cells will still contain the mutation giving rise to HD in the first place.

Clustered repeated interspersed palindromic repeats and associated systems (CRISPR/Cas9) have the ability to edit the genome at any desired sequence and have recently been used to correct the HD mutation (Shin et al., 2016) in patient fibroblasts. The versatility of CRISPR/Cas9 is highlighted further by Black *et al.,* who managed the direct conversion of human fibroblasts into neuronal cells (Black et al., 2016). Utilising these two methods could allow for the generation of HD corrected neuronal cells from patient fibroblasts, therefore providing a near limitless source of iPS cells that have few ethical issues associated with them and have little to no risk of immune rejection following transplantation. Combining this hypothetical CRISPR/Cas9 based cell replacement therapy with the promising ASO huntingtin lowering techniques may finally be a step toward a long lasting and effective therapy for HD.

Chapter 6 – General discussion and concluding remarks

6.1 MATLAB based analysis for large complex datasets

The use of MATLAB has been invaluable in analysing the large complex datasets associated with neurophysiological experiments. Not only has MATLAB expedited the whole procedure of analysis, but it has made the process documented and repeatable. Methodology sections of published papers and articles are lengthy and meticulously detailed. However, they rarely fully explain how the data were actually analysed. Commonly, researchers world-wide will have Excel spreadsheets that manipulate the data in numerous ways which are rarely described in the Methods section. In the interest of academic honesty and integrity it is highly recommended that the precise mechanics of the data analysis and interpretation are made transparent. Doing so will also enable academics at other institutions to analyse data in the exact same way and increase the comparability of the results. As discussed in Chapter 3, MATLAB can be intimidating to those who have not used the tool before-hand. However, every effort has been made to make learning the language more user friendly. The benefits of doing so cannot be stressed enough. However, it is important to note that many other programming languages exist, such as Python, C++ and Java each of which has their own respective merits.

6.2 Stem cells in disease modelling and therapy

Stem cells have the captivating ability to turn into any type of cell within the human body, thus their enormous potential for disease modelling and therapy. There are large ethical concerns associated with embryonic stem cells, whereas induced pluripotent stem cells demand technical prowess. Stem cells have been used throughout both arms of this project successfully to not only model a ‘difficult to model’ neurological disease, CDKL5 deficiency, but also to provide therapeutic benefit in a neurodegenerative disease associated with vast amounts of cell loss. It is for these reasons that the positives significantly outweigh the negatives associated with stem cell research and therapy, and stem cells will likely continue to be used in both for decades to come to great effect. The advent of CRISPR/Cas9 based genetic engineering and the rapid advancements in genetic medicine have the potential revolutionise medicine, but not without the help of stem cell technologies in testing of the techniques.

6.3 Electrophysiology in neurological disease research

Underpinning all of the work conducted in this thesis is electrophysiology. Electrophysiology remains the best way of interrogating the functional properties of neurons. As invaluable as techniques such as immunohistochemistry and molecular biological approaches are, electrophysiology remains the only way to determine whether the cell is electrochemically active. Immunohistochemistry can tell you that a cell has the right markers to be active, and high-powered microscopy can tell you whether the cells morphology would be conducive to electrical activity - yet only electrophysiology can explicitly define whether a cell is electrochemically active and how. The ideal project would utilise electrophysiology in conjunction with other techniques such as immunohistochemistry, microscopy and calcium imaging to answer strictly defined questions in a multi-disciplinary and comprehensive manner.

Reference List

Amendola E, Zhan Y, Mattucci C, Castroflorio E, Calcagno E, Fuchs C, Lonetti G, Silingardi D, Vyssotski AL, Farley D, Ciani E, Pizzorusso T, Giustetto M, Gross CT (2014) Mapping Pathological Phenotypes in a Mouse Model of CDKL5 Disorder. PLOS ONE 9:e91613.

Arber C, Precious SV, Cambray S, Risner-Janiczek JR, Kelly C, Noakes Z, Fjodorova M, Heuer A, Ungless MA, Rodríguez TA, Rosser AE, Dunnett SB, Li M (2015) Activin A directs striatal projection neuron differentiation of human pluripotent stem cells. Dev Camb Engl 142:1375–1386.

Aubry L, Bugi A, Lefort N, Rousseau F, Peschanski M, Perrier AL (2008) Striatal progenitors derived from human ES cells mature into DARPP32 neurons in vitro and in quinolinic acid-lesioned rats. Proc Natl Acad Sci 105:16707–16712.

Bachoud-Lévi A-C et al. (2000) Motor and cognitive improvements in patients with Huntington's disease after neural transplantation. The Lancet 356:1975–1979.

Bahi-Buisson N, Bienvenu T (2011) CDKL5-Related Disorders: From Clinical Description to Molecular Genetics. Mol Syndromol 2:137–152.

Bamji SX, Rico B, Kimes N, Reichardt LF (2006) BDNF mobilizes synaptic vesicles and enhances synapse formation by disrupting cadherin–β-catenin interactions. J Cell Biol 174:289–299.

Barde YA, Edgar D, Thoenen H (1982) Purification of a new neurotrophic factor from mammalian brain. EMBO J 1:549–553.

Barnes RM, Firulli BA, Conway SJ, Vincentz JW, Firulli AB (2010) Analysis of the Hand1 cell lineage reveals novel contributions to cardiovascular, neural crest, extra-embryonic, and lateral mesoderm derivatives. Dev Dyn Off Publ Am Assoc Anat 239:3086–3097.

Beal MF, Ferrante RJ, Swartz KJ, Kowall NW (1991) Chronic quinolinic acid lesions in rats closely resemble Huntington's disease. J Neurosci Off J Soc Neurosci 11:1649–1659.

Bean BP (2007) The action potential in mammalian central neurons. Nat Rev Neurosci 8:451.

Bear MF, Connors BW, Paradiso MA (2001) Neuroscience, 2nd ed. Philadelphia, USA: Sinauer Associates.

Binder DK, Scharfman HE (2004) Mini Review. Growth Factors 22:123–131.

Black JB, Adler AF, Wang H-G, D'Ippolito AM, Hutchinson HA, Reddy TE, Pitt GS, Leong KW, Gersbach CA (2016) Targeted Epigenetic Remodeling of Endogenous Loci by CRISPR/Cas9-Based Transcriptional Activators Directly Converts Fibroblasts to Neuronal Cells. Cell Stem Cell 19:406–414.

Blurton-Jones M, Kitazawa M, Martinez-Coria H, Castello NA, Müller F-J, Loring JF, Yamasaki TR, Poon WW, Green KN, LaFerla FM (2009) Neural stem cells improve cognition via BDNF in a transgenic model of Alzheimer disease. Proc Natl Acad Sci U S A 106:13594–13599.

Bostock H, Cikurel K, Burke D (1998) Threshold tracking techniques in the study of human peripheral nerve. Muscle Nerve 21:137–158.

Boulting GL, Kiskinis E, Croft GF, Amoroso MW, Oakley DH, Wainger BJ, Williams DJ, Kahler DJ, Yamaki M, Davidow L, Rodolfa CT, Dimos JT, Mikkilineni S, MacDermott AB, Woolf CJ, Henderson CE, Wichterle H, Eggan K (2011) A functionally characterized test set of human induced pluripotent stem cells. Nat Biotechnol 29:279–286.

Boyer LA, Lee TI, Cole MF, Johnstone SE, Levine SS, Zucker JP, Guenther MG, Kumar RM, Murray HL, Jenner RG, Gifford DK, Melton DA, Jaenisch R, Young RA (2005) Core Transcriptional Regulatory Circuitry in Human Embryonic Stem Cells. Cell 122:947–956.

Boyer PD, Walker JE, Skou JC (1997) The Nobel Prize in Chemistry 1997. Available at: https://www.nobelprize.org/nobel_prizes/chemistry/laureates/1997/index.html [Accessed July 9, 2018].

Boyle J (2008) Molecular biology of the cell, 5th edition by B. Alberts, A. Johnson, J. Lewis, M. Raff, K. Roberts, and P. Walter. Biochem Mol Biol Educ 36:317–318.

Calabresi P, Pisani A, Mercuri NB, Bernardi G (1992) Long-term Potentiation in the Striatum is Unmasked by Removing the Voltage-dependent Magnesium Block of NMDA Receptor Channels. Eur J Neurosci 4:929–935.

Campbell K, Kalén P, Wictorin K, Lundberg C, Mandel RJ, Björklund A (1993) Characterization of gaba release from intrastriatal striatal transplants: Dependence on host-derived afferents. Neuroscience 53:403–415.

Carroll JB, Warby SC, Southwell AL, Doty CN, Greenlee S, Skotte N, Hung G, Bennett CF, Freier SM, Hayden MR (2011) Potent and selective antisense oligonucleotides targeting single-nucleotide polymorphisms in the Huntington disease gene / allele-specific silencing of mutant huntingtin. Mol Ther J Am Soc Gene Ther 19:2178–2185.

Carter RB, Wood PL, Wieland S, Hawkinson JE, Belelli D, Lambert JJ, White HS, Wolf HH, Mirsadeghi S, Tahir SH, Bolger MB, Lan NC, Gee KW (1997) Characterization of the anticonvulsant properties of ganaxolone (CCD 1042; 3alpha-hydroxy-3beta-methyl-5alpha-pregnan-20-one), a selective, high-affinity, steroid modulator of the gamma-aminobutyric acid(A) receptor. J Pharmacol Exp Ther 280:1284–1295.

Cepeda C, Hurst RS, Calvert CR, Hernández-Echeagaray E, Nguyen OK, Jocoy E, Christian LJ, Ariano MA, Levine MS (2003) Transient and progressive electrophysiological alterations in the corticostriatal pathway in a mouse model of Huntington’s disease. J Neurosci Off J Soc Neurosci 23:961–969.

Chao MV (2003) Neurotrophins and their receptors: A convergence point for many signalling pathways. Nat Rev Neurosci 4:299–309.

Chattopadhyay B, Baksi K, Mukhopadhyay S, Bhattacharyya NP (2005) Modulation of age at onset of Huntington disease patients by variations in TP53 and human caspase activated DNase (hCAD) genes. Neurosci Lett 374:81–86.

Chen EY, DeRan MT, Ignatius MS, Grandinetti KB, Clagg R, McCarthy KM, Lobbardi RM, Brockmann J, Keller C, Wu X, Langenau DM (2014) Glycogen synthase kinase 3 inhibitors induce the canonical WNT/β-catenin pathway to suppress growth and self-renewal in embryonal rhabdomyosarcoma. Proc Natl Acad Sci U S A 111:5349–5354.

Chen Q, Zhu Y-C, Yu J, Miao S, Zheng J, Xu L, Zhou Y, Li D, Zhang C, Tao J, Xiong Z-Q (2010a) CDKL5, a protein associated with rett syndrome, regulates neuronal morphogenesis via Rac1 signaling. J Neurosci Off J Soc Neurosci 30:12777–12786.

Chen Q, Zhu Y-C, Yu J, Miao S, Zheng J, Xu L, Zhou Y, Li D, Zhang C, Tao J, Xiong Z-Q (2010b) CDKL5, a Protein Associated with Rett Syndrome, Regulates Neuronal Morphogenesis via Rac1 Signaling. J Neurosci 30:12777–12786.

Cheung AYL, Horvath LM, Grafodatskaya D, Pasceri P, Weksberg R, Hotta A, Carrel L, Ellis J (2011) Isolation of MECP2-null Rett Syndrome patient hiPS cells and isogenic controls through X-chromosome inactivation. Hum Mol Genet 20:2103–2115.

Chiou J (2014) Flexible and Fast Spike Raster Plotting - File Exchange - MATLAB Central. Available at: https://uk.mathworks.com/matlabcentral/fileexchange/45671 [Accessed September 24, 2018].

ClinicalTrials.gov (2015) A Multicenter, Open-Label Proof-of-Concept Trial of Ganaxolone in Children With PCDH19 Female Pediatric Epilepsy and Other Rare Genetic Epilepsies - Full Text View - ClinicalTrials.gov. Available at: https://clinicaltrials.gov/ct2/show/NCT02358538 [Accessed June 10, 2018].

Craufurd D, Thompson JC, Snowden JS (2001) Behavioral changes in Huntington Disease. Neuropsychiatry Neuropsychol Behav Neurol 14:219–226.

Cummings DM, André VM, Uzgil BO, Gee SM, Fisher YE, Cepeda C, Levine MS (2009) Alterations in cortical excitation and inhibition in genetic mouse models of Huntington's disease. J Neurosci Off J Soc Neurosci 29:10371–10386.

Della Sala G, Putignano E, Chelini G, Melani R, Calcagno E, Michele Ratto G, Amendola E, Gross CT, Giustetto M, Pizzorusso T (2016) Dendritic Spine Instability in a Mouse Model of CDKL5 Disorder Is Rescued by Insulin-like Growth Factor 1. Biol Psychiatry 80:302–311.

Devlin H (2017) Excitement as trial shows Huntington's drug could slow progress of disease. The Guardian Available at: http://www.theguardian.com/science/2017/dec/11/excitement-as-huntingtons-drug-shown-to-slow-progress-of-devastating-disease [Accessed July 31, 2018].

Dimos JT, Rodolfa KT, Niakan KK, Weisenthal LM, Mitsumoto H, Chung W, Croft GF, Saphier G, Leibel R, Goland R, Wichterle H, Henderson CE, Eggan K (2008) Induced pluripotent stem cells generated from patients with ALS can be differentiated into motor neurons. Science 321:1218–1221.

Döbrössy MD, Dunnett SB (2006) The effects of lateralized training on spontaneous forelimb preference, lesion deficits, and graft-mediated functional recovery after unilateral striatal lesions in rats. Exp Neurol 199:373–383.

Dong X, Wang Y, Qin Z (2009) Molecular mechanisms of excitotoxicity and their relevance to pathogenesis of neurodegenerative diseases. Acta Pharmacol Sin 30:379–387.

Dragatsis I, Levine MS, Zeitlin S (2000) Inactivation of Hdh in the brain and testis results in progressive neurodegeneration and sterility in mice. Nat Genet 26:300–306.

Evans MJ, Kaufman MH (1981) Establishment in culture of pluripotential cells from mouse embryos. Nature 292:154–156.

Evers MM, Tran H-D, Zalachoras I, Meijer OC, den Dunnen JT, van Ommen G-JB, Aartsma-Rus A, van Roon-Mom WMC (2014) Preventing formation of toxic N-terminal huntingtin fragments through antisense oligonucleotide-mediated protein modification. Nucleic Acid Ther 24:4–12.

Ferrer I, Goutan E, Marín C, Rey MJ, Ribalta T (2000) Brain-derived neurotrophic factor in Huntington disease. Brain Res 866:257–261.

Fuchs C, Fustini N, Trazzi S, Gennaccaro L, Rimondini R, Ciani E (2018) Treatment with the GSK3-beta inhibitor Tideglusib improves hippocampal development and memory performance in juvenile, but not adult, Cdkl5 knockout mice. Eur J Neurosci 47:1054–1066.

Fuchs C, Rimondini R, Viggiano R, Trazzi S, De Franceschi M, Bartesaghi R, Ciani E (2015) Inhibition of GSK3β rescues hippocampal development and learning in a mouse model of CDKL5 disorder. Neurobiol Dis 82:298–310.

Fuchs C, Trazzi S, Torricella R, Viggiano R, De Franceschi M, Amendola E, Gross C, Calzà L, Bartesaghi R, Ciani E (2014) Loss of CDKL5 impairs survival and dendritic growth of newborn neurons by altering AKT/GSK-3β signaling. Neurobiol Dis 70:53–68.

Fukata Y, Itoh TJ, Kimura T, Ménager C, Nishimura T, Shiromizu T, Watanabe H, Inagaki N, Iwamatsu A, Hotani H, Kaibuchi K (2002) CRMP-2 binds to tubulin heterodimers to promote microtubule assembly. Nat Cell Biol 4:583–591.

Gallagher J (2017) Huntington’s breakthrough may stop disease. BBC News Available at: https://www.bbc.com/news/health-42308341 [Accessed July 31, 2018].

Ganguly K, Schinder AF, Wong ST, Poo M (2001) GABA itself promotes the developmental switch of neuronal GABAergic responses from excitation to inhibition. Cell 105:521–532.

Gao Z, Ure K, Ables JL, Lagace DC, Nave K-A, Goebbels S, Eisch AJ, Hsieh J (2009) Neurod1 is essential for the survival and maturation of adult-born neurons. Nat Neurosci 12:1090–1092.

Gaura V, Bachoud-Lévi A-C, Ribeiro M-J, Nguyen J-P, Frouin V, Baudic S, Brugières P, Mangin J-F, Boissé M-F, Palfi S, Cesaro P, Samson Y, Hantraye P, Peschanski M, Remy P (2004) Striatal neural grafting improves cortical metabolism in Huntington's disease patients. Brain J Neurol 127:65–72.

Gauthier LR, Charrin BC, Borrell-Pagès M, Dompierre JP, Rangone H, Cordelières FP, De Mey J, MacDonald ME, Lessmann V, Humbert S, Saudou F (2004) Huntingtin controls neurotrophic support and survival of neurons by enhancing BDNF vesicular transport along microtubules. Cell 118:127–138.

Gharami K, Xie Y, An JJ, Tonegawa S, Xu B (2008) Brain-derived Neurotrophic Factor Over-expression in the Forebrain Ameliorates Huntington's Disease Phenotypes in Mice. J Neurochem 105:369–379.

Gonzales KK, Pare J-F, Wichmann T, Smith Y (2013) GABAergic Inputs from Direct and Indirect Striatal Projection Neurons Onto Cholinergic Interneurons in the Primate Putamen. J Comp Neurol 521:2502–2522.

Greger IH, Watson JF, Cull-Candy SG (2017) Structural and Functional Architecture of AMPA-Type Glutamate Receptors and Their Auxiliary Proteins. Neuron 94:713–730.

Guidetti P, Luthi-Carter RE, Augood SJ, Schwarcz R (2004) Neostriatal and cortical quinolinate levels are increased in early grade Huntington's disease. Neurobiol Dis 17:455–461.

Guidetti P, Schwarcz R (2008) 3-Hydroxykynurenine potentiates quinolinate but not NMDA toxicity in the rat striatum. Eur J Neurosci 11:3857–3863.

Gupta V, Chitranshi N, You Y, Gupta V, Klistorner A, Graham S (2014) Brain derived neurotrophic factor is involved in the regulation of glycogen synthase kinase 3β (GSK3β) signalling. Biochem Biophys Res Commun 454:381–386.

Heldt SA, Stanek L, Chhatwal JP, Ressler KJ (2007) Hippocampus-specific deletion of BDNF in adult mice impairs spatial memory and extinction of aversive memories. Mol Psychiatry 12:656–670.

Hentschke H (2011) abfload - File Exchange - MATLAB Central. Available at: https://uk.mathworks.com/matlabcentral/fileexchange/6190 [Accessed September 19, 2018].

Hentze H, Soong PL, Wang ST, Phillips BW, Putti TC, Dunn NR (2009) Teratoma formation by human embryonic stem cells: Evaluation of essential parameters for future safety studies. Stem Cell Res 2:198–210.

Hermann L (1905) Lehrbuch der Physiologie. A. Hirschwald. Available at: http://archive.org/details/lehrbuchderphys01hermgoog [Accessed September 17, 2018].

Hille B (1984) Ionic channels in excitable membranes. Current problems and biophysical approaches., 1st ed. Massachuetts, USA: Sinauer Associates Inc.

Hodgkin AL, Huxley AF (1952) A quantitative description of membrane current and its application to conduction and excitation in nerve. J Physiol. 1952 Aug 28;117(4):500–44.

Hodgkin AL, Eccles J, Huxley A (1963) The Nobel Prize in Physiology or Medicine 1963. Available at: https://www.nobelprize.org/nobel_prizes/medicine/laureates/1963/index.html [Accessed July 9, 2018].

Hormuzdi SG, Filippov MA, Mitropoulou G, Monyer H, Bruzzone R (2004) Electrical synapses: a dynamic signaling system that shapes the activity of neuronal networks. Biochim Biophys Acta BBA - Biomembr 1662:113–137.

Hu Y-S, Long N, Pigino G, Brady ST, Lazarov O (2013) Molecular Mechanisms of Environmental Enrichment: Impairments in Akt/GSK3β, Neurotrophin-3 and CREB Signaling. PLOS ONE 8:e64460.

Huang J, Guo X, Li W, Zhang H (2017) Activation of Wnt/β-catenin signalling *via* GSK3 inhibitors direct differentiation of human adipose stem cells into functional hepatocytes. Sci Rep 7:40716.

Iwano S et al. (2018) Single-cell bioluminescence imaging of deep tissue in freely moving animals. Science 359:935–939.

Kalscheuer VM, Tao J, Donnelly A, Hollway G, Schwinger E, Kübart S, Menzel C, Hoeltzenbein M, Tommerup N, Eyre H, Harbord M, Haan E, Sutherland GR, Ropers H-H, Gécz J (2003) Disruption of the Serine/Threonine Kinase 9 Gene Causes Severe X-Linked Infantile Spasms and Mental Retardation. Am J Hum Genet 72:1401–1411.

Kordasiewicz HB, Stanek LM, Wancewicz EV, Mazur C, McAlonis MM, Pytel KA, Artates JW, Weiss A, Cheng SH, Shihabuddin LS, Hung G, Bennett CF, Cleveland DW (2012) Sustained therapeutic reversal of Huntington’s disease by transient repression of huntingtin synthesis. Neuron 74:1031–1044.

Leavitt BR, van Raamsdonk JM, Shehadeh J, Fernandes H, Murphy Z, Graham RK, Wellington CL, Raymond LA, Hayden MR (2006) Wild-type huntingtin protects neurons from excitotoxicity. J Neurochem 96:1121–1129.

Lehnertz K, Bialonski S, Horstmann M-T, Krug D, Rothkegel A, Staniek M, Wagner T (2009) Synchronization phenomena in human epileptic brain networks. J Neurosci Methods 183:42–48.

LING G-Q, CHEN D-B, WANG B-Q, ZHANG L-S (2012) Expression of the pluripotency markers Oct3/4, Nanog and Sox2 in human breast cancer cell lines. Oncol Lett 4:1264–1268.

Liske H, Qian X, Anikeeva P, Deisseroth K, Delp S (2013) Optical control of neuronal excitation and inhibition using a single opsin protein, ChR2. Sci Rep 3:3110.

Liu Y, Lopez-Santiago LF, Yuan Y, Jones JM, Zhang H, O'Malley HA, Patino GA, O'Brien JE, Rusconi R, Gupta A, Thompson RC, Natowicz MR, Meisler MH, Isom LL, Parent JM (2013) Dravet syndrome patient-derived neurons suggest a novel epilepsy mechanism. Ann Neurol 74:128–139.

Lodish H, Berk A, Zipursky SL, Matsudaira P, Baltimore D, Darnell J (2000) Intracellular Ion Environment and Membrane Electric Potential. Mol Cell Biol 4th Ed Available at: https://www.ncbi.nlm.nih.gov/books/NBK21627/ [Accessed July 4, 2018].

Lucas JJ, Hernández F, Gómez-Ramos P, Morán MA, Hen R, Avila J (2001) Decreased nuclear β-catenin, tau hyperphosphorylation and neurodegeneration in GSK-3β conditional transgenic mice. EMBO J 20:27–39.

Ma L, Hu B, Liu Y, Vermilyea SC, Liu H, Gao L, Sun Y, Zhang X, Zhang S-C (2012) Human Embryonic Stem Cell-Derived GABA Neurons Correct Locomotion Deficits in Quinolinic Acid-Lesioned Mice. Cell Stem Cell 10:455–464.

Mandal M, Wei J, Zhong P, Chen J, Duffney LJ, Liu W, Yuen EY, Twelvetrees AE, Li S, Li X-J, Kittler JT, Yan Z (2011) Impaired AMPA receptor trafficking and function by mutant Huntingtin. J Biol Chem:jbc.M111.236521.

Mangiarini L, Sathasivam K, Seller M, Cozens B, Harper A, Hetherington C, Lawton M, Trottier Y, Lehrach H, Davies SW, Bates GP (1996) Exon 1 of the HD gene with an expanded CAG repeat is sufficient to cause a progressive neurological phenotype in transgenic mice. Cell 87:493–506.

Marchetto MCN, Carromeu C, Acab A, Yu D, Yeo GW, Mu Y, Chen G, Gage FH, Muotri AR (2010) A model for neural development and treatment of Rett syndrome using human induced pluripotent stem cells. Cell 143:527–539.

Marolt D, Campos IM, Bhumiratana S, Koren A, Petridis P, Zhang G, Spitalnik PF, Grayson WL, Vunjak-Novakovic G (2012) Engineering bone tissue from human embryonic stem cells. Proc Natl Acad Sci 109:8705–8709.

Massa SM, Yang T, Xie Y, Shi J, Bilgen M, Joyce JN, Nehama D, Rajadas J, Longo FM (2010) Small molecule BDNF mimetics activate TrkB signaling and prevent neuronal degeneration in rodents. J Clin Invest 120:1774–1785.

Mathworks (2018) Deep Learning Toolbox. Available at: https://uk.mathworks.com/products/deep-learning.html [Accessed September 24, 2018].

Mazzocchi-Jones D, Döbrössy M, Dunnett SB (2009) Embryonic striatal grafts restore bi-directional synaptic plasticity in a rodent model of Huntington's disease. Eur J Neurosci 30:2134–2142.

McBride JL, Behrstock SP, Chen E-Y, Jakel RJ, Siegel I, Svendsen CN, Kordower JH (2004) Human neural stem cell transplants improve motor function in a rat model of Huntington's disease. J Comp Neurol 475:211–219.

Mishra R, Barthwal MK, Sondarva G, Rana B, Wong L, Chatterjee M, Woodgett JR, Rana A (2007) Glycogen Synthase Kinase-3β Induces Neuronal Cell Death via Direct Phosphorylation of Mixed Lineage Kinase 3. J Biol Chem 282:30393–30405.

Montanara PL, Rusconi L, Locarno A, Forti L, Barbiero I, Tramarin M, Chandola C, Kilstrup-Nielsen C, Landsberger N (2015) Synaptic Synthesis, Dephosphorylation, and Degradation A NOVEL PARADIGM FOR AN ACTIVITY-DEPENDENT NEURONAL CONTROL OF CDKL5. J Biol Chem 290:4512–4527.

Nasir J, Floresco SB, O'Kusky JR, Diewert VM, Richman JM, Zeisler J, Borowski A, Marth JD, Phillips AG, Hayden MR (1995) Targeted disruption of the Huntington's disease gene results in embryonic lethality and behavioral and morphological changes in heterozygotes. Cell 81:811–823.

Ndountse LT, Chan HM (2009) Role of N-methyl-D-aspartate receptors in polychlorinated biphenyl mediated neurotoxicity. Toxicol Lett 184:50–55.

New Scientist (2017) Antisense therapy promises to slow Huntington's disease. New Sci Available at: https://www.newscientist.com/article/mg23631564-600-antisense-therapy-promises-to-slow-huntingtons-disease/ [Accessed July 31, 2018].

Nguyen HN, Byers B, Cord B, Shcheglovitov A, Byrne J, Gujar P, Kee K, Schüle B, Dolmetsch RE, Langston W, Palmer TD, Pera RR (2011) LRRK2 mutant iPSC-derived DA neurons demonstrate increased susceptibility to oxidative stress. Cell Stem Cell 8:267–280.

Nicoleau C, Varela C, Bonnefond C, Maury Y, Bugi A, Aubry L, Viegas P, Bourgois-Rocha F, Peschanski M, Perrier AL (2013) Embryonic stem cells neural differentiation qualifies the role of Wnt/β-Catenin signals in human telencephalic specification and regionalization. STEM CELLS 31:1763–1774.

Noakes Z, Fjodorova M, Li M (2015) Deriving striatal projection neurons from human pluripotent stem cells with Activin A. Neural Regen Res 10:1914–1916.

Office for National Statistics (2016) Deaths registered in England and Wales (series DR) - Office for National Statistics. Available at: https://www.ons.gov.uk/peoplepopulationandcommunity/birthsdeathsandmarriages/deaths/bulletins/deathsregisteredinenglandandwalesseriesdr/2016 [Accessed February 9, 2018].

Ohm GS (1827) Die galvanische kette, mathematisch. Berlin, T. H. Riemann. Available at: http://archive.org/details/diegalvanischek00ohmgoog [Accessed July 3, 2018].

Okuda S, Nishiyama N, Saito H, Katsuki H (1996) Hydrogen peroxide-mediated neuronal cell death induced by an endogenous neurotoxin, 3-hydroxykynurenine. Proc Natl Acad Sci 93:12553–12558.

Østergaard ME, Southwell AL, Kordasiewicz H, Watt AT, Skotte NH, Doty CN, Vaid K, Villanueva EB, Swayze EE, Bennett CF, Hayden MR, Seth PP (2013) Rational design of antisense oligonucleotides targeting single nucleotide polymorphisms for potent and allele selective suppression of mutant Huntingtin in the CNS. Nucleic Acids Res 41:9634–9650.

Park I-H, Arora N, Huo H, Maherali N, Ahfeldt T, Shimamura A, Lensch MW, Cowan C, Hochedlinger K, Daley GQ (2008) Disease-specific induced pluripotent stem cells. Cell 134:877–886.

Paul JR, DeWoskin D, McMeekin LJ, Cowell RM, Forger DB, Gamble KL (2016) Regulation of persistent sodium currents by glycogen synthase kinase 3 encodes daily rhythms of neuronal excitability. Nat Commun 7:13470.

Pecorelli A, Ciccoli L, Signorini C, Leoncini S, Giardini A, D'Esposito M, Filosa S, Hayek J, De Felice C, Valacchi G (2011) Increased levels of 4HNE-protein plasma adducts in Rett syndrome. Clin Biochem 44:368–371.

Pellock JM, Hrachovy R, Shinnar S, Baram TZ, Bettis D, Dlugos DJ, Gaillard WD, Gibson PA, Holmes GL, Nordl DR, O'Dell C, Shields WD, Trevathan E, Wheless JW (2010) Infantile spasms: a U.S. consensus report. Epilepsia 51:2175–2189.

Penn AC, Zhang CL, Georges F, Royer L, Breillat C, Hosy E, Petersen JD, Humeau Y, Choquet D (2017) Hippocampal LTP and contextual learning require surface diffusion of AMPA receptors. Nature 549:384–388.

Perkins MN, Stone TW (1983) Pharmacology and regional variations of quinolinic acid-evoked excitations in the rat central nervous system. J Pharmacol Exp Ther 226:551–557.

Reidling JC et al. (2018) Human Neural Stem Cell Transplantation Rescues Functional Deficits in R6/2 and Q140 Huntington's Disease Mice. Stem Cell Rep 10:58–72.

Reuter I, Tai YF, Pavese N, Chaudhuri KR, Mason S, Polkey CE, Clough C, Brooks DJ, Barker RA, Piccini P (2008) Long-term clinical and positron emission tomography outcome of fetal striatal transplantation in Huntington's disease. J Neurol Neurosurg Psychiatry 79:948–951.

Ricciardi S, Ungaro F, Hambrock M, Rademacher N, Stefanelli G, Brambilla D, Sessa A, Magagnotti C, Bachi A, Giarda E, Verpelli C, Kilstrup-Nielsen C, Sala C, Kalscheuer VM, Broccoli V (2012) CDKL5 ensures excitatory synapse stability by reinforcing NGL-1–PSD95 interaction in the postsynaptic compartment and is impaired in patient iPSC-derived neurons. Nat Cell Biol 14:911–923.

Ridler T, Matthews P, Phillips KG, Randall AD, Brown JT (2018) Initiation and slow propagation of epileptiform activity from ventral to dorsal medial entorhinal cortex is constrained by an inhibitory gradient. J Physiol 596:2251–2266.

Rosenblatt A, Brinkman RR, Liang KY, Almqvist EW, Margolis RL, Huang CY, Sherr M, Franz ML, Abbott MH, Hayden MR, Ross CA (2001) Familial influence on age of onset among siblings with Huntington disease. Am J Med Genet 105:399–403.

Rubinsztein DC et al. (1996) Phenotypic characterization of individuals with 30-40 CAG repeats in the Huntington disease (HD) gene reveals HD cases with 36 repeats and apparently normal elderly individuals with 36-39 repeats. Am J Hum Genet 59:16–22.

Rué L, Bañez-Coronel M, Creus-Muncunill J, Giralt A, Alcalá-Vida R, Mentxaka G, Kagerbauer B, Zomeño-Abellán MT, Aranda Z, Venturi V, Pérez-Navarro E, Estivill X, Martí E (2016) Targeting CAG repeat RNAs reduces Huntington's disease phenotype independently of huntingtin levels. J Clin Invest 126:4319–4330.

Ryu JK, Kim J, Cho SJ, Hatori K, Nagai A, Choi HB, Lee MC, McLarnon JG, Kim SU (2004) Proactive transplantation of human neural stem cells prevents degeneration of striatal neurons in a rat model of Huntington disease. Neurobiol Dis 16:68–77.

Sando R, Gounko N, Pieraut S, Liao L, Yates J, Maximov A (2012) HDAC4 Governs a Transcriptional Program Essential for Synaptic Plasticity and Memory. Cell 151:821–834.

Scala E, Ariani F, Mari F, Caselli R, Pescucci C, Longo I, Meloni I, Giachino D, Bruttini M, Hayek G, Zappella M, Renieri A (2005) CDKL5/STK9 is mutated in Rett syndrome variant with infantile spasms. J Med Genet 42:103–107.

Schwarcz R, Köhler C (1983) Differential vulnerability of central neurons of the rat to quinolinic acid. Neurosci Lett 38:85–90.

Schwartz SD, Hubschman J-P, Heilwell G, Franco-Cardenas V, Pan CK, Ostrick RM, Mickunas E, Gay R, Klimanskaya I, Lanza R (2012) Embryonic stem cell trials for macular degeneration: a preliminary report. Lancet Lond Engl 379:713–720.

Sekiguchi M, Katayama S, Hatano N, Shigeri Y, Sueyoshi N, Kameshita I (2013) Identification of amphiphysin 1 as an endogenous substrate for CDKL5, a protein kinase associated with X-linked neurodevelopmental disorder. Arch Biochem Biophys 535:257–267.

Shin JW, Kim K-H, Chao MJ, Atwal RS, Gillis T, MacDonald ME, Gusella JF, Lee J-M (2016) Permanent inactivation of Huntington's disease mutation by personalized allele-specific CRISPR/Cas9. Hum Mol Genet 25:4566–4576.

Skiteva O, Yao N, Nouhi M, Chergui K (2018) High frequency stimulation induces LTD of AMPA receptor-mediated postsynaptic responses and LTP of synaptically-evoked firing in the dorsolateral striatum. Neurosci Lett 666:11–16.

Skotte NH, Southwell AL, Østergaard ME, Carroll JB, Warby SC, Doty CN, Petoukhov E, Vaid K, Kordasiewicz H, Watt AT, Freier SM, Hung G, Seth PP, Bennett CF, Swayze EE, Hayden MR (2014) Allele-specific suppression of mutant huntingtin using antisense oligonucleotides: providing a therapeutic option for all Huntington disease patients. PloS One 9:e107434.

Soldner F, Hockemeyer D, Beard C, Gao Q, Bell GW, Cook EG, Hargus G, Blak A, Cooper O, Mitalipova M, Isacson O, Jaenisch R (2009) Parkinson's disease patient-derived induced pluripotent stem cells free of viral reprogramming factors. Cell 136:964–977.

Southwell AL, Skotte NH, Kordasiewicz HB, Østergaard ME, Watt AT, Carroll JB, Doty CN, Villanueva EB, Petoukhov E, Vaid K, Xie Y, Freier SM, Swayze EE, Seth PP, Bennett CF, Hayden MR (2014) In vivo evaluation of candidate allele-specific mutant huntingtin gene silencing antisense oligonucleotides. Mol Ther J Am Soc Gene Ther 22:2093–2106.

Spangler SG (1972) Expansion of the constant field equation to include both divalent and monovalent ions. Ala J Med Sci 9:218–223.

Spira ME, Hai A (2013) Multi-electrode array technologies for neuroscience and cardiology. Nat Nanotechnol 8:83–94.

Spires TL, Grote HE, Varshney NK, Cordery PM, van Dellen A, Blakemore C, Hannan AJ (2004) Environmental enrichment rescues protein deficits in a mouse model of Huntington's disease, indicating a possible disease mechanism. J Neurosci Off J Soc Neurosci 24:2270–2276.

Stanek LM, Yang W, Angus S, Sardi PS, Hayden MR, Hung GH, Bennett CF, Cheng SH, Shihabuddin LS (2013) Antisense oligonucleotide-mediated correction of transcriptional dysregulation is correlated with behavioral benefits in the YAC128 mouse model of Huntington's disease. J Huntingt Dis 2:217–228.

Tabrizi S, Leavitt B, Kordasiewicz H, Czech C, Swayze E, Norris DA, Baumann T, Gerlach I, Schobel S, Smith A, Lane R, Bennett CF (2018) Effects of IONIS-HTTRx in Patients with Early Huntington's Disease, Results of the First HTT-Lowering Drug Trial (CT.002). Neurology 90:CT.002.

Takahashi K, Tanabe K, Ohnuki M, Narita M, Ichisaka T, Tomoda K, Yamanaka S (2007) Induction of pluripotent stem cells from adult human fibroblasts by defined factors. Cell 131:861–872.

Takahashi K, Yamanaka S (2006) Induction of pluripotent stem cells from mouse embryonic and adult fibroblast cultures by defined factors. Cell 126:663–676.

Tao C, Zhang G, Xiong Y, Zhou Y (2015) Functional dissection of synaptic circuits: in vivo patch-clamp recording in neuroscience. Front Neural Circuits 9 Available at: https://www.ncbi.nlm.nih.gov/pmc/articles/PMC4440909/ [Accessed July 10, 2018].

Tavares RG, Tasca CI, Santos CE, Wajner M, Souza DO, Dutra-Filho CS (2000) Quinolinic acid inhibits glutamate uptake into synaptic vesicles from rat brain. Neuroreport 11:249–253.

Tavares RG, Tasca CI, Santos CES, Alves LB, Porciúncula LO, Emanuelli T, Souza DO (2002) Quinolinic acid stimulates synaptosomal glutamate release and inhibits glutamate uptake into astrocytes. Neurochem Int 40:621–627.

Telezhkin V et al. (2016) Forced cell cycle exit and modulation of GABAA, CREB, and GSK3β signaling promote functional maturation of induced pluripotent stem cell-derived neurons. Am J Physiol - Cell Physiol 310:C520–C541.

Thomson JA, Itskovitz-Eldor J, Shapiro SS, Waknitz MA, Swiergiel JJ, Marshall VS, Jones JM (1998) Embryonic Stem Cell Lines Derived from Human Blastocysts. Science 282:1145–1147.

Trazzi S, Fuchs C, Viggiano R, De Franceschi M, Valli E, Jedynak P, Hansen FK, Perini G, Rimondini R, Kurz T, Bartesaghi R, Ciani E (2016) HDAC4: a key factor underlying brain developmental alterations in CDKL5 disorder. Hum Mol Genet 25:3887–3907.

Varela F, Lachaux J-P, Rodriguez E, Martinerie J (2001) The brainweb: Phase synchronization and large-scale integration. Nat Rev Neurosci 2:229–239.

Walker FO (2007) Huntington’s disease. The Lancet 369:218–228.

Wang I-TJ, Allen M, Goffin D, Zhu X, Fairless AH, Brodkin ES, Siegel SJ, Marsh ED, Blendy JA, Zhou Z (2012) Loss of CDKL5 disrupts kinome profile and event-related potentials leading to autistic-like phenotypes in mice. Proc Natl Acad Sci 109:21516–21521.

Wexler NS et al. (2004) Venezuelan kindreds reveal that genetic and environmental factors modulate Huntington’s disease age of onset. Proc Natl Acad Sci U S A 101:3498–3503.

Wu C-C, Lien C-C, Hou W-H, Chiang P-M, Tsai K-J (2016) Gain of BDNF Function in Engrafted Neural Stem Cells Promotes the Therapeutic Potential for Alzheimer’s Disease. Sci Rep 6:27358.

Wu Y, Liu F, Liu Y, Liu X, Ai Z, Guo Z, Zhang Y (2015) GSK3 inhibitors CHIR99021 and 6-bromoindirubin-3′-oxime inhibit microRNA maturation in mouse embryonic stem cells. Sci Rep 5:8666.

Wuebben EL, Rizzino A (2017) The dark side of SOX2: cancer - a comprehensive overview. Oncotarget 8:44917–44943.

Yoshimura T, Kawano Y, Arimura N, Kawabata S, Kikuchi A, Kaibuchi K (2005) GSK-3beta regulates phosphorylation of CRMP-2 and neuronal polarity. Cell 120:137–149.

Zhang H, Zhang C, Vincent J, Zala D, Benstaali C, Sainlos M, Grillo-Bosch D, Daburon S, Coussen F, Cho Y, David DJ, Saudou F, Humeau Y, Choquet D (2018) Pharmacological modulation of AMPA receptor surface diffusion restores hippocampal synaptic plasticity and memory in Huntington's disease. bioRxiv:297069.

Zhang Y, Leavitt BR, van Raamsdonk JM, Dragatsis I, Goldowitz D, MacDonald ME, Hayden MR, Friedlander RM (2006) Huntingtin inhibits caspase-3 activation. EMBO J 25:5896–5906.

Zhang Y, Li M, Drozda M, Chen M, Ren S, Mejia Sanchez RO, Leavitt BR, Cattaneo E, Ferrante RJ, Hayden MR, Friedlander RM (2003) Depletion of wild-type huntingtin in mouse models of neurologic diseases. J Neurochem 87:101–106.

Zhao F-Q, Misra Y, Li D-B, Wadsworth MP, Krag D, Weaver D, Tessitore J, Li D-W, Zhang G, Tian Q, Buss K (2018) Differential expression of Oct3/4 in human breast cancer and normal tissues. Int J Oncol 52:2069–2078.

Zhao Y, Zhang X, Bao X, Zhang Q, Zhang J, Cao G, Zhang J, Li J, Wei L, Pan H, Wu X (2014) Clinical features and gene mutational spectrum of CDKL5-related diseases in a cohort of Chinese patients. BMC Med Genet 15:24.

Zhu Y-C, Li D, Wang L, Lu B, Zheng J, Zhao S-L, Zeng R, Xiong Z-Q (2013) Palmitoylation-dependent CDKL5–PSD-95 interaction regulates synaptic targeting of CDKL5 and dendritic spine development. Proc Natl Acad Sci 110:9118–9123.

Zuccato C, Ciammola A, Rigamonti D, Leavitt BR, Goffredo D, Conti L, MacDonald ME, Friedlander RM, Silani V, Hayden MR, Timmusk T, Sipione S, Cattaneo E (2001) Loss of huntingtin-mediated BDNF gene transcription in Huntington's disease. Science 293:493–498.

Zuccato C, Marullo M, Vitali B, Tarditi A, Mariotti C, Valenza M, Lahiri N, Wild EJ, Sassone J, Ciammola A, Bachoud-Lèvi AC, Tabrizi SJ, Di Donato S, Cattaneo E (2011) Brain-derived neurotrophic factor in patients with Huntington's disease. PloS One 6:e22966.